OPTOMECHANICAL LIGHT STORAGE

AND RELATED TRANSIENT OPTOMECHANICAL PHENOMENA

by

VICTOR NORVISON FIORE

A DISSERTATION

Presented to the Department of Physics
and the Graduate School of the University of Oregon
in partial fulfillment of the requirements
for the degree of
Doctor of Philosophy

June 2015

DISSERTATION APPROVAL PAGE

Student: Victor Norvison Fiore

Title: Optomechanical Light Storage and Related Transient Optomechanical Phenomena

This dissertation has been accepted and approved in partial fulfillment of the requirements for the Doctor of Philosophy degree in the Department of Physics by:

Dr. Michael Raymer	Chair
Dr. Hailin Wang	Advisor
Dr. Eric Torrence	Core Member
Dr. Paul Csonka	Core Member
Dr. Mark Lonergan	Institutional Representative

and

Scott L. Pratt	Dean of the Graduate School

Original approval signatures are on file with the University of Oregon Graduate School.

Degree awarded June 2015

DISSERTATION ABSTRACT

Victor Norvison Fiore

Doctor of Philosophy

Department of Physics

June 2015

Title: Optomechanical Light Storage and Related Transient Optomechanical Phenomena

An optomechanical system consists of an optical cavity coupled to a mechanical oscillator. The system used for this work was a silica microsphere. In a silica microsphere, the optical cavity is formed by light that is confined by total internal reflection while circulating around the equator of the sphere. The mechanical oscillator is the mechanical breathing motion of the sphere itself. The optical cavity and mechanical oscillator are coupled by radiation pressure and by the mechanical oscillator physically changing the length of the optical cavity.

The optomechanical analog to electromagnetically induced transparency (EIT), known as optomechanically induced transparency (OMIT), has previously been studied in its steady state. One topic of this dissertation is an experimental study of OMIT in the time domain. The results of these experimental demonstrations continue comparisons between EIT and OMIT, while also building a foundation for optomechanical light storage.

In OMIT, an off-resonance control laser controls the interaction between on-resonance light and the mechanical oscillator. Optomechanical light storage makes use of this arrangement to store an optical signal as a mechanical excitation, which is then retrieved at a later time as an optical signal. This is done by using two

temporally separated off-resonance control laser pulses. This technique is extremely flexible in frequency and displays a storage lifetime on the order of microseconds.

Use of optomechanical systems for quantum mechanical applications is hindered by the thermal background noise of the mechanical oscillator. Addressing this issue by first cooling the mechanical oscillator is costly and fraught with difficulties. The final topic presented in this dissertation deals with this issue through the use of an optomechanical dark mode. Two optical modes can interact with the same mechanical mode. The dark mode is a state that couples the two optical modes but is decoupled from the mechanical oscillator. While our specific optomechanical system is limited by its somewhat modest optomechanical cooperativity, this conversion process can, in principle, preserve the quantum state of the signal, even at room temperature, opening the possibility for this technique to be applied in quantum information processing.

CURRICULUM VITAE

NAME OF AUTHOR: Victor Norvison Fiore

GRADUATE AND UNDERGRADUATE SCHOOLS ATTENDED:
   University of Oregon, Eugene OR
   Lafayette College, Easton PA

DEGREES AWARDED:
   Doctor of Philosophy, Physics, 2015, University of Oregon
   Bachelor of Science, Physics, 2008, Lafayette College, *Summa cum laude*
   Bachelor of Science, Chemistry, 2008, Lafayette College, *Summa cum laude*

AREAS OF SPECIAL INTEREST:
   Optomechanics
   Atomic Molecular and Optical Physics
   Physics Education

PROFESSIONAL EXPERIENCE:

   Graduate Research Assistant, Department of Physics,
      University of Oregon, 2009–2013,
      Optomechanics,
      Principal Investigator: Prof. Hailin WANG

   Undergraduate Research Assistant, Department of Physics,
      Lafayette College, 2006–2008,
      Experimental atomic and molecular physics,
      Principal Investigator: Prof. Andy KORTYNA

   Undergraduate Research Assistant, Department of Chemistry,
      Lafayette College, Summer 2005,
      Computational chemistry,
      Principal Investigator: Prof. Kenneth HAUG

   Graduate Science Literacy Program Fellow, Department of Physics,
      University of Oregon, Fall 2012,
      Reference: Prof. Dan STECK

   Teaching Assistant, Department of Physics,
      University of Oregon, 2008–2013

GRANTS, AWARDS AND HONORS:

September 17, 2003, Boy Scouts of America, Eagle Scout

Undergraduate thesis, 2008, Lafayette College: *Hyperfine Measurements of Cesium Using an Atomic Beam Apparatus*

PUBLICATIONS:

C. Dong, J. Zhang, V. Fiore, and H. Wang. Optomechanically induced transparency and self-induced oscillations with Bogoliubov mechanical modes. *Optica* 1:425, 2014.

C. Dong, V. Fiore, M. C. Kuzyk, and H. Wang. Transient optomechanically-induced transparency in a silica microsphere. *Phys. Rev. A*, 87:055802, 2013.

V. Fiore, C. Dong, M. C. Kuzyk, and H. Wang. Optomechanical light storage in a silica microresonator. *Phys. Rev. A*, 87:023812, 2013.

C. Dong, V. Fiore, M. C. Kuzyk, H. Wang. Optomechanical dark mode. *Science*, 338:6114, 2012.

V. Fiore, Y. Yang, M. C. Kuzyk, R. Barbour, L. Tian, and H. Wang. Storing optical information as a mechanical excitation in a silica optomechanical resonator. *Phys. Rev. Lett.*, 107:133601, 2011.

A. Kortyna, V. Fiore, and J. Farrar. Measurement of the cesium $7d^2D_{3/2}$ hyperfine coupling constants in a thermal beam using two-photon fluorescence spectroscopy. *Phys. Rev. A*, 77:062505, 2008.

ACKNOWLEDGEMENTS

First and foremost, I would like to thank my advisor, Hailin Wang, for his guidance and support. His enthusiasm and commitment are inspirational and contagious, and have helped to keep me motivated. Working with him has been a pleasure.

I would also like to thank my committee, Michael Raymer, Eric Torrence, Paul Csonka, and Mark Lonergan, for their support and encouragement.

My colleagues in the Wang lab deserve a lot of gratitude. It has been a joy to be part of such a great community of people. In particular, I would like to thank Russell Barbour, for the many long hours we spent in the lab together, as well as for those times we spent swimming in cold lake water trying to keep our boat from dashing itself against rocky shores. I want to thank Yong Yang, Chunhua Dong, Thein Oo, and Mark Kuzyk for all of the time they spent working with me on our various optomechanics experiments. I would also like to thank Andrew Golter, Tom Baldwin, Nima Dinyari, Carey Phelps and Tim Sweeney for commiserating with me during moments of frustration and for not getting too upset when we all needed the same piece of equipment.

This research would not have been possible without the help of the staff at the university's machine shop. Kris Johnson and Jeffrey Garman have been a huge help with designing and constructing vacuum systems, and John Boosinger has patiently taught me how to use the machine shop to make all the little metal doodads.

I also would like to thank all of the other graduate students. I will always remember those late nights toiling away in the Binney Lounge.

To my loving family.

TABLE OF CONTENTS

LIST OF FIGURES

CHAPTER I

INTRODUCTION TO OPTOMECHANICS

"There are two ways of spreading light: to be the candle or the mirror that reflects it."

– Edith Wharton

1.1. Motivation

Quantum computing and quantum networking are at the forefront of modern physics research[4, 5]. Such systems would make use of quantum nodes connected through quantum channels. The nodes process and store information, and consist of matter qubits[6, 7]. The channels move information from one node to another and would typically consist of optical signals.

Optomechanics offers an exciting avenue to add to the list of tools available for quantum information processing. In particular, many of the proposed systems for matter qubits involve experiments that operate at specific optical frequencies. Since an optomechanical system can couple an extremely flexible range of optical frequencies to a single mechanical oscillator, optomechanics presents a means for optical frequency conversion[8]. This allows quantum state transfer from one optical frequency to another, and can bridge the gap between systems that have conflicting optical frequency requirements.

Additionally, the mechanical oscillator itself can be used as a means for storing an optical signal as a mechanical excitation[2, 3]. Since this process is predominantly limited by the lifetime of the mechanical oscillator, it is possible to achieve relatively long storage lifetimes.

1

1.2. What Is Optomechanics?

Optomechanics is a rapidly growing field in modern physics. In simple terms, an optomechanical system consists of an optical cavity coupled to a mechanical oscillator. By constructing such a system, it becomes possible to use light to both measure and manipulate the mechanical oscillator. This chapter will touch upon the nature of the optical cavity, the mechanical oscillator, and the means by which they are coupled to one another. It will also touch upon some of the consequences and applications of optomechanics.

1.3. Radiation Pressure

At the heart of optomechanics is the phenomenon known as "radiation pressure". Radiation pressure provides the means by which the optical cavity is able to influence the mechanical oscillator. Light carries momentum, with the momentum of a single photon being given by $p = \hbar\omega/c$. Consequently, when light reflects off of a surface, the change in momentum of the light necessitates an equal and opposite momentum change for the reflecting surface. When this occurs for a specific rate of incoming photons over a specific surface area, the resulting force per unit area is seen as a pressure, hence the term "radiation pressure".

Radiation pressure is by no means a recent discovery. The concept was first proposed by Johannes Kepler in 1619 as a method to explain the fact that a comet's tail is always seen pointing away from the Sun[9]. The idea was later formalized by James Maxwell in 1862, as consequence of his equations describing classical electromagnetic radiation[10]. Later, Pyotr Lebedev in 1900, as well as Ernest Nichols and Gordon Hull in 1901, announced the first experimental demonstrations of the

effect[11, 12]. As a side note, the light-mill style Crookes radiometer that is sometimes found adorning window sills is occasionally incorrectly described as being powered by radiation pressure. Radiation pressure by itself is far too weak to be observable with such a simple device. Indeed, the feeble nature of radiation pressure required near-vacuum conditions for the experiments of Lebedev, Nichols, and Hull, so as to not be overwhelmed by thermal effects.

Since then, the phenomenon of radiation pressure has become a prominent fixture in modern optical physics. In 1970, Arthur Ashkin demonstrated the use of focused laser light to control dielectric particles[13], laying the foundation for what is now commonly referred to as "optical tweezers". While it is easier to conceptualize this phenomenon in terms of electric field gradients, it is intrinsically a consequence of radiation pressure. By focusing the laser, photons that are absorbed or scattered by the dielectric particle do so in a way that has a net effect of pushing the particle towards the center of the beam's focus.

Similarly, radiation pressure can be used to slow and trap atoms, thus becoming an essential tool in the field of ultracold atoms. In this application, a clever use of the Doppler effect provides a means for damping the thermal motion of an atomic vapor. A specific frequency of light is required in order to excite a given atomic transition. When light is shined upon an atomic vapor, however, the optical frequency that an individual atom experiences is Doppler shifted as a consequence of the individual atom's motion. Hence if the incoming light is slightly lower than the frequency required to excite the atom, then the atom will only absorb photons when the atom is moving contrary to the photon's direction of travel. In that configuration, the photon momentum associated with every absorption will have the effect of incrementally slowing the atom. The photons are subsequently re-emitted randomly, so the re-

emitted photons have no net effect. Thus the atomic population can be cooled and trapped by hitting it with light in this manner from every direction. This process is referred to as "Doppler cooling".

While there are other important techniques involved in ultracold atoms, Doppler cooling is a cornerstone. The technique was first proposed by Theodor Hänsch and Arthur Schawlow[14], and separately by Hans Dehmelt and David Wineland[15] in 1975, and was first experimentally demonstrated by Wineland, Drullinger, and Walls in 1978[16]. The technique has since allowed for countless groundbreaking discoveries. The first Bose-Einstein condensate was created in this manner by Eric Cornell and Carl Wieman in 1995[17]. Later, in 2003, Deborah Jin took that research a step further by creating the first fermionic condensate[18]. Other applications range from optical atomic clocks to precision measurements of gravity.

Radiation pressure is also the basis for solar sails, which have been proposed as an alternative method for space travel within our solar system[19–21]. The weak magnitude of radiation pressure means that this propulsion method would only be feasible in the near-vacuum of space. For the sake of comparison, the strength of the solar radiation pressure 1 au from the Sun on a perfect reflector is only 9 μPa. To put that into perspective, an average apple weighs about 1 N on the Earth. A solar sail with an area of roughly 10^5 m^2 would be required to produce the same amount of force as the weight of the apple.

1.4. Optical Cavities

Evidently, the radiation pressure from a single reflection by itself is quite weak. This is overcome in optomechanics, however, through the use of a high quality factor optical cavity. In an optical cavity, light can reflect off of the same surface repeatedly,
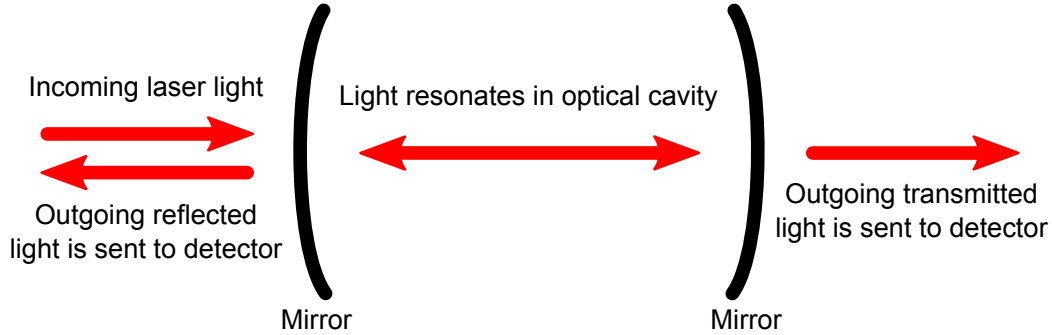
FIGURE 1.1. Schematic of a Fabry-Pérot resonator.

thus compounding the effect of the radiation pressure. The simplest example of an optical cavity is a Fabry-Pérot cavity, which is shown schematically in Fig. 1.1. A Fabry-Pérot cavity consists of two semi-reflective mirrors oriented in such a way that light can resonate between them. As a result of this arrangement, only specific frequencies of light are able to resonate within the cavity, with the resonance condition for a Fabry-Pérot cavity being given by $n\lambda = L$. Here, n is an integer, λ is the wavelength of the light, and L is the round trip distance for the light (i.e. L is two times the distance between the two end-mirrors). This resonance condition will play an important role in optomechanics, which we will return to after a brief description of optical resonators.

The optical resonance is a consequence of constructive interference between light that has circulated in the cavity a different number of times. As the frequency of the incoming laser light is swept across multiple resonances, a sharp peak is seen at each resonance, which is illustrated in Fig. 1.2. The sharpness of the peaks is determined by the optical cavity's quality factor, Q_c, which is a measure of how well the cavity holds light. Light has a chance to exit the cavity through a variety of mechanisms, such as scattering, being absorbed, or leaking through an end-mirror. The overall
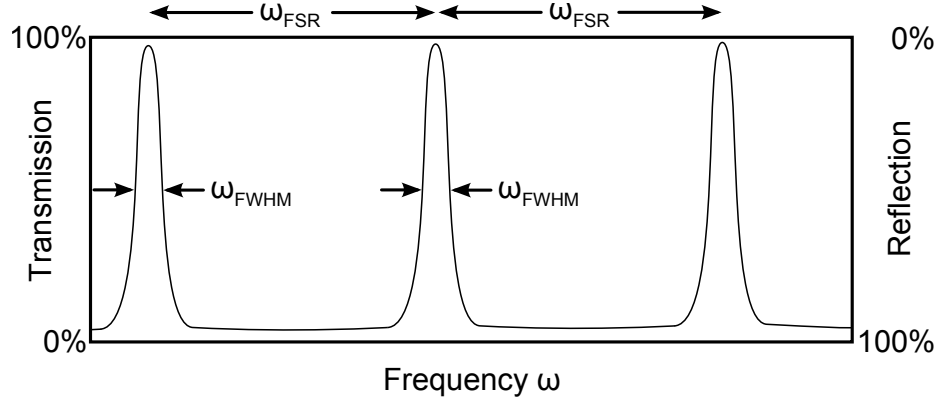
FIGURE 1.2. Illustration of transmission and reflection spectra from a Fabry-Pérot cavity. Adjacent peaks are separated by a frequency ω_{FSR}, which is the "free spectral range" of the cavity. The width of each peak at half of its total height is its "full width at half maximum", or ω_{FWHM}.

cavity decay rate, κ, takes all of these decay channels and lumps them together into one single parameter.

A high Q_c means that light will circulate more times before exiting, which results in sharper resonance peaks. As such, Q_c is related to κ and to the frequency of light in the cavity, ω_c, as follows:

$$Q_c = \frac{\omega_c}{\kappa}. \tag{1.1}$$

For the most part, it is desirable for a cavity to have as high a quality factor as is reasonably practicable. Another parameter, known as the optical finesse, F, is often used as a similar metric. The optical finesse is useful because it relates directly to frequencies found in the cavity's spectrum.

$$F = \frac{\omega_{FSR}}{\omega_{FWHM}} \tag{1.2}$$

Here, ω_{FSR} is the "free spectral range" of the cavity, i.e. the spacing between adjacent resonances. ω_{FWHM} is the "full width at half maximum", which is the width of the
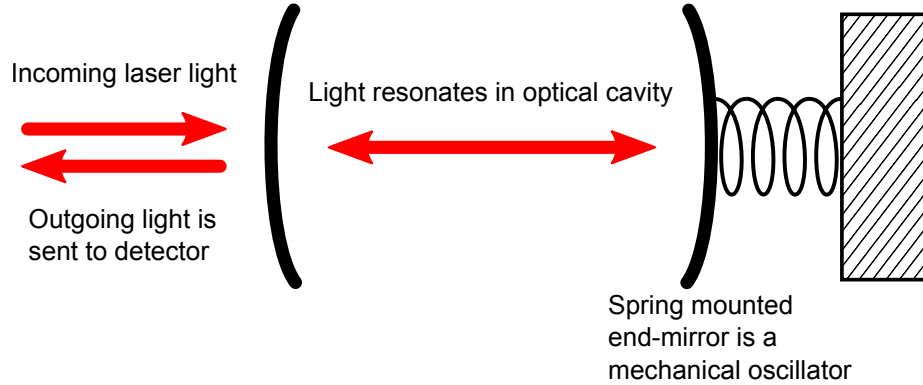
FIGURE 1.3. Schematic of a Fabry-Pérot optomechanical system.

peaks at half their height. Note that both Q_c and F are dimensionless. It should also be said that these resonances are seen as negative dips when looking at light reflected back through the first mirror, and positive peaks when looking at light transmitted through the second mirror.

1.5. Introducing the Mechanical Oscillator

The Fabry-Pérot cavity can be made into an optomechanical system by mounting one of its end-mirrors on a spring, with the spring-mounted end-mirror now playing the role of a mechanical oscillator. This arrangement is shown in Fig. 1.3. As light resonates within the optical cavity, it exerts radiation pressure upon the mirror, thus allowing the optical cavity to influence the mechanical oscillator. Conversely, the vibration of the end-mirror changes the effective length of the optical cavity, providing a means for the mechanical oscillator to influence the optical cavity. We now have a complete picture of coupling between the optical cavity and the mechanical oscillator. The radiation pressure allows the optical cavity to affect the mechanical oscillator, while the mechanical oscillator affects the optical cavity by physically changing the length of the cavity.

Now that we have introduced the mechanical oscillator, it would be prudent to discuss several pertinent attributes relating to mechanical oscillators. There are different mechanisms through which energy can leave the mechanical oscillator. The overall mechanical decay rate, Γ_m, includes all of these mechanisms and is analogous to previously introduced optical decay rate, κ. This mechanical decay rate is different for each mode of oscillation, which is especially significant when we consider more complex oscillators. This being the case, each mode has its own mechanical quality factor,

$$Q_m = \frac{\omega_m}{\Gamma_m},$$
(1.3)

where ω_m is the frequency of the specific mechanical mode. As with the optical quality factor, high mechanical quality factors are preferred.

1.6. Consequences and Applications of Optomechanics

There are a number of intriguing consequences that arise from an optomechanical system. One such consequence is bistability in the effective mechanical potential of the mechanical oscillator, which is due to the influence of the radiation pressure of the optical cavity. The radiation pressure force depends on the photon population of the optical mode, which in turn depends on the mechanical displacement. Thus, by acting upon the mechanical oscillator, the existence of the radiation pressure introduces an additional term into the function for the mechanical potential energy, with this additional term having a dependence on the mechanical displacement. The optical influence upon the mechanical potential is given by[22]

$$V_{rad}(x) = -\frac{1}{2}\hbar\kappa\bar{n}_c^{max}arctan[2(\frac{\omega_c}{L}x + \Delta)/\kappa],$$
(1.4)

8
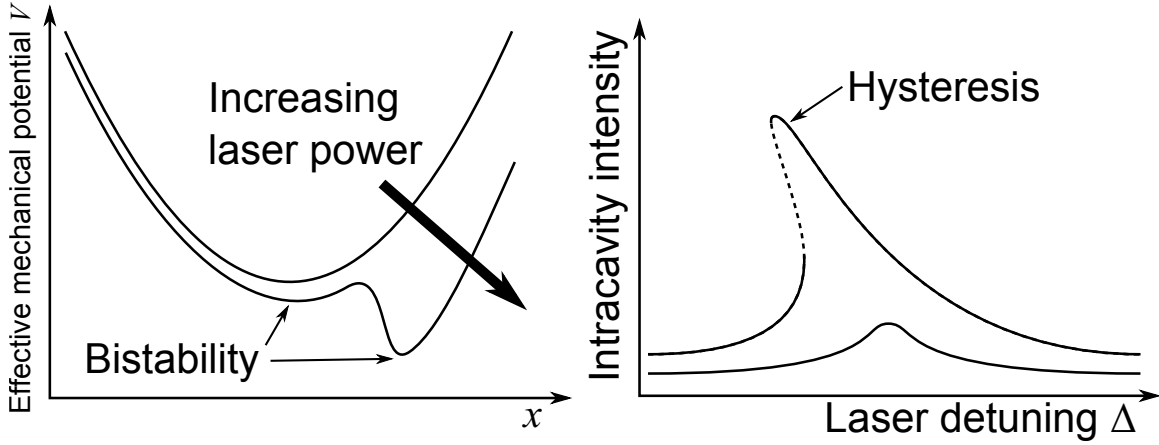
FIGURE 1.4. Left: Sketch of the effective mechanical potential as a function of mechanical displacement, modified by increasing the laser power. Note that increasing the laser power introduces an additional local minimum. Right: Sketch of the intracavity optical population as a function of the laser frequency. This illustrates the hysteresis caused by the bistability.

where $\bar{n}_c^{max}$ is the intracavity photon number when the laser is at resonance, L is the length of the optical cavity, and Δ is the detuning of the driving laser, with $\Delta = \omega_L - \omega_c$. The overall mechanical potential is then given by[22]

$$V(x) = \frac{m_{eff}\omega_m^2}{2}x^2 + V_{rad}(x), \qquad (1.5)$$

with m_{eff} being the effective mass of the mechanical oscillator and V_{rad} being the change in mechanical potential as a consequence of the radiation pressure. Derivations for Eqs. 1.4 and 1.5 can be found in [22].

A full analysis of Eqs. 1.4 and 1.5 is beyond the scope of this dissertation. In the context of our current discussion, the important consequence of Eqs. 1.4 and 1.5 is that increasing the laser power, and hence increasing $\bar{n}_c^{max}$, will alter the effective mechanical potential in such a way that there are two local minima, as shown in Fig. 1.4. This effects a hysteresis in the intracavity optical population, $\bar{n}_c$, which is also shown in Fig. 1.4. As the laser frequency is scanned across the resonance, a different

local minimum is chosen depending on which direction the laser is scanned. Speaking in terms of what might be observed in a laboratory experiment while adjusting the laser frequency by hand, this effect gives the impression of being able to drag the optical mode in one direction along with the laser frequency. Such behavior is quite undesirable for the experiments presented in this thesis, necessitating care when selecting laser power. The laser locking method described in Chapter III will not work if substantial optical bistability is present.

Changing the curvature of the effective mechanical potential in Eq. 1.5 also results in a change in the effective spring constant, which is often referred to as the "optical spring effect". This can be used to produce an artificially larger spring constant by several orders of magnitude, thus providing a means for reducing the impact of damping and environmental heating of the mechanical oscillator[23, 24].

Another remarkable application of optomechanics has been to cool the vibration of the mechanical oscillator[1, 25–27]. This technique has been shown to be so effective that several optomechanical systems have been successfully brought to their quantum mechanical ground state[28–30], with several other systems rapidly approaching this limit[31]. This is quite a ground breaking achievement, as this opens the possibility for performing quantum mechanical experiments on macroscopic systems, thus bridging the gap between the worlds of quantum mechanics and classical mechanics.

The mechanism for the cooling process can be viewed in two different ways: as a consequence of the retarded nature of the radiation pressure, or as a scattering phenomenon. First we shall examine the former. As the mechanical oscillator moves, and subsequently changes the length of the optical cavity, light of a specific frequency is only resonant with the cavity for a specific displacement of the mechanical oscillator. Relative to the timescale of the mechanical oscillations, it takes a consequential
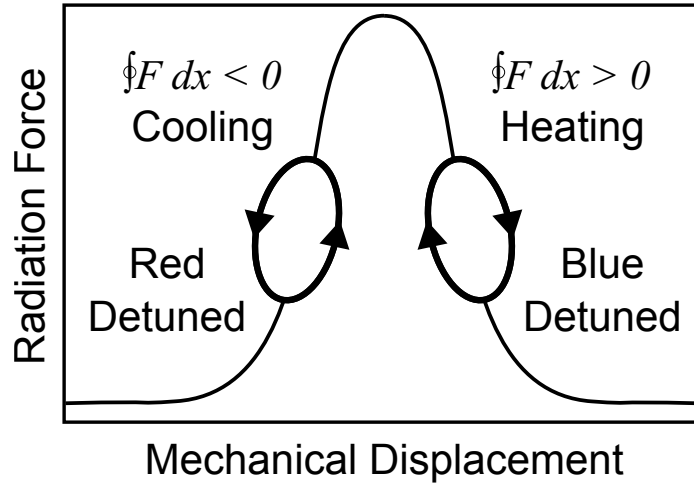
FIGURE 1.5. Optomechanical cooling or heating as a consequence of the retarded nature of the radiation force. As the mechanical oscillator changes the length of the cavity, the response of the optical cavity is slightly delayed. This leads to a hysteresis during the mechanical oscillator's motion; thus work is done on or by the system with each mechanical oscillation. The work is determined by the encompassed area, and the sign of the work determined by the direction of the path integral.

amount of time for light to build up to resonance, hence the radiation pressure is said to be retarded. By carefully selecting the frequency of light, it is possible to time the resonance such that the population of light in the cavity reaches its maximum at a point in time when its radiation pressure opposes the movement of the mechanical oscillator. By doing so, the resulting radiation pressure has a net effect of opposing the movement of the mechanical oscillations, thus cooling the mechanical oscillator. Figure 1.5 illustrates this processes by examining a plot of radiation force vs. mechanical displacement. As a consequence of being retarded, the radiation force lags behind the mechanical displacement. Thus each mechanical oscillation traces out an area within this plot, indicating that work is being done on or by the system[22, 25]. The sign of the path integral determines whether the system is being heated or cooled.

This phenomenon can also be viewed conceptually as a scattering phenomenon, where red-detuned light necessitates the absorption of a phonon via the anti-Stokes
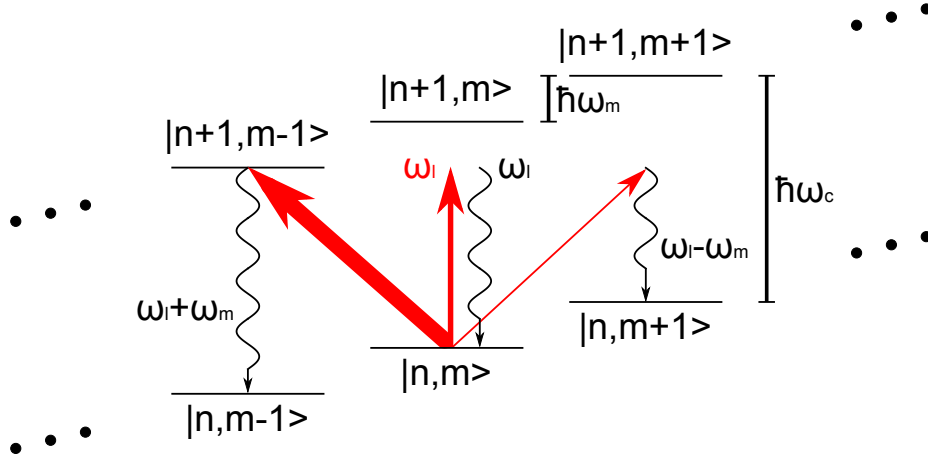
FIGURE 1.6.   Energy level diagram for an optomechanical system, showing the process of optomechanical cooling as a scattering phenomenon, with $|n, m\rangle$ representing the optical state, n, and the mechanical state, m. Different transitions can leave the system in a different mechanical state. By selecting laser light of frequency that is red detuned by ω_m, i.e. $\omega_l = \omega_c - \omega_m$, the $|n, m\rangle$ to $|n + 1, m - 1\rangle$ transition is preferred while the other two transitions are suppressed. Thus the anti-Stokes scattering reduces the mechanical population.

process[32–34], as shown in Fig. 1.6. Different transitions within Fig. 1.6 correspond to changes in the system's phonon number. Selecting laser light that is at the anti-Stokes position means that the favored transition is such that the phonon number decreases, thus cooling the system. This perspective is described in more detail in Chapter II.

Optomechanics also provides a means for performing precision measurements of the mechanical oscillator. The incredible precision of this arrangement has been implemented in both large and small systems, ranging from micron-sized polystyrene microspheres capable of detecting individual viruses[35] to kilometer-sized facilities, such as the LIGO facility, which was designed for detecting gravitational waves[36].

1.7. Dissertation Outline

The primary motivation for the work presented in this dissertation is the use of an optomechanical system as a means for manipulating optical signals. While many systems exist for optical communications, most of these systems involve processes that destroy the quantum state of the optical signal. Optomechanics provides a system where optical signals can be either stored or transferred to other optical frequencies in a manner that preserves the quantum state of the optical signal.

To lay the foundation for these goals, the first experiment presented in this work deals with the optomechanical analog to electromagnetically induced transparency (EIT). In atomic EIT, the opacity of an atomic medium with regards to a specific optical frequency is altered by the presence of light at a second optical frequency. That is to say that an optical "pump" beam is used to alter the transparency of the system with respect to an optical "probe" beam, with the two being of different frequencies. The optomechanical analog, known as optomechanically induced transparency or OMIT, accomplishes the same result but through the use of the mechanical oscillator[37]. This is done with a single optical mode and a single mechanical mode, with the probe beam being on-resonance with the optical mode and the pump beam being red-shifted to the anti-Stokes position. Previous work involving OMIT has examined its steady state behavior. The work presented in this dissertation involves the transient or time-domain behavior of OMIT, which is the topic of Chapter IV.

The transient OMIT experiments involve two optical pulses that arrive simultaneously. By introducing an additional optical pulse at a later time, this arrangement can be extended to become a means for storing an optical signal as a mechanical excitation, which is later converted back into an optical signal. In this

application, it is helpful to change the names of the respective optical pulses to match their function for light storage. The initial "pump" pulse is instead referred to as the "writing" pulse, while the "probe" pulse is instead the "signal" pulse. These two pulses arrive simultaneously, allowing the writing pulse to convert the signal into a mechanical excitation. At a later time, a "readout" pulse, which is also red-shifted to the anti-Stokes position, converts this mechanical excitation back into an optical signal that is at-resonance with the optical mode. This optomechanical light storage process is examined in Chapter V.

Finally, a second optical mode can be introduced to allow this system to convert an optical signal from one frequency to another, with each optical frequency corresponding to its own optical mode. This transition is facilitated by the mechanical oscillator, with both optical modes coupling to the same mechanical mode. An especially intriguing possibility with this arrangement is that the system can be put into a state where the two optical modes are coupled to each other but decoupled from the mechanical oscillator. This can be done even though the mechanical oscillator is the connecting link between the two optical modes. We refer to such a state as an "optomechanical dark mode", which is the topic of the eponymous chapter. This decoupling from the mechanical oscillator is fortuitous because it means that the optical transfer is protected from the unwanted contamination of the thermal background noise of the mechanical oscillator. Isolating the signal from the contamination of the thermal background noise means that this application can be performed with quantum signals at room temperature. This is in contrast to other arrangements which would require the mechanical mode to be cooled to its quantum ground state before working with quantum mechanical signals.

Individual chapters are dedicated to each of the three aforementioned topics; those topics being transient OMIT, optomechanical light storage, and the optomechanical dark mode. Prior to addressing these three topics, however, we shall first examine optomechanics theory in a more broad manner, as well as examining the aspects of the experimental apparatus that are mutually relevant to all of the individual topics.

CHAPTER II

OPTOMECHANICS THEORY

"There is a theory which states that if ever anyone discovers exactly what the Universe is for and why it is here, it will instantly disappear and be replaced by something even more bizarre and inexplicable. There is another theory which states that this has already happened."

– Douglas Adams, *The Hitchhiker's Guide to the Galaxy*

2.1. Coupling Light to Mechanical Vibrations

FIGURE 2.1. Schematic of a Fabry-Pérot optomechanical resonator.
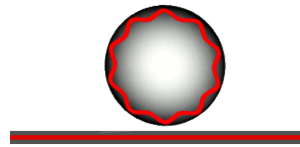
FIGURE 2.2. Schematic of a silica microsphere optomechanical resonator.

An optomechanical system consists of an optical resonator that is coupled to a mechanical oscillator. As introduced in Chapter I, one simple example of an optomechanical system is a Fabry-Pérot cavity in which one of the mirrors is mounted on a spring, which is shown schematically in Fig. 2.1. A Fabry-Pérot cavity by itself consists of two semi-reflective mirrors which face each other. Light enters by passing through one mirror, resonates between the two mirrors, and then exits through either mirror. Due to the boundary conditions, specific frequencies of light will resonate as optical modes within the cavity. By mounting one mirror on a spring, the Fabry-Pérot cavity can be made into an optomechanical system. The Fabry-Pérot cavity itself serves as an optical resonator, while the spring mounted mirror is a mechanical

oscillator. The optical modes can influence the mechanical modes through radiation pressure while the mechanical modes influence the optical modes by changing the length of the optical cavity.

The optomechanical system used for the work presented here is instead a silica microsphere, which is shown schematically in Fig. 2.2. In a microsphere, light is coupled into the sphere, circulates within the sphere, and then exits the sphere. The circulating light is confined through total internal reflection, and travels in a great circle along the surface of the sphere (i.e. around the sphere's equator). Due to the fact that the light loops back upon itself, these conditions form an optical resonator. The mechanical oscillator in this case is the mechanical breathing motion of the sphere itself. Once again, radiation pressure and the change in optical path length provide coupling between the optical cavity and the mechanical oscillator. More specifically, the circulating light exerts a radial radiation pressure force in order to maintain its circular trajectory, while the mechanical motion of the sphere's breathing modes changes the circumference through which the light must travel.

A more in depth description of the silica microsphere system can be found in Chapter III. For now, the preceding description provides a sufficient basis for our theoretical model. Additionally, while a silica microsphere is quite different from a Fabry-Pérot cavity, the two systems turn out to be mathematically equivalent, at least as far as optomechanics is concerned. After demonstrating this mathematical equivalency, which will be presented in the next section, it becomes unnecessary to differentiate between the two systems.

2.2. Hamiltonian Formulation

The Hamiltonians for an optical cavity $(\hat{H}_L)$ and for a mechanical oscillator $(\hat{H}_m)$ can be written as the following[32, 33, 38]:

$$\hat{H}_L = \hbar\omega_c \hat{a}^\dagger \hat{a} \tag{2.1}$$

$$\hat{H}_m = \hbar\omega_m \hat{b}^\dagger \hat{b}, \tag{2.2}$$

where $\hat{a}$ and $\hat{b}$ are the annihilation operators for the optical and mechanical modes, respectively, ω_c is the optical cavity resonance frequency, and ω_m is the frequency of resonance for the mechanical oscillator. It should be noted that the $1/2$ terms for the zero-point energy have been omitted from these Hamiltonians, as they will not have any effect on the dynamics of the system. We can now introduce the coupling between the optical cavity and the mechanical oscillator by relating the the optical resonance condition to the mechanical displacement, $\hat{x}$:

$$\omega_c(\hat{x}) = \omega_c + \frac{\delta\omega_c}{\delta\hat{x}}\hat{x} + \dots, \tag{2.3}$$

where ω_c on the right hand side of is now the optical resonance frequency in the absence of any mechanical displacement, and the ω_c previously shown in Eq. 2.1 corresponds to $\omega_c(\hat{x})$ on the left hand side of Eq. 2.3.

To find $\frac{\delta\omega_c}{\delta\hat{x}}$, we need an expression for ω_c in terms of $\hat{x}$. For a Fabry-Pérot cavity, ω_c can be related to the cavity round trip distance, L. The optical resonance condition is met when the length of the cavity is an integer multiple of the optical wavelength, λ:

$$n\lambda = L \tag{2.4}$$

18

Since $\omega_c = 2\pi c/\lambda$, we can now say that

$$\omega_c = \frac{2\pi nc}{L}. \qquad (2.5)$$

Since the constant term in the numerator will cancel itself out very soon, we can simplify this expression by saying

$$\omega_c = \frac{constant}{L}. \qquad (2.6)$$

Before proceeding further, we shall provide a similar treatment for a microsphere of radius R. Equation 2.6 is also applicable to the microsphere, but we need to write this expression to instead be in terms of R, the radius of the sphere. Here, the cavity length, L, is given by the circumference of a great circle of the sphere, which is to say that $L = C_{\text{“greatcircle”}} = 2\pi R$. Since it is now shown that the effective cavity length for the microsphere is directly proportional to its radius, an expression identical to Eq. 2.6 can be written for a microsphere:

$$\omega_c = \frac{constant}{R}. \qquad (2.7)$$

The only difference between the Fabry-Pérot cavity and the microsphere is in the constant term in the numerator, which is about to cancel itself out. With the Fabry-Pérot cavity or with the microsphere, the mechanical displacement causes a change in L or R, respectively, with both L and R having a linear dependence on $\hat{x}$. In this context, it can be seen that both the Fabry-Pérot cavity and the microsphere are mathematically identical, with L and R being interchangeable. Past this point it is no longer necessary to treat the two separately.

Differentiating Eq. 2.6 or 2.7 gives us the following (for either system),

$$\frac{\delta\omega_c}{\delta\hat{x}} = \frac{-constant}{R^2} = \frac{-1}{R}\left(\frac{constant}{R}\right) = \frac{-\omega_c}{R}, \tag{2.8}$$

which, along with Eq. 2.3, can be inserted into the optical Hamiltonian from Eq. 2.1 to give a complete Hamiltonian for an optomechanical system:

$$\hat{H} = \hat{H}_L + \hat{H}_m = \hbar\omega_c\hat{a}^\dagger\hat{a} + \hbar\omega_m\hat{b}^\dagger\hat{b} - \hbar\frac{\omega_c}{R}\hat{a}^\dagger\hat{a}\hat{x}, \tag{2.9}$$

It is now also beneficial to switch to a frame of reference rotating at the frequency of the driving laser, ω_L. This is done by applying a unitary transformation $\hat{U} = exp(i\omega_L\hat{a}^\dagger\hat{a}t)$, which, at this point, essentially has the effect of adding a new term of $-\hbar\omega_L\hat{a}^\dagger\hat{a}$ to the Hamiltonian. It should be mentioned, however, that shifting to this rotating frame would also have the effect of removing the time dependence from the driving laser's driving term. This driving term has not been introduced yet, however, but it will be introduced in Section 2.3. Since we are shifting to the rotating frame now, it will be unnecessary to include the time dependence in the driving term when it is introduced in Section 2.3. This is important to remember because later on, in Section 2.5, it will become necessary to undo our shift to the rotating reference frame.

That said, shifting to the rotating frame of reference gives us a new Hamiltonian of the form

$$\hat{H} = \underbrace{-\hbar\Delta\hat{a}^\dagger\hat{a} + \hbar\omega_m\hat{b}^\dagger\hat{b}}_{\hat{H}_0} - \underbrace{\hbar\frac{\omega_c}{R}\hat{a}^\dagger\hat{a}\hat{x}}_{\hat{H}_{int}}. \tag{2.10}$$

where $\Delta = \omega_L - \omega_c$ is the detuning of the driving laser. The interaction Hamiltonian, labeled $\hat{H}_{int}$, contains the optomechanical interaction, so this is the part that we are

more interested in (while $\hat{H}_0$ contains everything else):

$$\hat{H}_{int} = -\hbar \frac{\omega_c}{R} \hat{a}^\dagger \hat{a} \hat{x} \tag{2.11}$$

Note that the negative sign in $\hat{H}_{int}$ is sometimes dropped in some literature. This can be justified by saying that $x > 0$ would indicate a decrease in cavity length. For the sake of simplicity, however, we will keep the negative sign.

As an aside, at this point it is possible to find an expression for the radiation pressure force, $\hat{F}$, by differentiating $\hat{H}_{int}$ with respect to $\hat{x}$.

$$\hat{F} = -\frac{d\hat{H}_{int}}{d\hat{x}} = -\frac{d}{d\hat{x}} \left(-\hbar \frac{\omega_c}{R} \hat{a}^\dagger \hat{a} \hat{x} \right) = \hbar \frac{\omega_c}{R} \hat{a}^\dagger \hat{a} \tag{2.12}$$

For a sanity check, this expression can be compared to what we would get from simply examining the change in momentum of photons colliding with the Fabry-Pérot end-mirror. Each individual photon carries a momentum of $\hbar\omega_c/c$, so the momentum change due to the collision of a single photon is $2\hbar\omega_c/c$. This event occurs once per round trip of the photon, with the round trip time being $\tau_c = 2L/c$. Since the number of photons is given by $\hat{a}^\dagger \hat{a}$, the total radiation force is given by

$$\hat{F} = \frac{2\hbar\omega_c}{c} \frac{\hat{a}^\dagger \hat{a}}{\tau_c} = \hbar \frac{\omega_c}{L} \hat{a}^\dagger \hat{a}, \tag{2.13}$$

which agrees with the result from the Hamiltonian formulation (recalling that L and R are interchangeable).

Returning to the interaction Hamiltonian in Eq. 2.11, we can examine $\hat{x}$ to allow us to write $\hat{H}_{int}$ in terms of $\hat{b}$ and $\hat{b}^\dagger$, which will paint a clearer picture of the optomechanical interaction. The operator $\hat{x}$ depends on the zero point fluctuation of

21

the mechanical mode (x_{zpf}), the effective mass of the mechanical oscillator (m), and on the phonon annihilation operator as follows:

$$\hat{x} = x_{zpf}(\hat{b} + \hat{b}^\dagger) \tag{2.14}$$

$$x_{zpf} = \sqrt{\frac{\hbar}{2m\omega_m}} \tag{2.15}$$

We can also introduce g_0, which is the coupling rate between a single photon and a single phonon,

$$g_0 = \frac{\omega_c}{R}x_{zpf} \tag{2.16}$$

Equations 2.14, 2.15, and 2.16 can be substituted into the interaction Hamiltonian to yield

$$\hat{H}_{int} = -\hbar g_0 \hat{a}^\dagger \hat{a}(\hat{b} + \hat{b}^\dagger). \tag{2.17}$$

Note that the process described by the Hamiltonian in Eq. 2.17 involves three operators, and hence is nonlinear. However, we can apply the mean-field approximation, treating the the optical field as the sum of a large classical average value and a small varying term. This will allow us to linearize the interaction Hamiltonian with respect to the weak varying term.

$$\hat{a} \approx \bar{\alpha} + \delta\hat{a}, \tag{2.18}$$

where $\bar{\alpha}^*\bar{\alpha} = \bar{n}_c$ is the average classical photon number and $\delta\hat{a}$ is the annihilation operator for the weak varying field. $\hat{a}^\dagger\hat{a}$ now becomes

$$\begin{aligned}
\hat{a}^\dagger\hat{a} &= (\bar{\alpha}^* + \delta\hat{a}^\dagger)(\bar{\alpha} + \delta\hat{a}) \\
&= \bar{\alpha}^*\bar{\alpha} + \bar{\alpha}^*\delta\hat{a} + \bar{\alpha}\delta\hat{a}^\dagger + \delta\hat{a}^\dagger\delta\hat{a}.
\end{aligned} \tag{2.19}$$

The $\delta\hat{a}^\dagger\delta\hat{a}$ term can be discarded because it is negligible in comparison to the other terms. Substituting the remaining expression for $\hat{a}^\dagger\hat{a}$ into the interaction Hamiltonian yields

$$\hat{H}_{int} = -\hbar g_0(\bar{\alpha}^*\bar{\alpha} + \bar{\alpha}^*\delta\hat{a} + \bar{\alpha}\delta\hat{a}^\dagger)(\hat{b} + \hat{b}^\dagger). \tag{2.20}$$

Here, the $\bar{\alpha}^*\bar{\alpha}$ term (when combined with $\hat{b}$ and $\hat{b}^\dagger$) describes an average, non-fluctuating radiation force, and can be removed by shifting our definition of the origin for the mechanical displacement. Removing this term, and then distributing the remaining terms, gives us

$$\hat{H}_{int} = -\hbar g_0(\alpha^*\delta\hat{a}\hat{b} + \alpha\delta\hat{a}^\dagger\hat{b}^\dagger) - \hbar g_0(\alpha^*\delta\hat{a}\hat{b}^\dagger + \alpha\delta\hat{a}^\dagger\hat{b}) \tag{2.21}$$

Additionally, we can simplify $\hat{H}_{int}$ further by assuming that $\bar{\alpha}$ is real-valued, i.e. $\bar{\alpha} = \sqrt{\bar{n}_c}$. This allows us to factor out $\sqrt{\bar{n}_c}$ and then make the substitution

$$g = g_0\sqrt{\bar{n}_c}, \tag{2.22}$$

which produces an interaction Hamiltonian of

$$\hat{H}_{int} = \underbrace{-\hbar g(\delta\hat{a}\hat{b} + \delta\hat{a}^\dagger\hat{b}^\dagger)}_{\text{"Parametric Down-conversion"}} - \underbrace{\hbar g(\delta\hat{a}\hat{b}^\dagger + \delta\hat{a}^\dagger\hat{b})}_{\text{"Beam-Splitter"}}. \tag{2.23}$$

The full, linearized Hamiltonian is now

$$\hat{H} = -\hbar\Delta\delta\hat{a}^\dagger\delta\hat{a} + \hbar\omega_m\hat{b}^\dagger\hat{b} - \hbar g(\delta\hat{a}\hat{b} + \delta\hat{a}^\dagger\hat{b}^\dagger) - \hbar g(\delta\hat{a}\hat{b}^\dagger + \delta\hat{a}^\dagger\hat{b}). \tag{2.24}$$

The effective optomechanical coupling strength, g, performs much the same role as g_0, except that g depends on the strength of the control field, $\bar{n}_c$. This dependence

on $\bar{n}_c$ is a crucial feature because it means that the effective optomechanical coupling strength can be controlled by changing the strength of the control field.

Controlling the effective optomechanical coupling strength in this manner makes processes like optomechanical light storage possible. In optomechanical light storage, which is covered in Chapter V, an on-resonant optical "signal" pulse is sent to the microresonator at the same time as the red-detuned control pulse. This allows the control pulse to act as a "writing" pulse because it allows the on-resonant signal pulse to interact with the mechanical mode. At a later time, a second control pulse can be sent (by itself, with no signal pulse), this time acting as a "reading" pulse. The reading pulse again allows the mechanical mode to interact with the on-resonant field, which converts the mechanically stored signal back into an optical signal. All of this is made possible by the $\bar{n}_c$ dependence of g.

It is important to observe that the processes described by the interaction Hamiltonian in Eq. 2.23 take the form of scattering phenomena. In the Stokes and anti-Stokes processes, by selecting laser light that is off-resonance, the mechanical oscillator can be heated or cooled by creating or destroying phonons. In the anti-Stokes process, red detuned light causes a phonon to be absorbed; in the Stokes process, blue detuned light causes the creation of a phonon. This process effectively allows us to map a photon state to a phonon state, and *vice versa*, which is fundamental to all of the specific optomechanical processes that will be covered here.

In our case, we are primarily interested in what happens when the control laser is at the anti-Stokes resonance condition, which allows us to focus our attention on several terms in the interaction Hamiltonian in particular. The first half of the interaction Hamiltonian of Eq. 2.23 has a form that is analogous to the Hamiltonian for parametric down-conversion. The second half of Eq. 2.23 has the form of a

beam-splitter Hamiltonian. In the resolved sideband regime, where the mechanical frequency is significantly larger than the mechanical linewidth [39, 40], it is possible to select one set of terms or the other by changing the detuning of the control laser, Δ. When $\Delta \approx -\omega_m$, i.e. the optical control field is near the anti-Stokes position, the beam-splitter type terms dominate. Eliminating the parametric down-conversion type terms from our full, linearized Hamiltonian (Eq. 2.24) gives us

$$\hat{H} = -\hbar\Delta\delta\hat{a}^\dagger\delta\hat{a} + \hbar\omega_m\hat{b}^\dagger\hat{b} - \hbar g(\delta\hat{a}\hat{b}^\dagger + \delta\hat{a}^\dagger\hat{b}). \tag{2.25}$$

Note that under the Stokes condition ($\Delta \approx \omega_m$), however, the parametric down-conversion type terms would instead dominate. The experiments presented in this thesis were performed with the $\Delta \approx -\omega_m$.

2.3. Equations of Motion

The Heisenberg Equation can be used to find the equations of motion for this system:

$$\frac{d\delta\hat{a}}{dt} = \frac{1}{i\hbar}[\delta\hat{a}, \hat{H}]$$
$$\frac{d\hat{b}}{dt} = \frac{1}{i\hbar}[\hat{b}, \hat{H}] \tag{2.26}$$

Using the above with the full Hamiltonian from Eq. 2.25 yields the following equations of motion:

$$\frac{d\delta\hat{a}}{dt} = i\Delta\delta\hat{a} + ig\hat{b}$$
$$\frac{d\hat{b}}{dt} = -i\omega_m\hat{b} + ig\delta\hat{a} \tag{2.27}$$

Up until this point damping and driving effects have not been taken into account for either the mechanical oscillator or the optical resonator. Damping and driving do not affect the interaction Hamiltonian, but now that we have turned our interest

to the equations of motion it is desirable to introduce these effects. Damping and driving manifest themselves as additional terms in $\hat{H}_L$ and $\hat{H}_m$, and subsequently additional terms in $\hat{H}$. We can introduce these effects at this point by simply adding them to the equations of motion:

$$\begin{aligned}
\frac{d\delta\hat{a}}{dt} &= \left(i\Delta - \frac{\kappa}{2}\right)\delta\hat{a} + ig\hat{b} + \sqrt{\kappa_{ex}}\delta\hat{s}_p + \sqrt{\kappa_0}\hat{f}_{in} \\
\frac{d\hat{b}}{dt} &= \left(-i\omega_m - \frac{\Gamma_m}{2}\right)\hat{b} + ig\delta\hat{a} + \sqrt{\Gamma_m}\hat{b}_{in}
\end{aligned} \tag{2.28}$$

Here we have introduced several decay rates. κ_{ex} is the cavity decay rate associated with input coupling, i.e. whatever method is used to get light into the optical cavity. κ_0 is the optical decay rate for everything else, including scattering and absorption. κ is the overall optical cavity decay rate, with $\kappa = \kappa_{ex} + \kappa_0$. Γ_m is the decay rate for the mechanical oscillator, which includes clamping losses due to the supporting stem of the microsphere, viscous damping due to the surrounding gas, and all other sources of mechanical damping. $\hat{f}_{in}$ and $\hat{b}_{in}$ are the quantum or thermal noise for the optical cavity and the mechanical oscillator, respectively. For the optical frequencies and experimental conditions we are concerned with, $\left\langle \hat{f}_{in} \right\rangle = 0$, so the $\sqrt{\kappa_0}\hat{f}_{in}$ term can be ignored.

$\hat{b}_{in}$, however, is nonzero at room temperature, as a consequence of the thermal energy of in the experimental chamber. The presence of this thermal noise means that the mechanical mode is already populated with thermal phonons. This poses a problem if the desire is to use the mechanical mode to store quantum information, given that the thermal background will swamp any sort of quantum signal. However, this issue can be circumvented by the use of an optomechanical dark mode, which is the topic of Chapter VI.

In Eq. 2.28, we have also introduced several new fields to describe the input probe laser. $\hat{s}_p$ is the input probe optical field, due to the probe laser, such that the input probe power is $P_p = \hbar\omega_c \langle \hat{s}_p^\dagger \hat{s}_p \rangle$. The frequency of the probe laser is ω_p, so $\hat{s}_p$ would have a frequency of ω_p, i.e. $\hat{s}_p = \bar{s}_p e^{-i\omega_p}$. Since we are currently in a frame of reference rotating at the frequency of the driving laser, ω_L, Eq. 2.28 instead uses $\delta\hat{s}_p$, with $\delta\hat{s}_p = \bar{s}_p e^{-i(\omega_p-\omega_L)t}$. Thus the $\sqrt{\kappa_{ex}}\delta\hat{s}_p$ term is the driving term as a consequence of the probe laser.

2.4. Steady State Solution and OMIT

The equations of motion presented in Eq.2.28 can be solved analytically to find the steady state behavior of the system. Doing so will demonstrate that our system will display the effect of optomechanically induced transparency(OMIT)[41].

We first make an educated guess that our solutions for $\delta\hat{a}$ and $\hat{b}$ will take the following forms[37]:

$$\delta\hat{a} = A^- e^{-i\Omega t} + A^+ e^{+i\Omega t}$$
$$\hat{b} = B^- e^{-i\Omega t} + B^+ e^{+i\Omega t}$$

(2.29)

Here, $\Omega = \omega_p - \omega_L$ is the spectral separation between the pump and probe lasers. Our goal is to find a spectrum of the OMIT dip as a function of an adjustable ω_p, so at this point Ω is our adjustable parameter. This educated guess is based partly on the fact that $\delta\hat{s}_p = \bar{s}_p e^{-i(\omega_p-\omega_L)t} = \bar{s}_p e^{-i\Omega t}$. The time derivatives are subsequently

$$\frac{d\delta\hat{a}}{dt} = -i\Omega A^- e^{-i\Omega t} + i\Omega A^+ e^{+i\Omega t}$$
$$\frac{d\hat{b}}{dt} = -i\Omega B^- e^{-i\Omega t} + i\Omega B^+ e^{+i\Omega t}.$$

(2.30)

We can now plug Eqs. 2.29 and 2.30 into Eq. 2.28. In this specific solution we are not interested in the contribution of the mechanical thermal noise, so we will drop that term. Doing so, we obtain the following set of equations:

$$
\begin{aligned}
- i\Omega A^- & e^{-i\Omega t} + i\Omega A^+ e^{+i\Omega t} \\
&= \left(i\Delta - \frac{\kappa}{2} \right) A^- e^{-i\Omega t} + \left(i\Delta - \frac{\kappa}{2} \right) A^+ e^{+i\Omega t} \\
&\qquad + ig B^- e^{-i\Omega t} + ig B^+ e^{+i\Omega t} + \sqrt{\kappa_{ex}}\, \bar{s}_p e^{-i\Omega t}
\end{aligned}
$$

(2.31)

$$
\begin{aligned}
- i\Omega B^- & e^{-i\Omega t} + i\Omega B^+ e^{+i\Omega t} \\
&= \left(-i\omega_m - \frac{\Gamma_m}{2} \right) B^- e^{-i\Omega t} + \left(-i\omega_m - \frac{\Gamma_m}{2} \right) B^+ e^{+i\Omega t} \\
&\qquad + ig A^- e^{-i\Omega t} + ig A^+ e^{+i\Omega t}
\end{aligned}
$$

If we focus only on the terms involving $e^{-i\Omega t}$, we get

$$
\begin{aligned}
-i\Omega A^- &= \left(i\Delta - \frac{\kappa}{2} \right) A^- + ig B^- + \sqrt{\kappa_{ex}}\, \bar{s}_p \\
-i\Omega B^- &= \left(-i\omega_m - \frac{\Gamma_m}{2} \right) B^- + ig A^-.
\end{aligned}
$$

(2.32)

It is possible to come up with two more equations that involve A^+ and B^+ by examining the terms involving $e^{+i\Omega t}$. However, we are not particularly interested in the terms involving $e^{+i\Omega t}$, since $A^+ \approx 0$ in the resolved sideband regime. Thus it is A^- that we are interested in.

We can now solve Eq. 2.32 algebraically for A^-. Doing so results in an intracavity field of

$$
A^- = \frac{\left(\frac{\Gamma_m}{2} - i(\Omega - \omega_m) \right) \sqrt{\kappa_{ex}}\, \bar{s}_p}{\left(\frac{\kappa}{2} - i(\Omega + \Delta) \right) \left(\frac{\Gamma_m}{2} - i(\Omega - \omega_m) \right) + g^2}.
$$

(2.33)

28

This expression can be further simplified by making the assumption that the optomechanical coupling is weak compared to the optical losses of the system. This allows for the approximation $\left(\frac{\kappa}{2} - i(\Delta + \Omega)\right) \approx \frac{\kappa}{2}$. To make these equations cleaner, we also introduce $\Delta_p \equiv \Omega - \omega_m$, which is the detuning of the probe laser away from the optical cavity resonance. Doing so gives us an intracavity field of the following form:

$$A^- = \frac{\left(\frac{\Gamma_m}{2} - i\Delta_p\right)\sqrt{\kappa_{ex}}\bar{s}_p}{\frac{\kappa}{2}\left(\frac{\Gamma_m}{2} - i\Delta_p\right) + g^2}. \tag{2.34}$$

We can now relate this expression to the transmitted optical field, viz. the light that is coupled back into the waveguide by the microsphere, or equivalently the light that is reflected by the Fabry-Pérot cavity. This transmitted optical field is given by[22]

$$\hat{s}_{out} = \hat{s}_{in} - \sqrt{\kappa_{ex}}\hat{a}, \tag{2.35}$$

where $\hat{s}_{in}$ is the total input optical field from all lasers. This includes both the pump laser (also referred to as the control laser), with an input optical field of $\hat{s}_c$, and the probe laser (also referred to as the signal laser), with an input optical field of $\hat{s}_p$. Thus the total input optical field is $\hat{s}_{in} = \hat{s}_c + \hat{s}_p$. The expression for the transmitted optical field can be broken down into components relative to each relevant optical frequency:

$$\hat{s}_{out} = (\hat{s}_c - \sqrt{\kappa_{ex}}\bar{\alpha})e^{-i\omega_c t} + (\hat{s}_p - \sqrt{\kappa_{ex}}A^-)e^{-i\omega_p t} \tag{2.36}$$

At this point, we can now connect our derivation to an experimentally testable quantity. The transmission of the probe beam, which can be measured experimentally, is defined as being the ratio between the output and input optical field amplitudes at

the probe frequency:

$$t_p = \frac{\hat{s}_p - \sqrt{\kappa_{ex}}\delta\hat{a}}{\hat{s}_p} = 1 - \frac{\left(\frac{\Gamma_m}{2} - i\Delta_p\right)\kappa_{ex}}{\frac{\kappa}{2}\left(\frac{\Gamma_m}{2} - i\Delta_p\right) + g^2} \tag{2.37}$$

This expression, however, includes all of the less interesting effects of optical coupling into the optical cavity. In order to examine the OMIT process by itself, it is desirable to normalize the transmission to remove the effects of optical coupling. This can be done by finding the residual on-resonance ($\Delta_p = 0$) transmission for the probe laser as it would appear in the absence of the pump laser ($g = 0$), and then subtracting this residual from t_p. This residual is

$$t_p(\Delta_p = 0, g = 0) = 1 - 2\frac{\kappa_{ex}}{\kappa}, \tag{2.38}$$

and thus the normalized probe transmission is

$$t'_p = t_p - t_p(\Delta_p = 0, g = 0) = 1 - \frac{-\left(\frac{\Gamma_m}{2} - i\Delta_p\right)\kappa_{ex}}{\frac{\kappa}{2}\left(\frac{\Gamma_m}{2} - i\Delta_p\right) + g^2} - 1 + 2\frac{\kappa_{ex}}{\kappa} = \frac{2\frac{\kappa_{ex}}{\kappa}g^2}{\frac{\kappa}{2}\left(\frac{\Gamma_m}{2} - i\Delta_p\right) + g^2}. \tag{2.39}$$

One final simplification can be made by assuming the case of critical coupling into the optical cavity, which means that $\kappa_{ex}/\kappa = 1/2$.

$$t'_p = \frac{g^2}{\frac{\kappa}{2}\left(\frac{\Gamma}{2} - i\Delta_p\right) + g^2} = \frac{\frac{(2g)^2}{\kappa}}{\Gamma_m + \frac{(2g)^2}{\kappa} - 2i\Delta_p} \tag{2.40}$$

In terms of optical power, the probe transmission is

$$|t'_p|^2 = \frac{\frac{(2g)^4}{\kappa^2}}{\left(\Gamma_m + \frac{(2g)^2}{\kappa}\right)^2 + (2\Delta_p)^2}. \tag{2.41}$$

30

This is the spectrum of the OMIT dip as a function of the detuning of the probe laser, Δ_p. This shows that the OMIT dip has a Lorentzian line shape. The half-width at half-maximum for this OMIT dip is

$$\gamma_{OMIT} = \Gamma_m + \frac{(2g)^2}{\kappa}, \tag{2.42}$$

and the peak value is

$$|t_p'(\Delta_p = 0)|^2 = \frac{\frac{(2g)^4}{\kappa^2}}{\left(\Gamma_m + \frac{(2g)^2}{\kappa}\right)^2}. \tag{2.43}$$

It is customary and convenient at this point to introduce the optomechanical cooperativity, $C = (2g)^2/\Gamma_m\kappa$, which allows the width and height of the OMIT dip to be expressed more simply as

$$\gamma_{OMIT} = \Gamma_m(1 + C) \tag{2.44}$$

$$|t_p'(\Delta_p = 0)|^2 = \left(\frac{C}{1+C}\right)^2. \tag{2.45}$$

2.5. Transient Solution and Light Storage

The Hamiltonian in Eq. 2.25 has a form that allows for state transfer and Rabi oscillations. To see this, we shall first examine the general case for the state transfer process for a two level system. Here we start with a system whose Hamiltonian has the form

$$\hat{H} = \underbrace{E_1 |1\rangle \langle 1| + E_2 |2\rangle \langle 2|}_{\hat{H}_0} + \underbrace{\gamma_{Rabi} e^{i\omega t} |1\rangle \langle 2| + \gamma_{Rabi} e^{-i\omega t} |2\rangle \langle 1|}_{\hat{H}_{int}}. \tag{2.46}$$

This system has an exact solution[42]:

$$c_1(0) = 1, \qquad c_2(0) = 0, \tag{2.47}$$

$$|c_2(t)|^2 = \frac{\gamma_{Rabi}^2/\hbar^2}{\gamma_{Rabi}^2/\hbar^2 + (\omega - \omega_{21})^2/4} \sin^2\left[\left(\frac{\gamma_{Rabi}^2}{\hbar^2} + \frac{(\omega - \omega_{21})^2}{4}\right)^{1/2} t\right], \tag{2.48}$$

$$|c_1(t)|^2 = 1 - |c_2(t)|^2. \tag{2.49}$$

In the above, we define $\omega_{21} \equiv (E_2 - E_1)/\hbar$, and set the system in the initial configuration where only c_1 is populated. Equation 2.48 shows the characteristic Rabi oscillation, where the population oscillates between c_1 and c_2 as time goes on. The frequency of this oscillation, known as the Rabi frequency, is given by

$$\Omega_{Rabi} = \sqrt{\left(\frac{\gamma_{Rabi}^2}{\hbar^2}\right) + \frac{\omega - \omega_{21}}{4}}. \tag{2.50}$$

Note that if $\omega = \omega_{21}$, the amplitude of the Rabi oscillation becomes such that a complete state transfer occurs with each oscillation and the Rabi frequency becomes

$$\Omega_{Rabi} = \frac{\gamma_{Rabi}}{\hbar}. \tag{2.51}$$

If ω is detuned away from ω_{21}, the amplitude of the oscillation decreases, with a smaller peak value for $|c_2(t)|^2$.

To complete the connection to optomechanics, we must remember that the optomechanical Hamiltonian presented in Eq. 2.25 is in the rotating frame of reference. If we undo the shift to the rotating reference frame, the Hamiltonian of Eq. 2.25 is instead

$$\hat{H} = \hbar\omega_c \delta\hat{a}^\dagger \delta\hat{a} + \hbar\omega_m \hat{b}^\dagger \hat{b} - \hbar g(e^{i\omega_L t}\delta\hat{a}\hat{b}^\dagger + e^{-i\omega_L t}\delta\hat{a}^\dagger \hat{b}). \tag{2.52}$$

Now it becomes apparent that the optomechanical Hamiltonian in Eq. 2.52 is of exactly the same form as the Hamiltonian in Eq. 2.46 which gave rise to Rabi oscillations. Note that since $\omega_c > \omega_m$, E_2 corresponds to $\hbar\omega_c$ and E_1 corresponds to $\hbar\omega_m$. In this case, the resonance condition is met when $\omega_L = \omega_c - \omega_m$, i.e. when $\Delta = -\omega_m$, which is what is to be expected. γ_{Rabi} corresponds to $\hbar g$, so the on-resonance Rabi frequency is given by

$$\Omega_{Rabi} = g. \tag{2.53}$$

It should also be mentioned that, strictly speaking, the analogy could be made more exact by instead saying that $c_1(0) = 0$ and $c_2(0) = 1$ (since we want the population to start in the optical mode), but the consequence of this reversal is simply a phase shift by half a cycle.

This configuration can be taken a step further and used as a mechanism for storing an optical signal as a mechanical excitation. This is accomplished simply by turning off the on-resonance control laser after half of a Rabi cycle. The signal can then be later retrieved by applying the on-resonance control laser again for another half of a Rabi cycle. This can be described mathematically by allowing g to vary with respect to time. With $\Delta = -\omega_m$, and continuing with our previous example,

$$|\hat{b}(t)|^2 = sin^2\left[\theta(t)\right], \tag{2.54}$$

where $\theta(t) = \int_0^\tau g(t)dt$. Note that the time evolution is governed by a sin^2 function, so one full cycle corresponds to $\theta(\tau) = \pi$. Thus by pulsing the control laser such that $\theta(\tau) = \pi/2$, we leave the system in a state where $|\hat{b}(\tau)|^2$ is populated.

In a more general sense, we can write the time evolution of the system as follows:

$$\delta\hat{a}(t) = \left(\delta\hat{a}(0)\cos[\theta(t)] - i\hat{b}(0)\sin[\theta(t)]\right)e^{-i\omega_c t} \tag{2.55}$$

$$\hat{b}(t) = \left(\hat{b}(0)\cos[\theta(t)] - i\delta\hat{a}(0)\sin[\theta(t)]\right)e^{-i\omega_m t} \tag{2.56}$$

Written in this manner, we can clearly see that a "$\pi/2$ pulse", i.e. $\theta(\tau) = \pi/2$, swaps the optical and mechanical states. This allows the control laser's $\pi/2$ pulse to act as either a "writing" or "reading" pulse, thus providing the mechanism for light storage that will be presented experimentally in Chapter V.

2.6. Summary

In this chapter, the interaction Hamiltonian and the equations of motion have been derived for our optomechanical system. We have examined the steady state solution in the absence of damping, which gave rise to the effect of OMIT. The transient solution was also presented, giving us the foundation for optomechanical light storage. This informs us as to what to expect from our system in the following experimental chapters.

The examples derived in this chapter for OMIT and optomechanical light storage were performed in the absence of damping. These damping effects, however, are intrinsic to the experimental observations. As such, many of the theoretical predictions that accompany experimental measurements are found by numerically solving the equations of motion, such as those presented in Eq. 2.28.

It bears repeating that the effective optomechanical coupling rate, g, which is present in both the interaction Hamiltonian and the equations of motion, is dependent upon the strength of the anti-Stokes positioned control laser. As such, this allows the

strength of the optomechanical coupling to be controlled by the strength of the control laser. This effect plays a prominent role in all of the experiments in this dissertation.

CHAPTER III

EXPERIMENTAL APPARATUS

"Experience without theory is blind, but theory without experience is mere intellectual play."

– Immanuel Kant

3.1. Silica Microspheres

While the Fabry-Pérot cavity with a movable end-mirror provides a simple example for describing optomechanics theory, there is a wide variety of elegant optomechanical systems that have been developed for experimental work[43]. Such systems include silicon nitride membranes[44], silica microtoroids[45], and mirror coated AFM cantilevers[46], to name just a few. For the experiments discussed in this dissertation, however, the optomechanical system is a silica microsphere[1, 25], shown schematically in Fig. 3.1. Figure 3.2 shows an image of an actual microsphere.

Silica microspheres were chosen for their simplicity, which presents them as a preferable platform for performing proof of principle procedures. The typical diameter for our microspheres is 30 μm. Light is coupled into the sphere, travels around a great circle of the sphere due to total internal reflection, and then exits the sphere. Similar to the Fabry-Pérot cavity, the microsphere also has boundary conditions which support a harmonic series of optical modes. The optical modes of silica microspheres are commonly referred to as "whispering gallery modes" [47]. This somewhat whimsical term is a reference to a similar phenomenon that can be observed with sound waves in large buildings with domed ceilings.
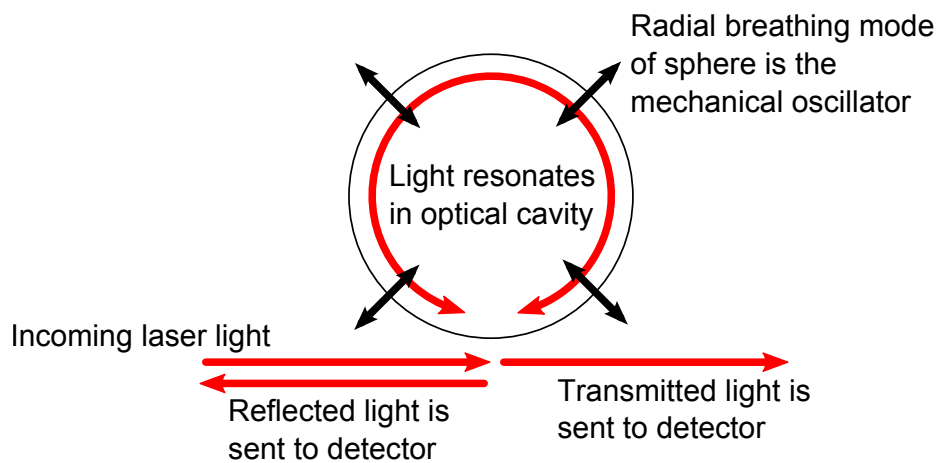
FIGURE 3.1. Schematic of a silica microsphere.
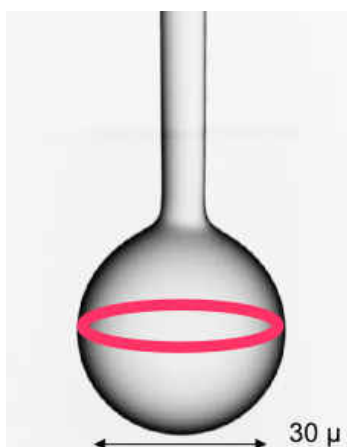
FIGURE 3.2. Image of a microsphere, with the path of the optical cavity drawn for clarity. Note the presence of the stem, which is how the sphere is held in place.
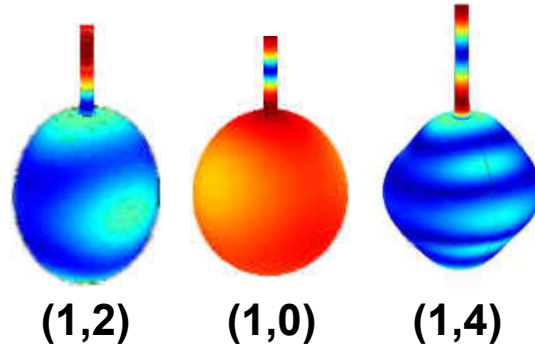
FIGURE 3.3. Finite element analysis of three relevant mechanical modes in silica microspheres. (n,l) indicate the radial (n) and angular (l) quantum numbers.[1]

In a silica microsphere, the vibrations of the sphere itself play the role of the mechanical oscillator, some of which are show in Fig. 3.3. There are different modes of oscillation, each exhibiting a different frequency relative to the others, as can be seen in Fig. 3.4. The modes are typically labeled with their quantum numbers, (n,l), with n being the radial quantum number and l being the angular. There are advantages and disadvantages involved when selecting a specific mechanical mode for experiments. For example, the (1,2) can be convenient because it is the lowest frequency mode. At the same time, the (1,2) mode can suffer from a distorted spectral shape owing to a badly deformed sphere breaking the mode's degeneracy. The (1,2) mode was used for most of the work presented in this dissertation.

The frequency of the mechanical modes is also affected by the diameter of the microsphere, as shown in Fig. 3.5. Our experiments typically use a microsphere near 30 μm. This size was chosen based on the ability to reliably fabricate a sphere with the desired deformity and the desired ratio of sphere diameter to stem diameter.

Moving on in our treatment of silica microspheres, we will now examine the coupling between the optical and mechanical modes. This coupling is easiest to conceptualize by considering the fundamental radial breathing mechanical mode,

38
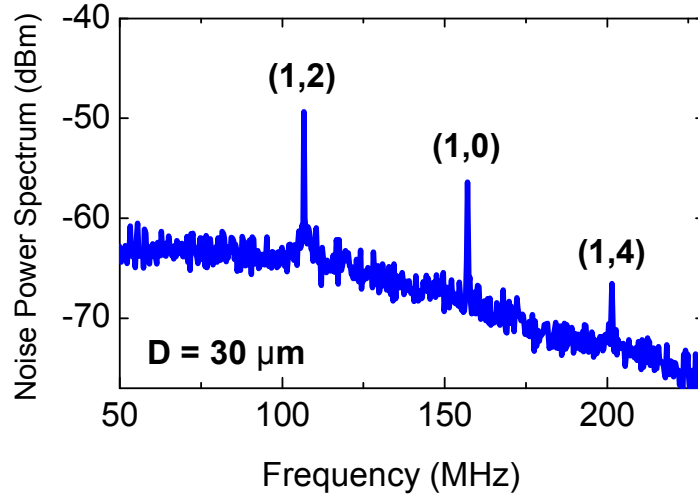
FIGURE 3.4. Noise power spectrum of a typical silica microsphere, with a diameter of 30 μm, showing the spectral position of the three most relevant mechanical modes.[1]

the (1,0) mode, in which the entire radius of the sphere uniformly expands and contracts. The radiation pressure from the whispering gallery modes is radial, and is a consequence of the curved path that the light follows, as shown in Fig. 3.6. Since the mechanical oscillator's ability to influence the optical cavity relies on changing the optical path length, only vibrational modes that change the sphere's circumference will affect the optical cavity. Such modes are said to be "optically active". All of the modes depicted in Figs. 3.3, 3.4, and 3.5 are optically active.

The desire for high quality factors, both mechanical and optical, is one of the chief motivations behind the development of the previously mentioned assortment of optomechanical systems. Indeed, the different quality factors are one of the major trade-offs that differentiates one system from another. Other considerations include the the overall size of the system, as well as the optomechanical coupling rate, i.e. how well the optical cavity and mechanical oscillator are able to influence one another. A complete comparison between these devices is beyond the scope of this work. Such a comparison can be found in [22]. In this regard, the microsphere system chosen for this
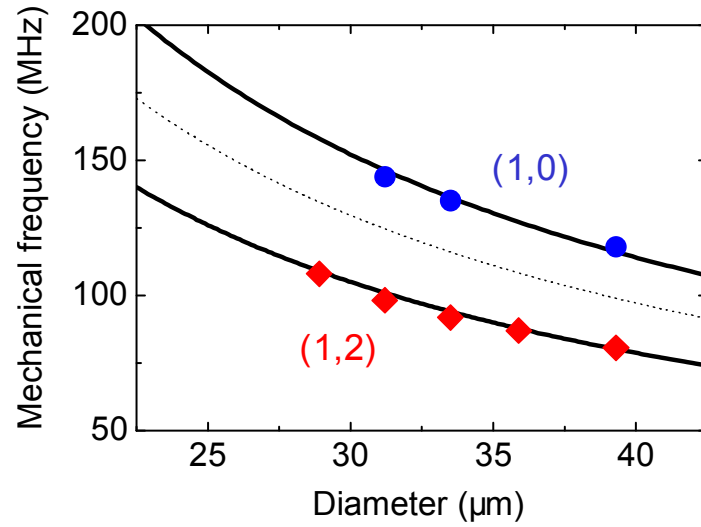
FIGURE 3.5. Effect of microsphere size on the frequencies of two mechanical modes.[1]
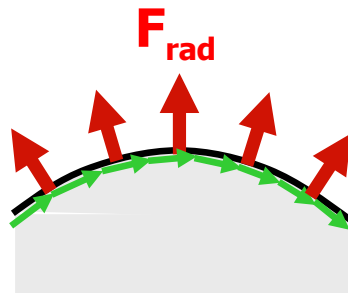
FIGURE 3.6. The radiation force in a microsphere is radial, as a consequence of the curved optical path. Green arrows denote the optical path as it follows the curved surface of the sphere, while red arrows indicate the radial radiation force.

work might be described as a jack of all trades, master of none. Silica microspheres do feature excellent optical cavities and mechanical oscillators, but our configuration does not hold any records for the relevant parameters. The microspheres are made from high purity silica, which produces an atomically smooth surface and features extremely small optical losses from absorption or scattering. More specifically, Q_c and Q_m for a 30 μm silica microsphere are typically on the order of 10^8 and 10^4 respectively, with ω_c and ω_m being on the order of 10^{14} Hz and 10^8 Hz respectively. Thus, these parameters in a microsphere are sufficient to allow the experiments to be performed, while the overall simplicity of the system makes it a good system for proof of principle experiments.

3.2. Fabricating Silica Microspheres

A CO_2 laser was used to fabricate silica microspheres out of single-mode optical fiber[1]. A diagram of the sphere fabrication apparatus is shown in Fig. 3.7. The final product of this fabrication process is a sphere of silica, approximately 30 μm in diameter, attached to a stem that tapers to a thickness of 5 μm. The first step in the fabrication process is to strip the jacket from a small length of fiber and mount it vertically in a fiber chuck, with the loose end of the fiber facing downwards. A small weight (a washer for 1/4" machine screws) was then taped to the loose end of the fiber.

The CO_2 laser was focused near the fiber and then brought just close enough to the fiber to burn away the cladding. Next, the fiber was rotated about its vertical axis by 90 degrees and this process repeated for a total of four times from each angle. Considerable care was taken when burning the cladding so as to not leave behind soot. Melting the fiber core while burning away the cladding can result in burying

41
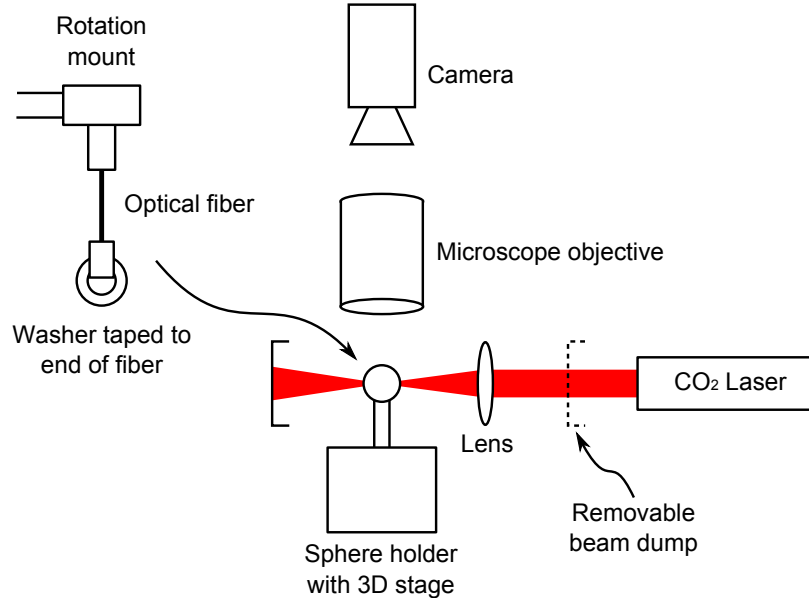
FIGURE 3.7. Top view of the apparatus for sphere fabrication, with a close-up side view of the sample mount. The sphere is made out of a piece of optical fiber, which hangs vertically and is tensioned by the weight of a small washer. A CO_2 laser is used to sculpt the sphere. The system is imaged 90° from the axis of the laser.

soot in the fiber core, and subsequently the final product, leading to poor optical quality factors.

Once the cladding has been successfully removed, the remaining silica fiber core can be sculpted into a microsphere. First, the core is gently heated by bringing the focused laser progressively closer, which melts the fiber and allows the weight to stretch the fiber into a thin strand. The diameter of the strand should taper down to the desired stem thickness. Next, the laser was used to sever the strand at a lower point, allowing the weighted end of the fiber to drop away. The amount of material left after severing the strand will determine the size of the sphere. The remaining material was gently fed into the focused laser. As the material melts, its surface tension pulls it into a spherical shape. Some degree of practice is required during the aforementioned step in order to produce a final product with the desired dimensions, given that a considerable amount of material is lost while it is being fed into the

focused laser. It can be helpful to heat this material from some distance up the side, rather than directly from the bottom, so as to cause a larger sphere to accumulate without losing quite as much material. If this is done, however, it is important to make sure that the final stoke of melting of the sphere is done from below rather than from the side, in order for the final product to be as symmetrical as possible.

The goal of this procedure is to produce a sphere of the desired diameter while keeping the stem as short and narrow as possible. The diameter of the stem at the point where it meets the sphere is one of the primary limiting factors for the mechanical quality factor, so it is best to keep the stem as thin as possible. The length of the stem is also important because a long stem is extremely fragile. If the stem is too long, the stem will break while attempting to transfer the sample into the experimental chamber. Keeping the sample in a vertical position while moving it can help mitigate this problem, but it is still important to keep the stem short. Our stems are typically 5 μm thick at the point where they connect to the sphere, and approximately 200 μm long.

If a tapered optical fiber is used to couple light into the microsphere then the sphere is complete at this point. If, however, it is desired to preform free-space optical excitation, then it is now necessary to deform the sphere[48]. We have tried several methods to accomplish this. One method is to hit the sphere from the side with a quick pulse of the CO_2 laser. Another is to make two separate spheres, and then carefully melt them together, heating them gently enough that the final product has not yet become perfectly spherical. The former method is significantly less time consuming, but we have found that the latter method yields better results. The necessary deformity is beyond the resolution of the viewing screen of the fabrication apparatus. In light of this, it's best to start with a deformity that is higher than

desired, test the sphere in the experimental chamber, and then transfer it back to the fabrication table to reduce the deformation incrementally until reaching the desired deformation. A deformation that is too high will have low quality optical and mechanical modes. A deformation that is too low will have poor optical coupling.

3.3. Tapered Optical Fibers

For some of the experiments presented here, light was coupled to the microsphere through the evanescent field of a tapered optical fiber[49–51]. This approach has several advantages. One significant advantage is that a perfectly round microsphere can be used, as opposed to the free-space method which requires deformed microspheres.

To fabricate the tapered fibers, optical fiber was heated with a hydrogen torch and pulled until the desired thickness was achieved. Once the taper has been fabricated, its tension within its mount needs to be properly adjusted. The ends of the tapered fiber were clamped into a removable holding device and transferred to a separate tensioning station. The removable holding device also contains a mechanism for adjusting the fiber tension. The tensioning station consists of a 3-axis stand for the tapered fiber holder, a microscope imaging system, and a dispensable microsphere similar to the experimental samples. The microsphere was brought close enough to the tapered fiber that the two would stick together through electrostatic forces. The microsphere was then pulled away until the two separated. The amount of movement required to pull the sphere away from the fiber was used to gauge the tension of the fiber. A sufficient amount of tension allows the sphere to be positioned close to the fiber without the two getting stuck together.

Once the desired tension has been achieved, the ends of the fiber are glued into a separate, smaller fiber holder using UV cure epoxy. At this point, the fiber is ready for use.

3.4. Experimental Chambers

Two different experimental chambers were used for the work presented here. One chamber was used for free-space coupling, and the other for fiber coupling. The purpose of both chambers was to provide a controlled, clean environment for the samples, and to isolate the samples from both air currents and vibrations in the room.

For isolation from vibrations, both chambers were laid upon vibration damping foam. Additionally, the chambers were bolted to the optical table, with a vibration damping foam washer accompanying each bolt. Once a sample was in position, the chambers were purged with nitrogen or helium. It is important to use a gas source that is free from moisture, as absorption of water vapor can degrade the optical quality of silica microspheres significantly in less than an hour.

Both chambers used Attocube micropositioners to achieve high precision movement control. Attocube positioners are piezo-electric based devices that provide the precision of piezo technology without the limited range of motion that is typically associated with the use of piezo-electrics. This is accomplished by allowing the control mechanism to slip when the piezo moves quickly and to stick when the piezo moves slowly. By applying a saw-tooth waveform to the piezo, the control mechanism essentially shuffles the sample in one direction. This action can be compared to sitting in a cardboard box on a linoleum floor and scooting the box across the floor by moving one's body weight quickly in one direction and slowly in the other.

The shuffling movement is used for course movement, while a constant voltage can be applied to the piezo crystal to achieve fine movement control. In addition to the Attocube positioners, both chambers also included screw-threaded actuators for coarse movement control.

The free-space chamber was a rectangular enclosure, which is shown diagrammatically in Fig. 3.8. This chamber had two windows on opposing walls and a narrow gap in between the two windows. The attocube positioners were mounted inside the chamber between the two windows, and the microsphere sample was mounted on top of the attocube positioners so that the microsphere hung vertically between the two windows. The entire chamber was mounted on top of a three-axis stage for course control of the sample's position. A microscope objective was mounted in front of each window, with each microscope objective having its own three-axis stage. The microscope objectives focused light near the microsphere to provide input and output coupling. Additionally, there was a third window in the top of the chamber which was used for an additional CCD imaging system.

The fiber coupling chamber was a circular enclosure, with two fiber feedthroughs for the tapered optical fiber, as shown in Fig. 3.9. These feedthroughs were made by inserting the fiber through a hole drilled through a rubber cylinder and then clamping the rubber cylinder in a Swagelok tube feedthrough. As with the free-space chamber, the microsphere sample was mounted on an attocube stack to hang vertically. In this case, however, the attocube stack was then mounted on top of a mechanical three-axis stage, which was used for course positioning prior to closing the chamber. Additionally, the tapered fiber was mounted on a goniometer to allow its pitch to be adjusted. It was found that mounting the sphere on the attocubes is preferable rather than mounting the tapered fiber on attocubes, as moving the tapered fiber

46
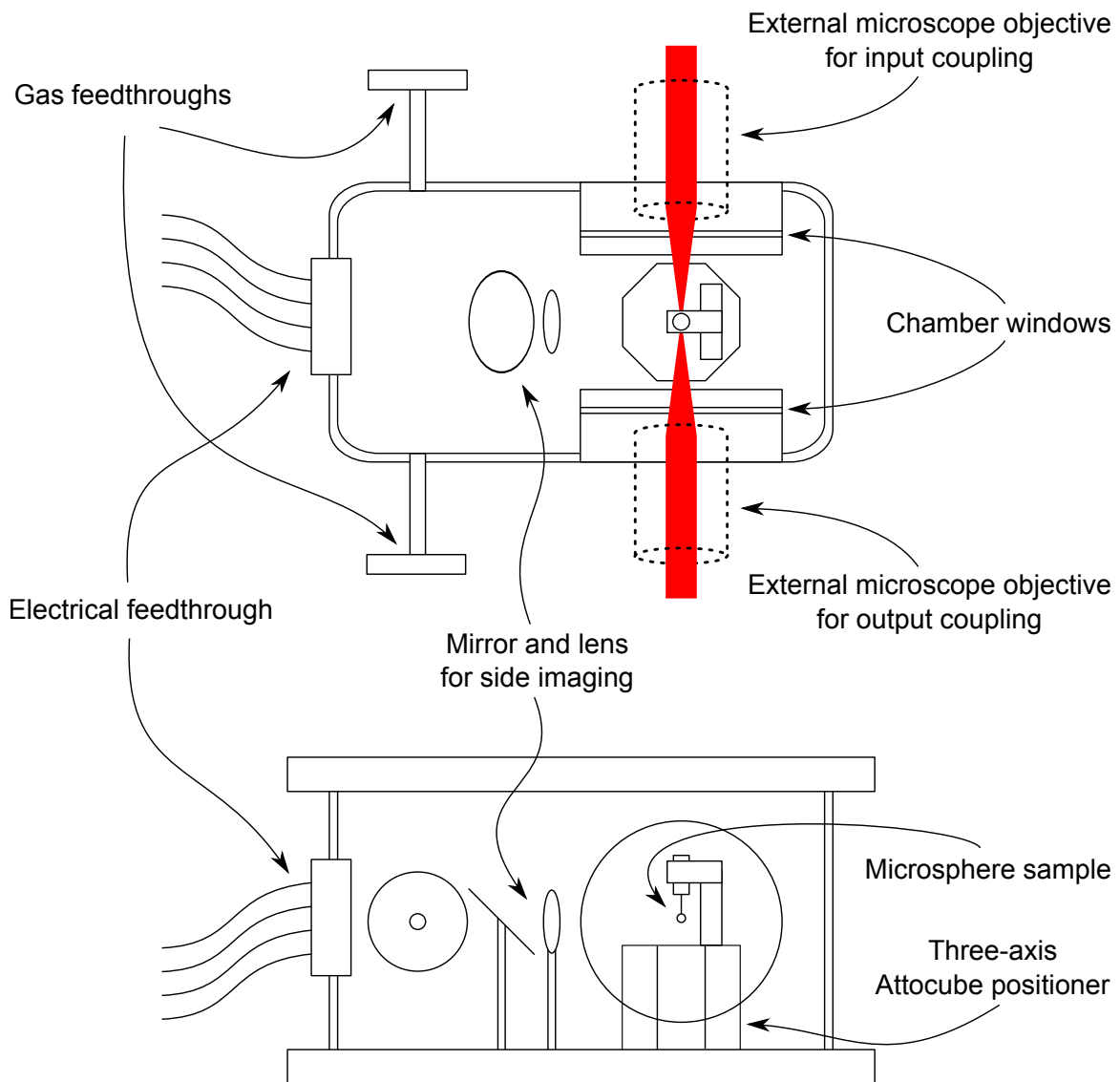
FIGURE 3.8. Experimental chamber for free-space optical coupling. Incoming and outgoing light was coupled to the microsphere sample using two microscope objectives. Both microscope objectives were mounted outside of the chamber, with each having its own three-axis manual positioning stage. Due to the short focal length of these microscope objectives it was necessary for the chamber windows to be recessed within the chamber walls, thus allowing the microscope objectives to both be positioned sufficiently close to the microsphere sample. The microsphere was mounted upon a three-axis Attocube micropositioner for precision position adjustment. A detailed diagram of the microsphere holder, which sits on top of the Attocube positioners, can be found in Fig. B.2. The entire chamber was mounted upon a three-axis manual positioning stage to allow for coarse adjustment of the microsphere's position. The three-axis stage rested on vibration damping foam.

with attocubes causes the fiber to vibrate significantly. The fiber coupling chamber also contained a CCD imaging system. For our earlier work, the entire CCD imaging system was mounted inside the chamber. Later, the chamber was modified to have a window and an externally mounted imaging system.

3.5. Detection and Laser Locking

The Pound-Drever-Hall technique was used to lock the frequency of the laser relative to the optical modes of the microsphere[52, 53]. Part of this process is to create what is commonly referred to as an "error signal". The error signal varies with frequency, is centered around the desired optical mode, and has a shape that is characterized by several other parameters. The error signal was then sent to a PID controller, which uses the error signal to determine what corrections are necessary to keep the laser frequency locked relative to the optical mode. The feedback loop is completed by sending the output of the PID to the laser to control the laser's frequency.

Understanding the function of the PID circuit is crucial to understanding the the laser locking feedback loop as a whole. Historically, the PID controller was first developed as autopilot for ocean-going vessels, and as such it is helpful to compare adjusting the laser frequency to the steering a ship. The error signal is sent to the PID and the PID essentially attempts to maintain a constant set-point for the error signal. For a ship, the error signal would vary in some way with respect to the ship's heading. In our case, the error signal varies with respect to the laser frequency. If the PID receives an input that is above or below the set-point, then the PID gives an output that tells the laser (or ship) to "steer" back towards the set-point. It is important to note that this happens regardless of the specific shape of the error signal
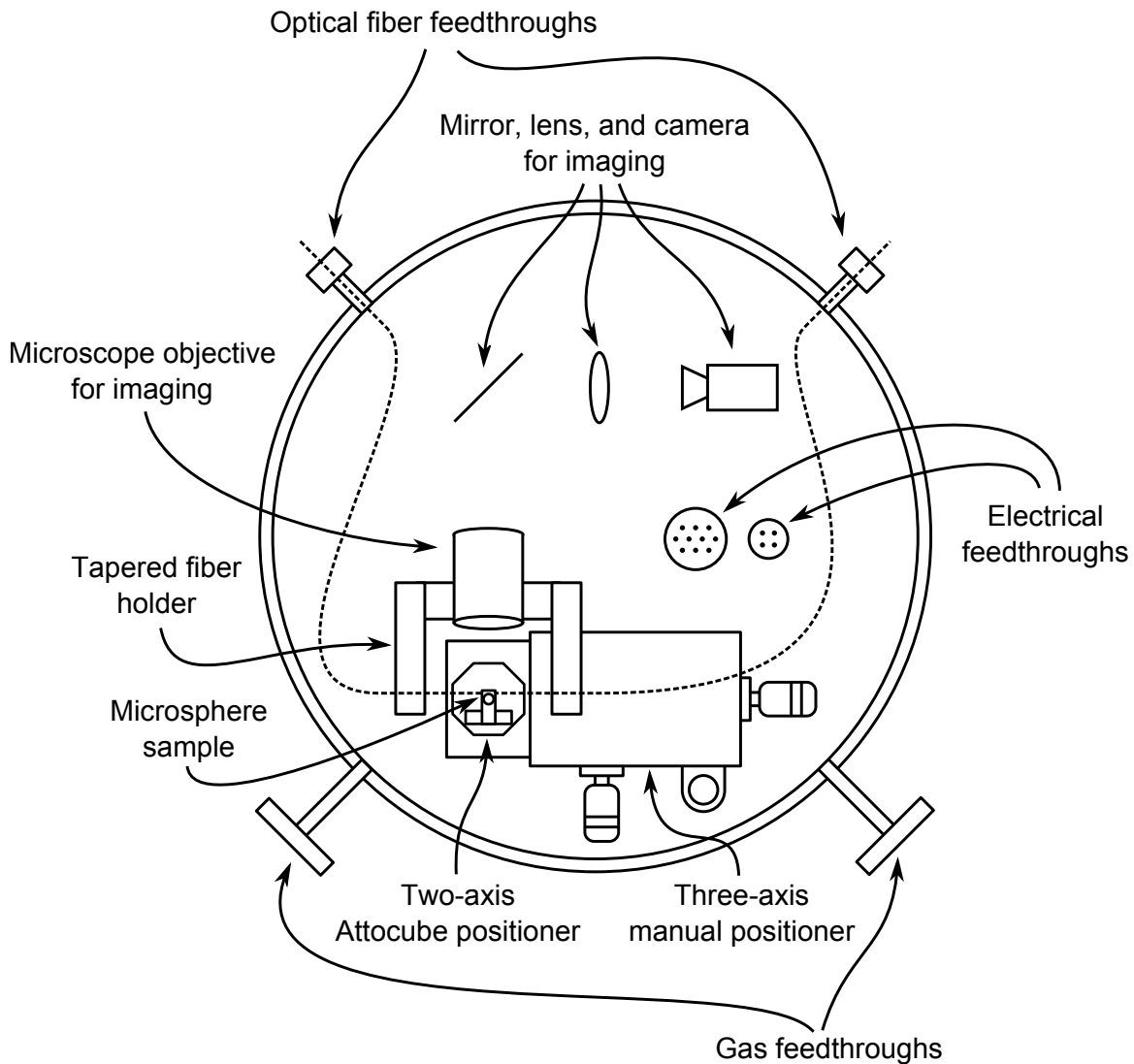
FIGURE 3.9. Experimental chamber for tapered fiber optical coupling. The tapered section of the fiber was held by a custom made forked holder that allowed the tapered fiber and microsphere sample to be correctly positioned relative to each other, while still allowing room for a microscope objective for imaging. The tapered fiber holder was mounted upon a goniometer, which allowed the tapered fiber to be tilted relative to the microsphere. A diagram of the tapered fiber holder is presented in Fig. B.1. The tapered fiber's goniometer was subsequently mounted upon a linear translation stage that moved along the axis of the fiber, thus allowing different sections of fiber to be used. The microsphere itself was mounted upon a two-axis Attocube micropositioner, which in turn was mounted upon a three-axis manual positioning stage. A diagram of the microsphere holder, which sits on top of the Attocube positioners, can be found in Fig. B.2. Only two axes of fine control were necessary, with movement along the axis of the tapered fiber not requiring high precision. The entire chamber rested on vibration damping foam.

or how the error signal varies with respect to the ship's heading or the laser frequency. That is to say, the PID is only concerned with the difference between the set-point and the current value of the error signal, and the PID has no knowledge of the shape of the error signal.

PID stands for "proportional-integral-derivative", which are the different methods that it uses to decide how to steer. The proportional component is a real-time response, meaning that if the ship is pointing too far to the left then the PID will tell the ship to steer to the right. The integral component is a cumulative time-based response that is a reflection of how much time the ship has spent pointing at the wrong heading. This means that if the ship has been pointing too far to the left for a very long time then the integral component will produce a very strong response. If the ship has been pointing too far to the left for only a short period of time then the integral response will be weak. The derivative component, however, looks at how quickly the ship's heading is changing. If the ship gets hit by a wave and suddenly veers off to the left, then there will be a large response from the derivative component. Another way to look at these components is to say that the proportional component looks at the present error signal, the integral component keeps track of the past error signal, and the derivative component tries to predict the future error signal.

The choice between different locking methods is generally a choice between different methods for creating the error signal and the subsequent shape of the error signal. Different methods will effect different shapes, and the shape of the error signal has a large influence on the behavior of the laser lock. The most straightforward method is to simply use some type of spectral peak or dip (such as an optical resonance) as the error signal itself. The PID set-point is then chosen to be an intermediate value between the background level and the top of the peak. The PID
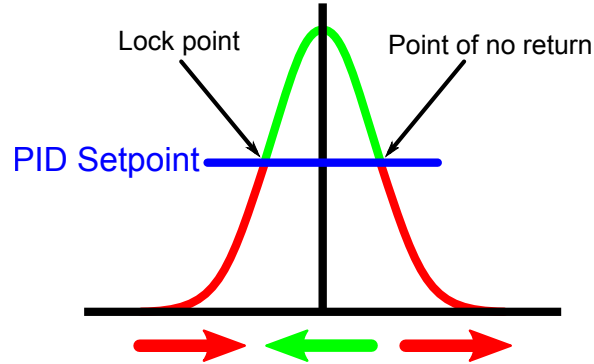
FIGURE 3.10. Illustration of side-locking. The feedback circuitry attempts to keep the optical feedback signal at a specific setpoint. If the signal deviates below the setpoint, the locking circuitry responds by adjusting the laser frequency in one direction (red arrow), while a deviation above the setpoint results in an adjustment in the opposite direction (green arrow). Note that this configuration will actively shift the laser away from the desired lock point if the frequency jumps past the point where the setpoint crosses the optical feature on the other side (labeled here as "point of no return").

then attempts to maintain that intermediate value, thus keeping the laser at the frequency that corresponds to that part of the spectral feature, as shown in Fig. 3.10. As such, this configuration is typically referred to as "side-locking".

While the side-locking approach is easy to set up, it suffers from several drawbacks. One drawback is highlighted by the name "side-locking" itself. For most applications it is preferred that the laser be locked as close as possible to the center of the spectral feature. It is possible to adjust the set-point of the side lock to get ever closer to the center of the spectral feature, but doing so reduces the stability of the lock. As shown in Fig. 3.10, if the laser's frequency deviates into the red region on the right then the feedback system actively moves away from the lock point. Shifting the set-point closer to the center of the spectral feature decreases the safety cushion between the set-point and this region, making it progressively easier for the laser to lose its lock.

While the aforementioned drawbacks can often be overcome with some ingenuity, there is yet another problem with side-locking that is not so easily overcome. Fluctuations in various experimental parameters, such as fluctuations in the amplitude of the laser's power output, will cause the relative size of the spectral peak to fluctuate. As this happens, the laser frequency corresponding to the set-point changes. Thus, side locking causes amplitude fluctuations of any kind to manifest themselves as fluctuations in the lock frequency. This can be a substantial issue for many experiments.

A more refined alternative is to dither the frequency of the laser, thus allowing the frequency to be locked at the center of the optical feature. This is possible by comparing the relative amplitude between the dithered laser frequency and the optical output of the system, as shown in Fig. 3.11. This essentially produces a measurement of the slope of the optical output. With the slope being measured, it is now possible to send that measurement to the PID. The laser can now be locked to the point where the slope is zero, which is the center of the optical feature.

The Pound-Drever-Hall method provides a rather similar method for center-locking. This is done by using an electro-optic modulator (EOM) to modulate the laser light prior to the experimental sample. Rather than modulating the laser's frequency, we are instead modulating the phase. The optical signal after the sample is sent to a lock-in amplifier, which has the effect of measuring the relative phase between the laser's modulation and the phase of the subsequently modulated optical signal. This arrangement produces an error signal from the output of the lock-in amplifier that has the shape shown in Fig. 3.12. An important trait to notice about this error signal is that it crosses zero at the center of the optical feature. This means that with a set-point of zero, the laser can be center locked and the locking
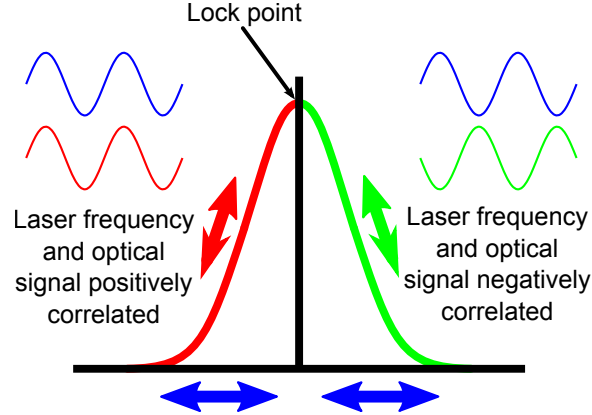
FIGURE 3.11. Center locking by laser frequency dithering. Prior to being sent to the experimental sample, the laser light is frequency modulated. The feedback circuitry determines the laser's position by comparing the relative amplitude between the laser and the optical signal. A positive slope produces a positive correlation between the laser frequency and the optical signal, while a negative slope produces a negative correlation. A PID setpoint of zero will lock the laser at the location where the slope is zero.

frequency is unaffected by amplitude fluctuations. Also, the fact that the setpoint is at a zero crossing means that the locking frequency is unaffected by laser amplitude fluctuations.

Another useful aspect of the Pound-Drever-Hall error signal is that it has additional zero crossings corresponding to the side-bands of the EOM. These side-band zero crossings have the opposite slope from the central zero crossing. By changing the sign of the PID circuit, it becomes possible to lock the laser at a set amount away from the optical feature, with the amount of detuning being determined by the EOM frequency. This can be particularly useful when optical bistability distorts the optical feature when at resonance.

3.6. Pulsing the Light and Time Gated Heterodyne Detection

The experiments presented in this work involve measurements in the time domain. As such, it is necessary to pulse the various incoming optical beams and

53
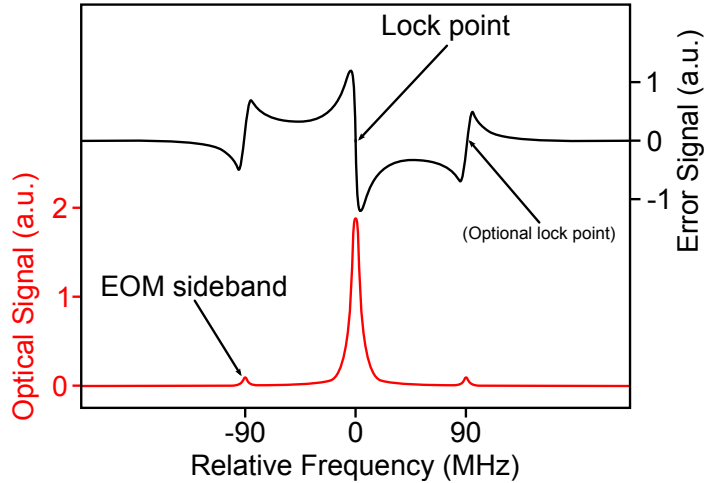
FIGURE 3.12. Sketch of the error signal produced by the Pound-Drever-Hall method. Note the zero crossing at both the center of the optical feature and at the EOM sidebands.

to have a time-gated detection method. This also necessitates special considerations concerning the laser locking procedure.

The optical pulses were, for the most part, produced by pulsing the electronic driving signals for acousto-optic modulators (AOMs) and using the first-order diffracted light beam as the pulsed beam. Pulsing of the electronic driving signals was achieved by using programmable arbitrary-waveform generators (AFGs) to amplitude modulate the RF sources for the AOMs. The AFGs were synchronized by using one AFG as the trigger source to trigger the other AFGs and the other time-gated equipment. The specific waveforms for each AFG were supplied by a desktop computer. The computer used Labview programs that were written to control these experiments.

Outgoing light from the microsphere was detected using time-gated heterodyne detection. The optical beam of interest (i.e. the signal beam for the light storage experiments or the probe beam for the OMIT and dark mode experiments) is shifted from the driving optical beam by an amount equal to the frequency of the chosen

mechanical mode of the microsphere. As such, this beam can be detected via heterodyne detection by virtue of its beating against the unshifted pump beam. Fortunately, the geometry of these experiments (both with free-space and tapered-fiber) is such that these beams are already collinear. By using a photodetector with an appropriate frequency response and sending its electrical output to a spectrum analyzer (SA), it is possible to detect the optical signal by looking for this beating. Furthermore, this detection can be performed in the time domain by using a time-gated spectrum analyzer. This feature of the SA is able to examine an RF signal in a specific time window by electronically masking its input signal.

It is also necessary to make provisions to allow the laser locking equipment to function properly when the locking beams are pulsed. The locking optical beam is pulsed prior to the microsphere such that it is only present when it will not interfere with experimental measurements. After leaving the microsphere, the portion of outgoing light that is sent to the locking equipment is also pulsed with an AOM so that changing experimental parameters will not have an impact on the lock. Additionally, the lock-in amplifier is configured such that its time-constant is longer than the repetition period of the experiment cycle. Typically a time constant of 3 ms was used. This was done so that the lock would not be affected by the gaps in time where the locking optical beam was shuttered off during experimental measurements.

3.7. Bringing It All Together

Details for adapting the experimental apparatus for each specific experiment are described in the chapters for each specific experiment. Before concluding this chapter, however, we shall touch upon the overall arrangement of the system. Figures 3.13 and 3.14 show diagrams of the experimental apparatus for the light storage experiments.
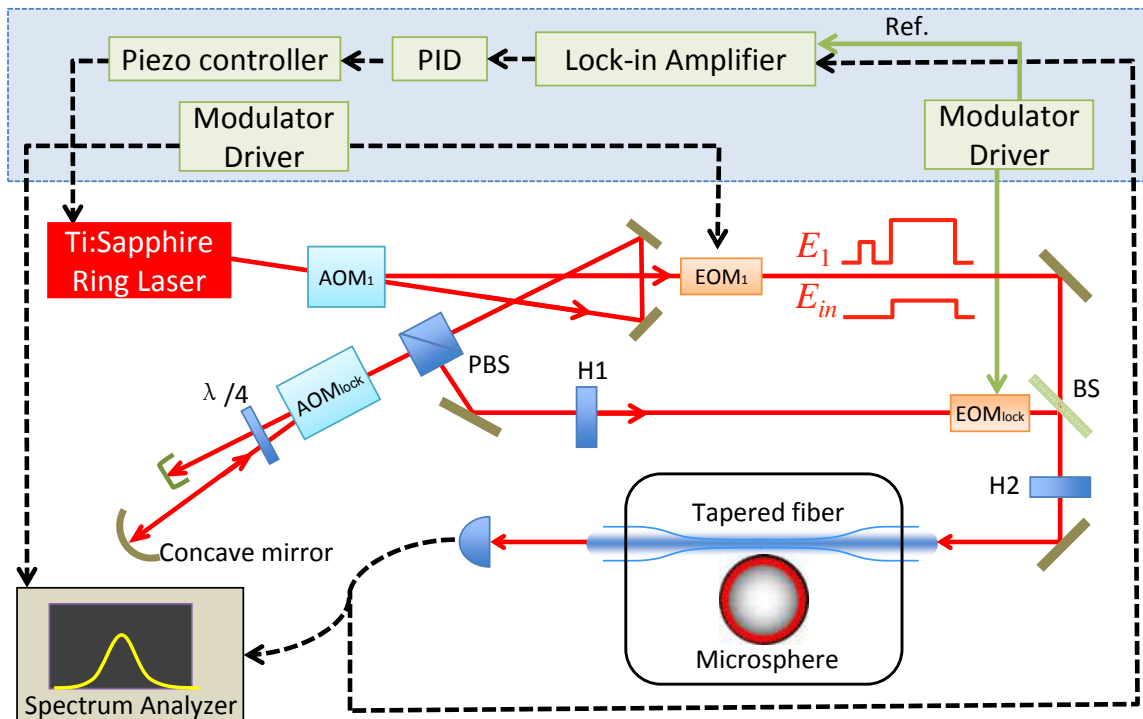
FIGURE 3.13. Optical layout for light storage experiments. Modulators are used to create the optical pulses. In this particular example, light is coupled to the microsphere using a tapered optical fiber.
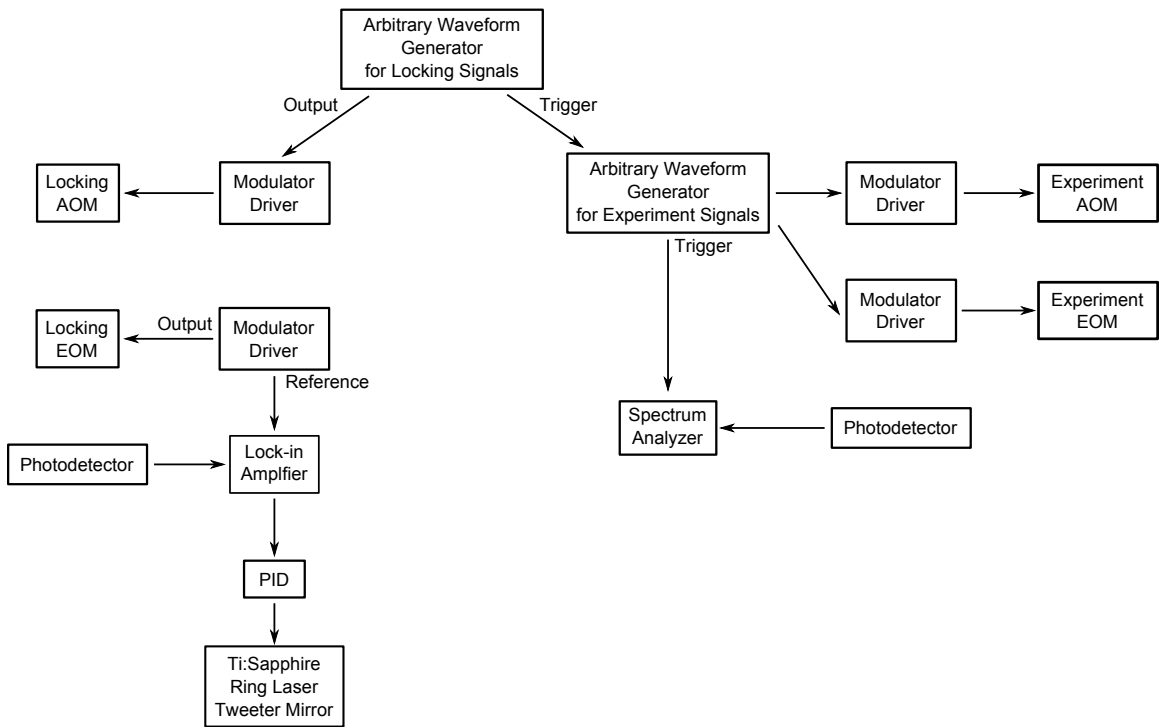
FIGURE 3.14. Electronics layout for light storage experiments. Arbitrary waveform generators are used to control the amplitudes of the various optical pulses. These signals then amplitude modulate the drivers for the individual modulators. The lock-in amplifier and the spectrum analyzer each have their own separate photodetector, which reduces electronic cross-talk between the lock-in amplifier and the spectrum analyzer.

The configuration for the other experiments is similar to the configuration for light storage, so this arrangement provides a good example.

The various optical pulses were derived from a Coherent 899 Ti:Sapphire ring laser. This laser light then passes through a sequence of acousto-optic modulators (AOMs) and electro-optic modulators (EOMs) in order to generate the necessary optical pulses. The specific frequencies and timings required for these pulses are particular for each specific experiment, so the exact configuration of these modulators is covered in more detail in each relevant chapter. Generally speaking, pulses necessary for locking are alternated with pulses for taking experimental data. This light is then coupled to the microsphere sample, either by free-space coupling or through the use of a tapered optical fiber. Outgoing light is collected with high speed photodetectors. Locking and data collection each had a dedicated photodetector in order to avoid contamination of either electrical signal. The electrical signals from these photodetectors were sent to the lock-in amplifier and the time-gated spectrum analyzer. The lock-in amplifier provides the error signal for the locking circuitry, while the spectrum analyzer performs the data collection.

CHAPTER IV

TRANSIENT OPTOMECHANICALLY INDUCED TRANSPARENCY

"A lack of transparency results in distrust and a deep sense of insecurity."

– Dalai Lama

4.1. Motivation

It has been predicted[41, 54] and experimentally demonstrated[37, 55–57] that optomechanical systems exhibit a phenomenon analogous to electromagnetically induced transparency (EIT). In the context of optomechanical light storage, it is useful to examine optomechanically induced transparency (OMIT) in more detail, especially in the transient domain, in order to compare optomechanical light storage to light storage using EIT. OMIT plays a central role in optomechanical light storage and optomechanical dark modes, but these processes take place in the transient domain. Much of the previous work involving OMIT focuses only on its steady state behavior. It is thus desirable to extend the scope of OMIT research to encompass the transient domain.

EIT is a process by which the opacity of an atomic system, with regards to a specific frequency of light, is altered by the presence of light of another frequency [58–60]. The optical beam whose opacity is altered is sometimes referred to as the "probe", and the other referred to as the "pump" (sometimes the "pump" beam is instead referred to as the "control" beam). In order to facilitate EIT, an atomic system must have three separate atomic states such that one transition is dipole forbidden and the other two dipole allowed. The pump and probe are tuned such that each corresponds with one of the dipole allowed transitions. There are several different configurations
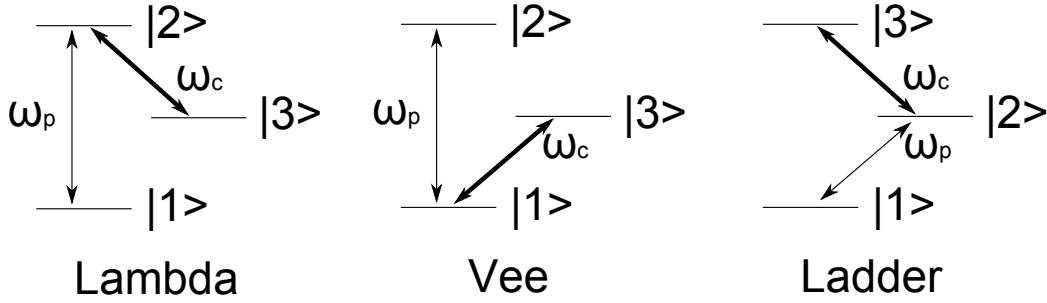
FIGURE 4.1. Energy level diagrams for EIT.

that fit this description, which are shown in Fig 4.1. The different configurations are typically named based on which transition is dipole forbidden.

The optomechanical analog to EIT is OMIT. In a similar manner, OMIT also uses a pump beam to render an optomechanical system transparent to a probe beam. With OMIT, the probe beam is at resonance with an optical mode, while the pump beam is one mechanical frequency, ω_m, below that optical mode. The pump beam excites an intracavity optical field via the anti-Stokes process. In the absence of the pump beam, the probe beam would interact with the optical mode, displaying a transmission dip when at resonance. In presence of the pump beam, however, the intracavity optical field generated by the pump beam destructively interferes with that of the probe beam, preventing the probe from exciting the optical mode. Thus the pump beam causes the system to be transparent with respect to the probe.

It should also be noted that the overall width of the transmission dip of the probe field is determined by the optical quality factor, while the width of the transparency window is governed by the mechanical quality factor. This means that the observed OMIT effect is a narrow transparency window within the broader optical mode. The width and depth of the peak can be related to the optomechanical cooperativity, $C = (2g)^2 / \Gamma_m \kappa$, as was presented in Eqs. 2.44 and 2.45 and derived in Chapter II.

For convenience, we restate Eqs. 2.44 and 2.45 here:

$$\gamma_{OMIT} = \Gamma_m(1 + C) \tag{4.1}$$

$$|t_p'(\Delta = 0)|^2 = \left(\frac{C}{1+C}\right)^2 \tag{4.2}$$

Additionally, the spectral position of the transparency window is dictated by the spectral separation between the pump and probe. If the pump-probe separation is exactly ω_m then the transparency window will be at the center of the optical mode.

Our work with OMIT focuses specifically on its transient behavior[61]. This is of particular interest because of the similarities between optomechanical light storage and light storage through EIT. Prior to the work presented here, much of the research involving OMIT has focused on its steady state behavior. Many of the processes that involve OMIT, however, take place under transient conditions. Such processes include optomechanical light storage and optomechanical dark modes. In this chapter, we examine the transient behavior of OMIT, by means of time-gated detection and by pulsing the incident light. This allows us to directly observe the evolution of the system as it approaches its steady state.

4.2. Experimental Details

A general description of the experimental techniques is presented in Chapter III. Figure 4.2 shows a diagram of the apparatus, as configured specifically for the work in this chapter. The OMIT experiments were performed using the tapered fiber coupling method described in Chapter III. These experiments were performed with the (1,0) radial-breathing mechanical mode. The following details were necessary to tailor the apparatus to OMIT in particular.
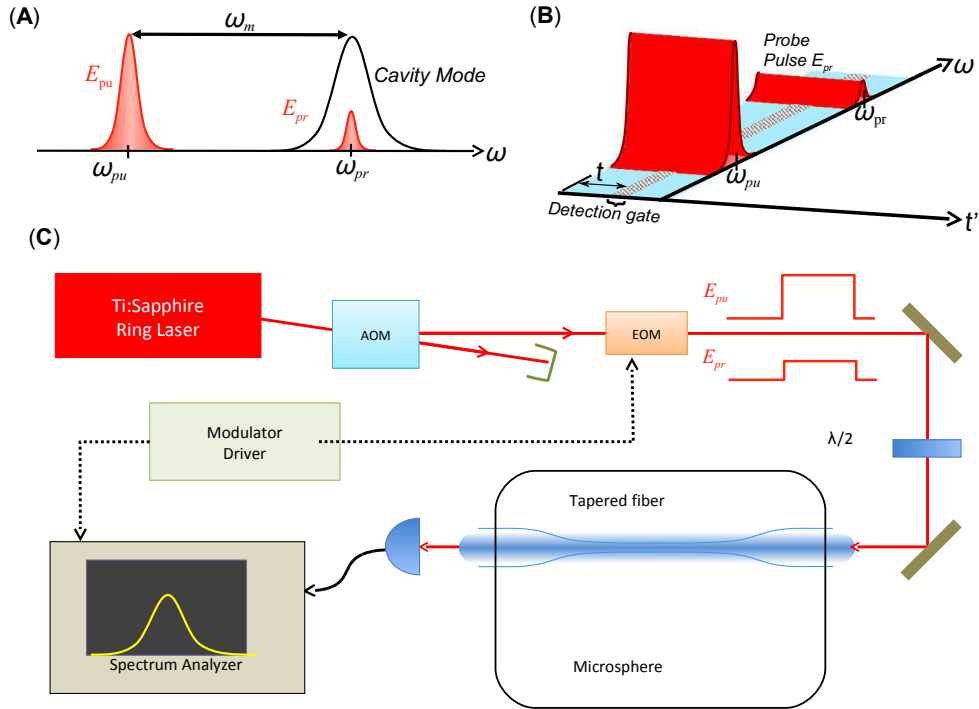
FIGURE 4.2. (a) Spectral position of the pump (E_{pu}) and probe (E_{pr}) pulses, relative to the optical cavity mode. The probe pulse is at resonance with the cavity mode, while the pump pulse is separated by a distance of one mechanical frequency, ω_m. (b) Diagram of temporal positioning. The pump and probe pulse arrive simultaneously while the position of the detection gate is adjustable. The duration of the optical pulses is 8 μs, and the detection gate duration is 0.5 μs. (c) Experimental layout for OMIT experiments. The AOM is used to gate both experimental pulses. The first order, blue sideband of the EOM serves as the probe pulse while the zeroth order light serves as the pump. These modulators also create the necessary signal to lock the laser.

Unlike the light storage and dark mode experiments, which will be presented in subsequent chapters, the optical pulses for the OMIT experiments arrive simultaneously. These pulses then last long enough for the system to reach its steady state. The spectrum analyzer detection gate is adjusted iteratively to measure the temporal profile of the heterodyne signal, with the profile beginning at the arrival of the optical pulses. This is essentially the equivalent to performing the light storage experiments, but examining only the behavior at the arrival of the writing pulse. In the case of OMIT, however, we refer to the on-resonance light as the "probe" pulse, and the Stokes shifted light as the "pump" (as opposed to the names "signal" and "writing" which we will introduce when discussing light storage).

These two pulses are produced by an acousto-optic modulator (AOM) and an electro-optic modulator (EOM). The AOM is used to pulse the laser by using its first order diffracted beam. Downstream from the AOM, the EOM is used to split this pulse into the pump and probe pulses, with the zeroth being the pump and the blue shifted first order sideband being the probe. These modulators also provide the necessary signal to lock the laser. Also, it should be noted that the time resolution of the temporal profiles is determined by the spectrum analyzer's resolution bandwidth of 3 MHz and its detection gate duration of 0.5 μs.

4.3. Results

The following results were obtained using a silica microsphere with a diameter of $\sim$30 μm and with $(\omega_m, \Gamma_m, \kappa)/2\pi = (160.9, 0.096, 20)$ MHz. The peak powers of the pump pulse and the probe pulse are 1.6 mW and 0.01 mW, respectively.

Figure 4.3 shows the optical emission power as a function of time. This is with time $= 0$ being the time that both the pump and probe are turned on and with the
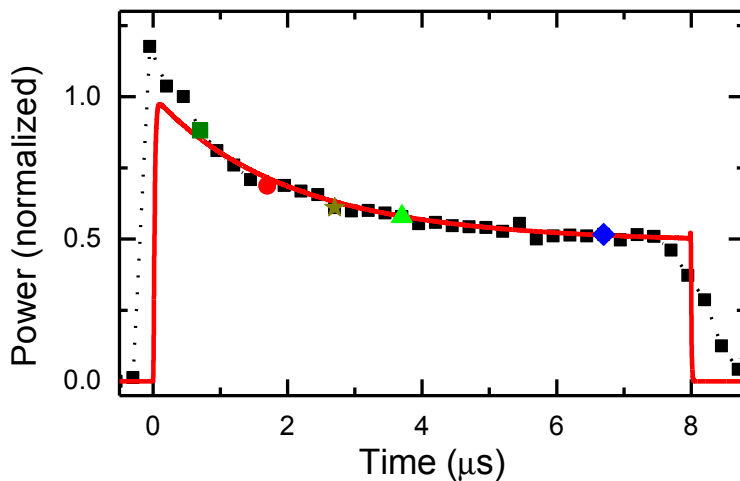
FIGURE 4.3. Optical emission power as a function of the delay of the detection gate. The probe pulse is at resonance with the optical mode and $\Delta = -\omega_m$.

probe being at resonance with the WGM. This emission power decreases over time while approaching its steady state value. At time $= 8$ μs, both pulses are turned off. This same measurement was performed while instead sweeping the frequency of the probe beam across the WGM resonance at different time points to produce Fig. 4.4. That is to say, this figure shows the transparency windows as a function of the pump-probe separation, Ω. The dip at $\Omega = \omega_m$ is the transparency induced by the presence of the pump field. It should be noted that the WGM emission powers shown in these two figures are the result of the probe being absorbed and emitted by the microsphere. Hence, a decrease in the power shown in these figures is indicative of an increase in the transmission of the probe beam.

Also note that the spectral linewidth of the transparency dip becomes narrower as the system approaches steady state. This is shown in Fig. 4.5, which plots the linewidth as a function of time.
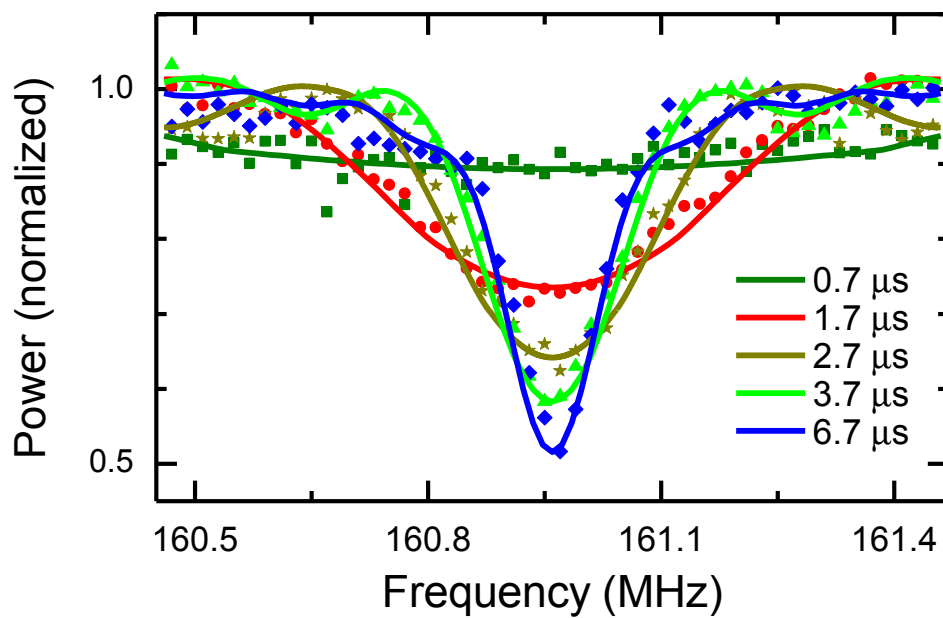
FIGURE 4.4. OMIT spectra at various points in time, showing the transparency window as a dip in the emission. These spectra were obtained by measuring the emission power while sweeping the frequency of the probe across the WGM resonance, with each plot showing a different detection gate delay. Colors and symbols correspond to specific data points shown in Fig.4.3.
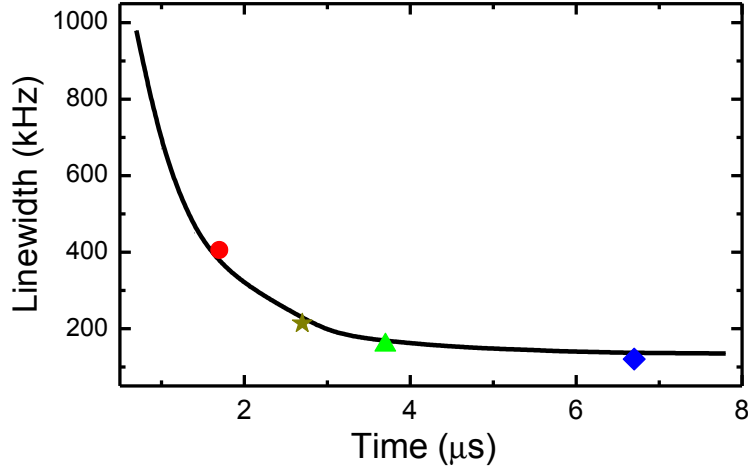
FIGURE 4.5. Spectral linewidths of the features shown in Fig. 4.4, shown as a function of detection gate delay.

The optomechanical coupling rate is related to the strength of the pump field. This is relevant for Fig. 4.6, which shows the transient OMIT behavior for several different pump strengths. Figure 4.6a is similar to Fig. 4.3, but now with various pump strengths. Each plot in Fig. 4.6a corresponds to a plot in Fig. 4.6b, which shows the OMIT dip, obtained by measuring the optical emission from the WGM at 6.7 μs, while sweeping the probe frequency across the optical resonance.

The optomechanical coupling rate can also be characterized by the system's optomechanical cooperativity, which is a dimensionless parameter given by $C = (2g)^2/\kappa\Gamma_m$. In Fig. 4.7, both the WGM emission power and spectral linewidths from Fig. 4.6b are plotted as a function of the optomechanical cooperativity.
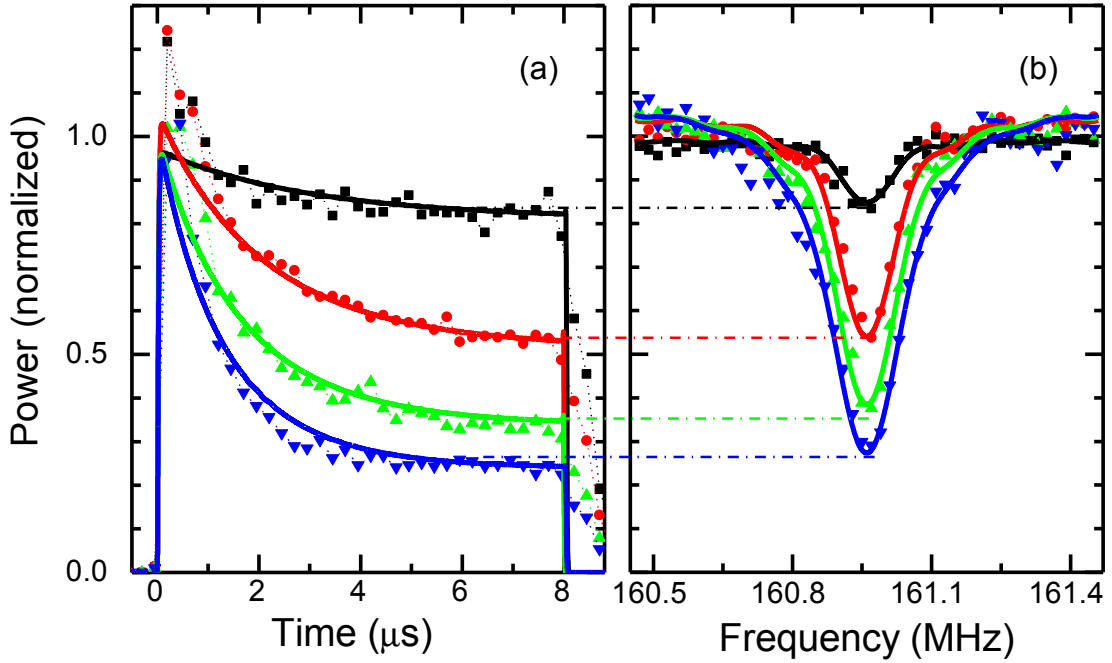
FIGURE 4.6. (a) Optical emission power as a function of the delay of the detection gate, with four different pump powers. From top to bottom, the incident pump powers are 0.4, 1.6, 2.9, and 4.8 mW. These correspond to $g/2\pi = 0.2$, 0.45, 0.58, and 0.7 MHz, respectively. As with Fig. 4.3, the probe pulse is at resonance with the optical mode and $\Delta = -\omega_m$. (b) Corresponding OMIT spectra obtained by sweeping the frequency of the probe across the WGM resonance. Each plot corresponds to a power shown in the figure to the left. These measurements were performed with a gate delay of 6.7 μs. For both figures, solid lines indicate theoretical predictions.
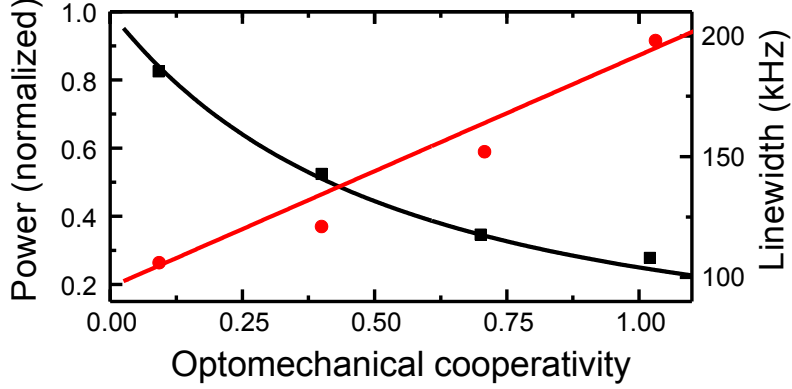
FIGURE 4.7. Spectral linewidths for each power shown in Fig. 4.6, plotted as a function of optomechanical cooperativity. Solid lines indicate theoretical predictions.

4.4. Discussion

As shown in Eq. 2.28 from Chapter II, this system can be expressed as two coupled oscillators:

$$\frac{d\delta\hat{a}}{dt} = \left(i\Delta - \frac{\kappa}{2}\right)\delta\hat{a} + ig\hat{b} + \sqrt{\kappa_{ex}}\delta\hat{s}_p + \sqrt{\kappa_0}\hat{f}_{in}$$
$$\frac{d\hat{b}}{dt} = \left(-i\omega_m - \frac{\Gamma_m}{2}\right)\hat{b} + ig\delta\hat{a} + \sqrt{\Gamma_m}\hat{b}_{in}$$

(4.3)

The above assumes the pump field is fixed one mechanical frequency below the optical resonance, and that the optomechanical resonator is in the resolved sideband regime.

The steady state intracavity optical field is given by

$$A^- = \frac{\left(\frac{\Gamma_m}{2} - i(\Omega - \omega_m)\right)\sqrt{\kappa_{ex}}\bar{s}_p}{\left(\frac{\kappa}{2} - i(\Omega + \Delta)\right)\left(\frac{\Gamma_m}{2} - i(\Omega - \omega_m)\right) + g^2}.$$

(4.4)

where Ω is the spectral separation between the pump and probe fields. This equation was derived in Chapter II as Eq. 2.33. The optical transmission of the probe field, from Eq. 2.41, can be written as a function of Δ_p, which is the detuning of the probe laser from the optical cavity:

$$|t'_p|^2 = \frac{\frac{(2g)^4}{\kappa^2}}{\left(\Gamma_m + \frac{(2g)^2}{\kappa}\right)^2 + (2\Delta_p)^2} \tag{4.5}$$

Under the conditions given, the spectral linewidth of the OMIT dip is $\gamma_{OMIT} = \Gamma_m + (2g)^2/\kappa$, which can be written in terms of the optomechanical cooperativity as $\gamma_{OMIT} = \Gamma_m(1+C)$. The normalized depth of the OMIT dip is given by $C^2/(1+C)^2$.

The theoretical plots shown as solid lines in Figs. 4.3, 4.4, 4.5, and 4.6 were obtained by numerically solving Eq. 4.3. The necessary values for κ and Γ_m were measured through independent experiments. The theoretical plots in Fig. 4.7 are given by the steady state equations involving the cooperativity. It should be noted that there is some distortion in the experimental results at the leading and trailing edges of the pulse. This is due to the duration of the detection gate of the time-gated spectrum analyzer, which is the limiting factor in the time resolution of the experiment and essentially smooths sudden changes. This smoothing is somewhat similar to what one might expect from a boxcar averaging method. In light of this, considerable effort was put forth to reduce the duration of the detection gate as much as possible. Aside from the aforementioned distortion, the theoretical plots show good agreement with the experimental results.

The characteristic time scale for the mechanical excitation of this system is predicted to be $[(1 + C)\Gamma_m]^{-1}$, with a damping rate of $C\Gamma_m$ being the damping rate associated just the optomechanical coupling[39, 40]. This agrees with our

experimental observations. Just after the arrival of the pulse, the optical emission power and the linewidth of the OMIT dip are dictated entirely by the small, preceding duration of the pulse. As time progresses, the dynamics of the mechanical excitation become increasingly involved. This is evident in Fig. 4.3, as the emission power monotonically approaches its steady state value. It is also expected that the evolution of the linewidth of the OMIT dip should follow the same characteristic time scale. This appears to be true, as evidenced by the results shown in Fig. 4.5.

For Figs. 4.3 and 4.4, the cooperativity was estimated to be $C = 0.4$. Increasing the cooperativity should increase the rate at which the system approaches its steady state. The cooperativity can be changed by adjusting the pump power, which is what was done in Fig. 4.6. To verify that all four plots do indeed reach steady state by the end of the pulse, Fig. 4.7 plots the values taken at 6.7 μs for the width and depth of the OMIT dip, and compares those with the calculated steady state values for each cooperativity. Evidently, the steady state is reached by this time, even for the lowest cooperativity tested.

4.5. Conclusion

This chapter examines the OMIT process in the time domain. This was facilitated by our experimental apparatus, which allows time-gated detection and pulsed optical excitation of a silica microsphere. Our experiments were able to observe the approach of the OMIT process to its steady state, with several different cooperativity values. These studies suggest that the characteristic time scale for the OMIT process is $[(1+C)\Gamma_m]^{-1}$, with a damping rate of $C\Gamma_m$, both of which are limited by the mechanical decay lifetime of the optomechanical system. It is anticipated that

this should be the characteristic time scale for other OMIT related processes. One such process, optomechanical light storage, is the subject of the next chapter.

CHAPTER V

OPTOMECHANICAL LIGHT STORAGE

"The good thing about SUVs is they have storage."

– P. J. O'Rourke

5.1. Motivation

In the modern world, fiber optics have become one of the most widely used methods for delivering information. Given that the fields of quantum networking and quantum computing both rely heavily on optical signals, the rapid development of these fields will necessitate new techniques for dealing with light. Of particular concern for us is the ability to store an optical signal, both for buffering an incoming signal in a network or for serving as memory in a quantum computer[62, 63]. In traditional digital communications, a fiber optic signal is stored by reading the optical data and storing it as electronic data. This approach is insufficient for quantum mechanical applications, as this process would destroy the quantum state.

The most straightforward approach to solving this problem would be to store the light itself in an optical resonator, such as a Fabry-Pérot cavity, thus preserving the light's quantum state. This topic has been pursued to some extent but has proven to have considerable drawbacks. One significant drawback is that the storage lifetime of such an approach is determined by the optical decay lifetime of the optical resonator, which is typically on the order of 100 ps[64].

Another approach that has been pursued would be to trap the light in an atomic system using electromagnetically induced transparency (EIT)[58, 59, 65, 66]. Given that our approach, which will be described momentarily, bears some similarities to

this method, a brief description may be prudent. The premise of EIT is to send two frequencies of laser light to an atomic ensemble, with each frequency chosen to correspond to a specific atomic transition. Typically the two different beams are referred to as "pump" and "probe". Since the probe beam is resonant with an atomic transition, the sample is opaque for the probe beam under normal conditions. However, by choosing appropriate atomic transitions, the pump beam can be used to make the sample transparent for the probe beam. This can be used as a storage mechanism by using the probe beam to carry the optical signal, and then trapping the signal by temporarily turning off the pump beam, which essentially stores the signal as a superposition of the atomic states. While this technique has been shown to boast storage lifetimes on the order of seconds, it suffers from the drawback that the frequency of light is inflexible and must be chosen to be resonant with specific atomic transitions. This is a significant problem if the goal is to connect to other quantum systems with other light frequency requirements.

As the experiments with EIT have shown, it is beneficial to convert the optical signal into something that is longer lived than simply light itself. While the EIT experiments store the signal in atomic states, it is also possible to convert the optical signal into a mechanical excitation within an optical fiber through the use of stimulated Brillouin scattering [67]. This approach is considerably more flexible in terms of optical frequencies, but has thus far shown a relatively short storage lifetime on the order of 4 ns.

Given this context, optomechanics offers an appealing option for storing an optical signal, which is the focus of this chapter. The work presented here is an experimental demonstration of storing an optical signal as a mechanical excitation in a silica microsphere[2, 3]. Silica microspheres were chosen for their ease of

fabrication, since the goal here was simply proof-of-principle. As with the case of the stimulated Brillouin scattering, the signal is stored as a mechanical excitation. In the case of optomechanics, however, the mechanical excitation is in a high quality-factor mechanical oscillator, which leads to a significantly longer storage lifetime. Additionally, in comparison to the EIT experiments, the light in the optical resonator of an optomechanical system can be virtually any frequency, limited only by the absorptive properties of the materials used. This means much greater flexibility in terms of optical frequency. All of this is accomplished while satisfying the requirement that the storage process preserve the quantum state of the stored signal.

In addition to the aforementioned benefits, an individual mechanical mode can interact with many different optical modes within an optomechanical system. This has the additional benefit of allowing the signal to be retrieved with an entirely different frequency of light. Thus, not only is this approach useful for storing the signal, but also for the conversion of the signal from one optical frequency to another. This opens up the possibility to connect one type of quantum system to another, despite differing wavelength requirements. Another possibility is the ability to map a signal to a wavelength that is suitable for long distance communication.

Although it is not investigated here, it is worth mentioning that an array of optomechanical resonators would allow the spatial-temporal profile of an optical pulse to be stored.

For the following experiments, the laser is locked in such a way that "writing" and "reading" laser pulses are tuned to one mechanical frequency, ω_m, below the optical resonance, with a "signal" laser pulse at resonance, as illustrated in Fig. 5.1. The writing and signal pulses arrive simultaneously, followed later by the readout pulse, which is shown in Fig. 5.2. The writing pulse converts the optical signal pulse
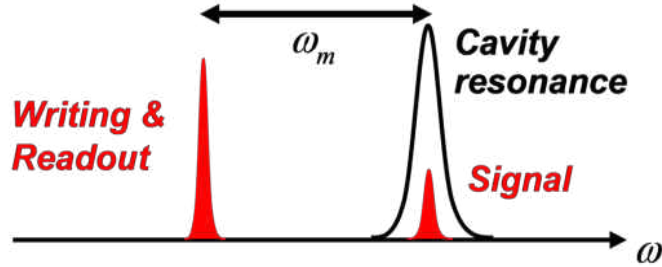
FIGURE 5.1. Spectral positions of the writing, reading, and signal pulses.
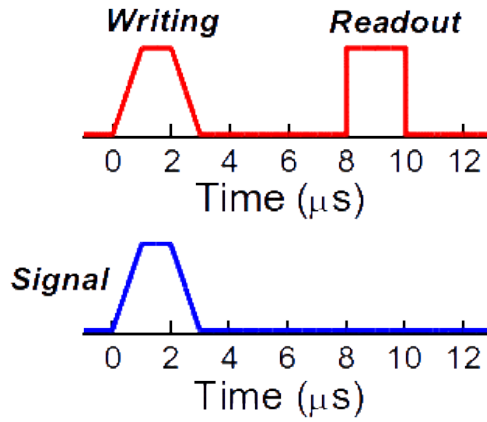
FIGURE 5.2. Typical pulse timing.

into a mechanical excitation, and the reading pulse later converts the mechanical excitation back into an optical pulse at the cavity resonance.

This is all possible because the red detuned writing and reading pulses effectively control the coupling strength between the on-resonance optical field and the mechanical mode. The specific mechanical mode affected is determined by how far the writing and reading pulses are tuned away from the optical resonance.
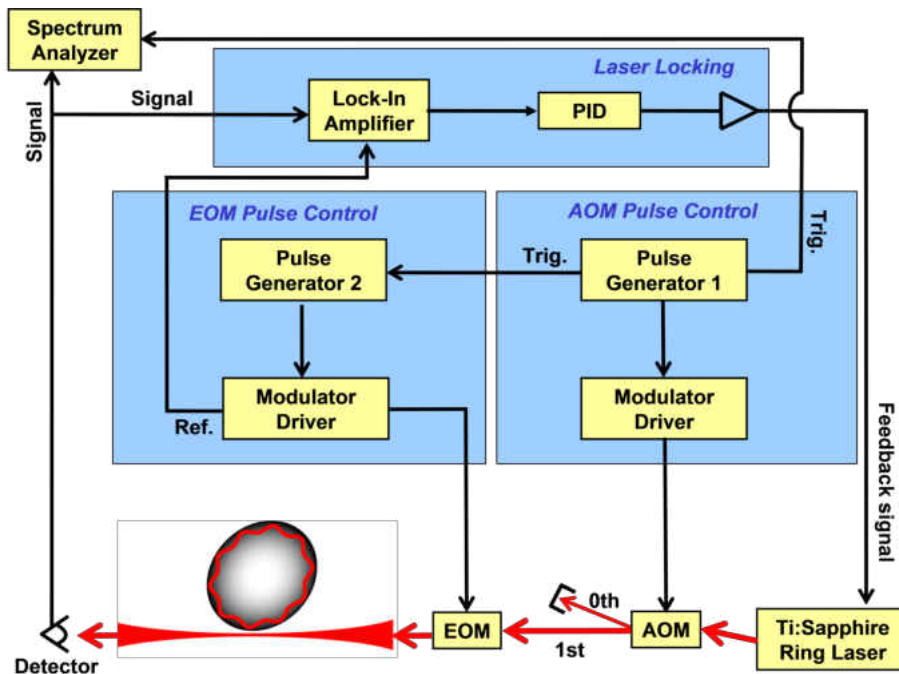
FIGURE 5.3. Experimental apparatus for our earlier single color light storage experiments[2]. Light from a CW Ti:Sapphire laser is sent through a sequence of modulators to create the necessary optical pulses, as described in the text. This light is then coupled to a silica microsphere using free-space coupling. Light from the cavity is heterodyne detected, and the signal sent to a time-gated spectrum analyser for data collection. The laser is frequency stabilized relative to the relevant optical mode using a Pound-Drever-Hall technique.

5.2. Experimental Details

The following experiments were performed using the experimental apparatus described in Section 3.7, with the specific arrangement shown in Figs. 5.3 and 5.4. For these experiments, light was coupled to the silica microsphere using the previously described tapered optical fiber method. The acousto-optic and electro-optic modulators are used to generate the pulse shapes shown in Fig. 5.2.

The retrieved optical pulse emitted by the silica microsphere is heterodyne detected and sent to the time-gated spectrum analyzer. The gate delay time of the spectrum analyzer can be changed relative to the optical pulses. Other parameters,
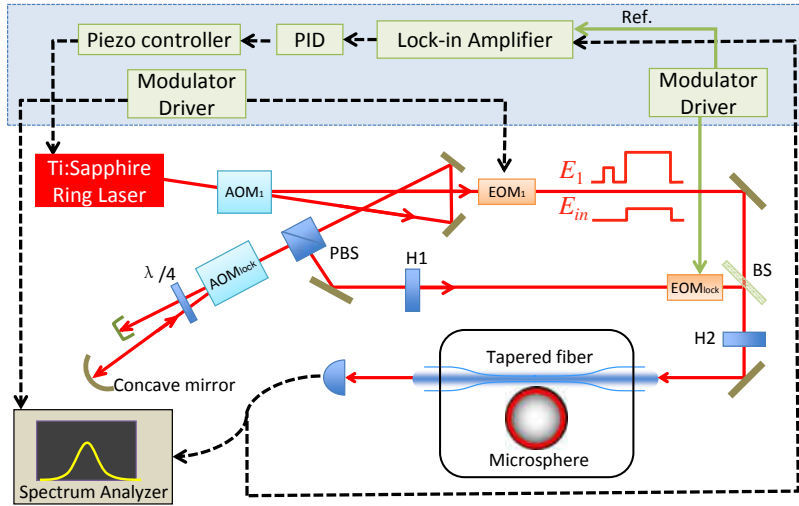
FIGURE 5.4. Experimental apparatus for our later single color light storage experiments[3]. In this later work, we switched to tapered optical fiber for coupling to the microsphere. Also note the introduction of a two-pass AOM for the locking beam, which allowed the lock position to be tuned more easily.

such as the detuning of the writing and reading pulses, can also be adjusted. Profiles of the system can then be constructed by changing any of these parameters iteratively and taking a measurement at each value. At each individual value for the parameter in question, the spectrum analyzer takes a spectrum of the heterodyne response and sends this spectrum a desktop computer. A sample of what these spectra look like is shown in Fig. 5.5. The computer fits a Lorentzian function to this spectrum, and the area under this curve is used to determine the intensity of the response.

5.3. Results

A typical heterodyne detected emission from the resonator is shown in Fig. 5.7, plotted with respect to time. For comparison, a theoretical prediction for the intensity of the intracavity optical field is shown in Fig. 5.6. At t = 0 the on-resonance signal pulse arrives, which is converted to a mechanical excitation by the red-detuned writing pulse. The mechanical excitation, shown as the orange trace in Fig. 5.6, then decays
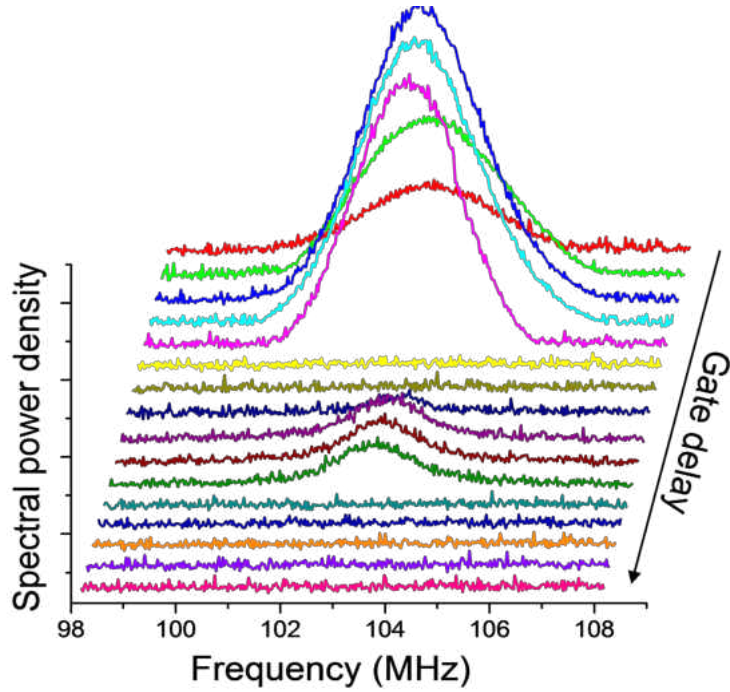
FIGURE 5.5. Heterodyne detected signal field.

exponentially due to mechanical losses. At a later time, the red-detuned reading pulse arrives. The reading pulse converts the mechanical excitation into the retrieved optical signal, which can be seen at t = 8 μs.

The results[3] shown in Fig.5.7 are a significant improvement in time resolution as compared to some of our earlier work [2]. This improvement is primarily due to a modification of the spectrum analyser parameters used for data collection. The previous results were collected with a resolution bandwidth (RBW) of 1 MHz, with a gate length of 3 μs. The gate length was chosen to accommodate the set-up time required by the Agilent E4401B spectrum analyser with the 1 MHz RBW. For our more recent work, a larger resolution bandwidth of 30 MHz was used, allowing for a gate length of 100 ns. The improved time resolution was also facilitated by reducing the beam diameter of light passing through AOM_1.

78
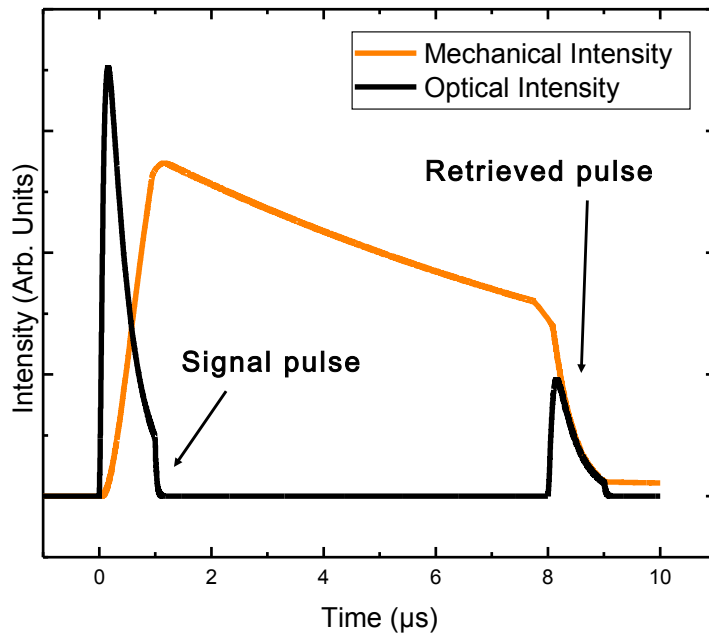
FIGURE 5.6. Theoretical plot of the signal field (black) and intensity of the stored mechanical oscillation (orange).
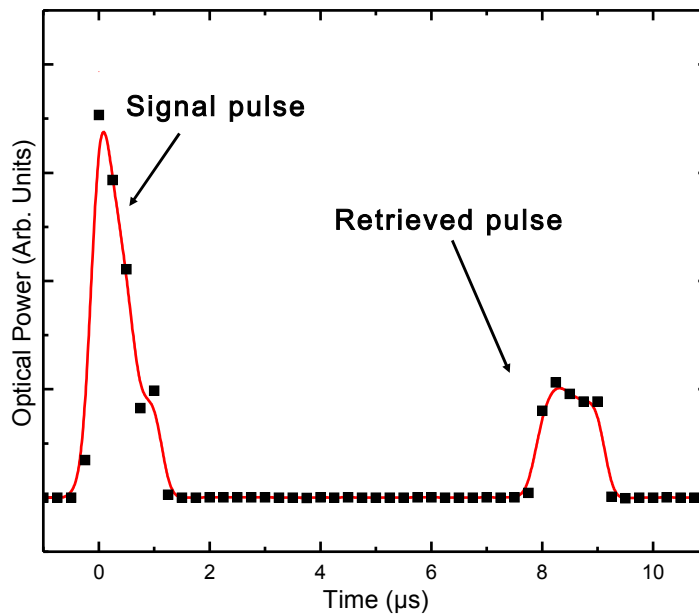
FIGURE 5.7. Power of the heterodyne-detected signal and retrieved pulses emitted from the resonator.
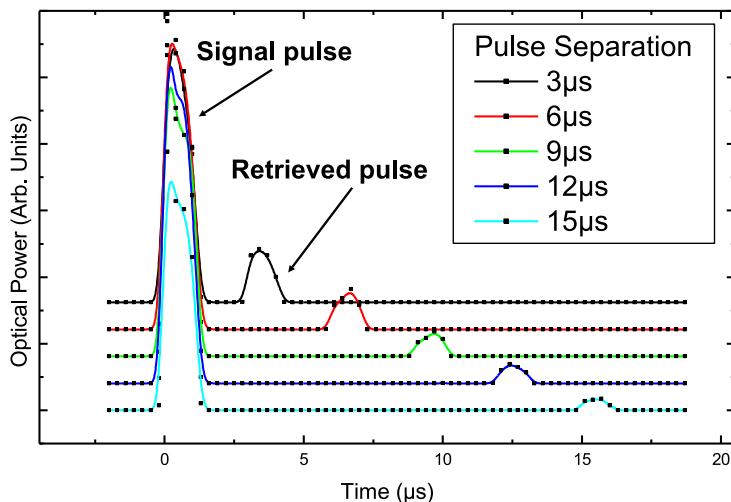
FIGURE 5.8. Power of the heterodyne detected signal and retrieved pulses as a function of time with varying separations between the writing and reading pulses. For these data, all pulses are 1 μs in duration.

Since the storage process relies on a mechanical excitation, the storage lifetime is determined by the mechanical decay lifetime. Figure 5.8 shows the temporal profile of the signal and retrieved pulses with varying separations between the writing and reading pulses. Note that the area of the retrieved pulse, and consequently the energy of the retrieved pulse, decays as the pulse separation is increased. The mechanical decay lifetime can be determined independently from the mechanical linewidth. As shown in Fig. 5.9, the decay of the storage efficiency with respect to the pulse separation shows good agreement with the mechanical decay lifetime determined by the mechanical linewidth, indicating that the storage lifetime is limited only by the mechanical loss of the system. For the experiments described here, the primary source for mechanical loss is clamping loss due to the stem of the microsphere. By keeping the stem diameter as small as possible, we are able to achieve mechanical linewidths on the order of $\kappa/2\pi = 16$ kHz, which corresponds to a decay lifetime of 8.5 μs.

80
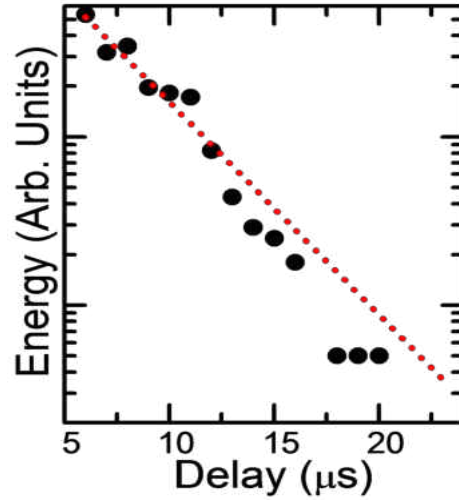
FIGURE 5.9. Dependance of reading intensity on delay between writing and reading pulses.

The light storage process requires the writing and reading pulses to be ω_m away from the signal pulse, satisfying the anti-Stokes resonance condition. Figure 5.10 plots the retrieved pulse energy against the detuning of the writing and reading pulses, which illustrates the necessity of this spectral configuration. Also shown in this figure is the theoretically determined spectral feature, which is in good agreement with the experimental results, both in shape and linewidth. It should also be noted that the theoretically determined feature is independent of the power of the reading pulse.

The optomechanical light storage process also relates to the optomechanical analog to EIT, known as optomechanically induced transparency or OMIT[37]. Light storage has been successfully demonstrated in atomic systems utilizing EIT, where an optical pulse is converted into a stationary superposition of atomic states and then back into an optical signal at a later time[58, 59]. Optomechanical light storage relates similarly to OMIT. In OMIT, a strong pump field at the red sideband renders the system transparent to a weak, on-resonance probe field. By turning the pump
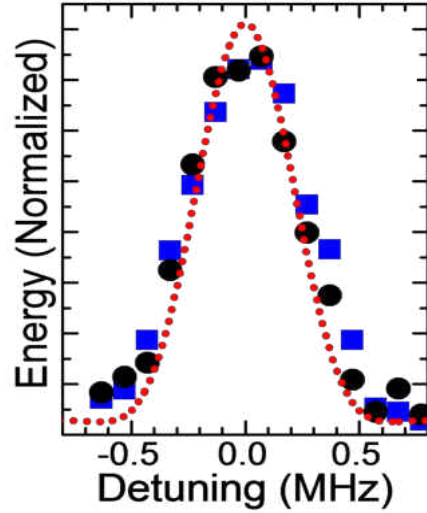
FIGURE 5.10. Retrieved pulse energy as a function of $\omega_p - \omega_L - \omega_m$.

field off and then on again at a later time, the probe field is stored as a mechanical excitation.

To make the comparison to OMIT, we have performed both light storage and OMIT measurements on the same experimental sample. The black trace of Fig. 5.11 shows a typical emission spectrum, detected during the writing phase of the experiment. For these data, the red-detuned control field is held at a fixed frequency relative to the optical mode, while the on-resonance signal field is swept over the optical resonance. In this case, OMIT is observed, with the control field acting as the pump and the signal field acting as the probe. The larger, positive Lorentzian feature is due to the interaction between the signal field and the optical mode. This feature is simply the optical emission from the microsphere, with to the probe pulse entering an optical WGM and being re-emitted. As such, this feature has a linewidth that is determined by the optical linewidth of the microsphere's WGM. The sharp dip at the center of the emission spectrum occurs when the anti-Stokes resonance condition is met between the writing and signal fields. This dip corresponds to OMIT and is the

82
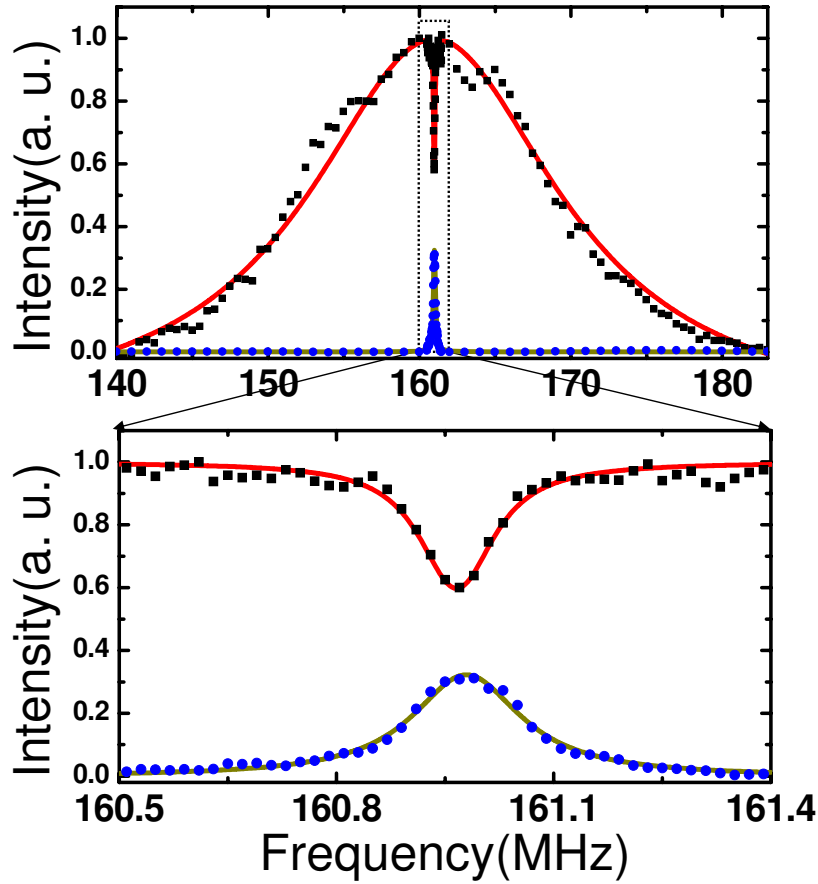
FIGURE 5.11. (a),(b) Optical emission from WGM, detected once the writing pulse has reached steady state (black) and during the reading pulse (red), as a function of detuning, $\Delta = \omega_s - \omega_L$. The solid red line represents the theoretical prediction, and the solid blue line is a Lorentzian fit.

transparency window for the signal pulse. The red trace of Fig. 5.11 is detected during the reading phase, and shows the light storage efficiency as the frequency of the signal field is swept over the optical resonance. This retrieved optical field corresponds to the dip in the OMIT measurement.

Measurements were also performed during the reading phase with varying intensities of the reading pulse, which are shown in Fig. 5.12. As the reading pulse intensity is increased, the mechanical excitation is converted to an optical signal at a faster rate. This leads to a faster decay of the signal.
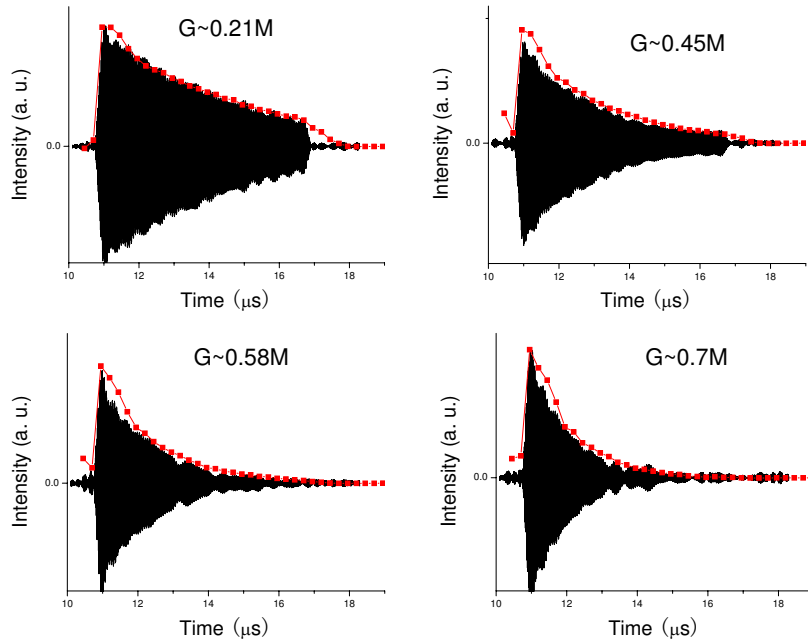
FIGURE 5.12. Heterodyne-detected retrieved optical emission, obtained directly from oscilloscope. The emission is bandpass filtered with the mechanical frequency around 161 MHz.

It is desirable to demonstrate the coherence of the retrieved pulse. In light of this, the measurements performed in Fig. 5.12 were collected by sending the photodetector output directly to an oscilloscope. The RF source used to drive EOM_1 was phase locked to the trigger source for the experiment. The oscilloscope was used to view the retrieved signal with signal averaging. When this was done, a consistent phase was observed for the retrieved signal, suggesting that the retrieved pulse is coherent with the signal pulse.

5.4. Conclusion

We have experimentally demonstrated a system to store an optical signal as a mechanical excitation of a silica microsphere. The storage lifetime is determined by the mechanical damping time, which is on the order of 8.5 μs. These experiments were

carried out at room temperature. At room temperature, the thermal background noise of the mechanical mode prevents this technique from being applied to the quantum regime. There are, however, promising methods that could be used to deal with this thermal noise. For one, recent experimental studies have successfully cooled the mechanical resonator of an optomechanical system to its quantum ground state. Through a combination of these techniques, it may be possible to optomechanically store quantum information.

CHAPTER VI

OPTOMECHANICAL DARK MODE AND OPTICAL MODE CONVERSION

"Fear is the path to the dark side. Fear leads to anger. Anger leads to hate. Hate leads to suffering."

– Yoda, *Star Wars: The Phantom Menace*

6.1. Motivation

There are many applications of optomechanics that gain their usefulness by virtue of their ability to deal with quantum information. This presents an additional challenge, however, given that the mechanical modes of an optomechanical resonator are populated by thermal noise when at room temperature. This thermal noise will swamp any quantum information, thus preventing the system from being used as a quantum device. The most heavily pursued method for overcoming this obstacle has been to cool the mechanical mode to its quantum ground state. This has been met with a reasonable degree of success, but implementation requires a considerable amount of expertise and equipment. While it is possible to perform proof of principle experiments at room temperature, it would be desirable to pursue a method of implementation that would not necessitate the heavy burden of cooling to the ground state.

An alternate approach is to utilize an optomechanical dark mode[68–70]. This approach involves two optical modes that are coupled to the same mechanical mode. An optomechanical dark mode is a superposition of the two optical modes, but is decoupled from the mechanical mode. As such, the dark mode facilitates coupling between the two optical modes, but is protected from the unwanted thermal noise.

86
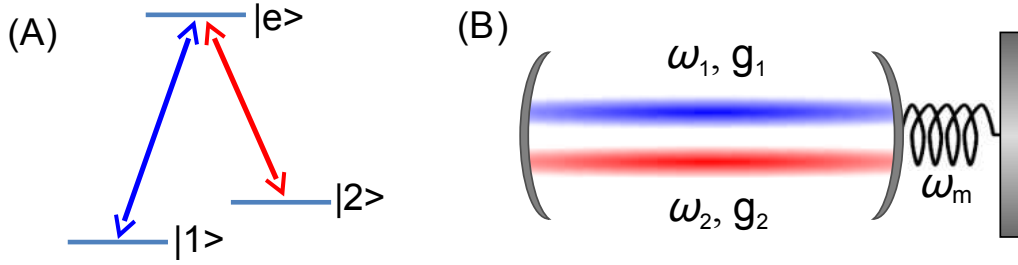
FIGURE 6.1. (a) Energy level diagram of a Λ type system, which can be used to form a dark mode in atomic systems. (b) An optomechanical system with two separate optical modes interacting with a single mechanical oscillator. Each optical mode has its own optomechanical coupling rate, g_1 and g_2.

This would allow several quantum applications of optomechanics to be free from the requirement a quantum ground state.

The optomechanical dark mode is similar to the dark modes that have been demonstrated in atomic systems. In the context of atomic systems, the dark mode phenomenon is thoroughly tested, both with atomic vapors and with solid state systems such as quantum dots and diamond nitrogen vacancy centers. The energy level diagram for the Λ configuration for such a system is shown in Fig. 6.1a. Here, the states $|1\rangle$ and $|2\rangle$ are both coupled to an excited state, $|e\rangle$. A dark mode is formed by stimulating both transitions, such that destructive interference prevents the excited state from interacting. This also induces a conversion between the two lower states, thus allowing those two states to be swapped with each other without being corrupted by the excited state.

In this chapter, we examine the optomechanical variant of the dark mode, using our silica microsphere system in the weak coupling regime[8]. In this optomechanical dark mode, two separate optical whispering gallery modes are coupled to a single mechanical breathing mode. A dark mode is formed by allowing both optomechanical interactions to occur simultaneously, facilitated by the presence of an anti-Stokes shifted optical pulse for each optical mode. The dark mode is immune to the thermal
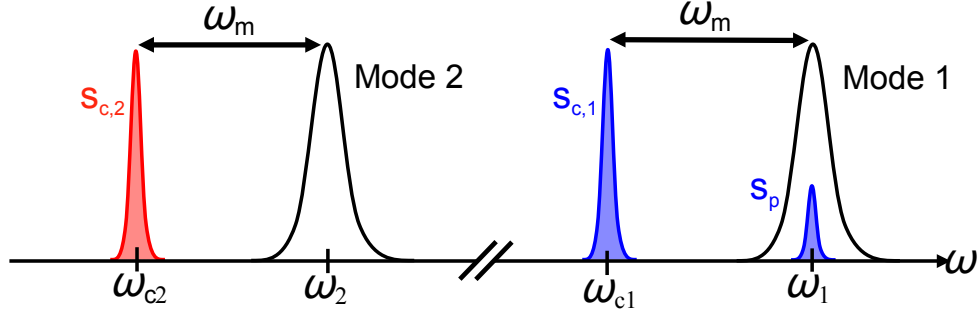
FIGURE 6.2. Spectral position of optical fields relevant to the formation of an optomechanical dark mode. The control lasers, $s_{c,1}$ and $s_{c,2}$ are at the red sideband of each optical mode, and together allow for the formation of the dark mode.

contamination of the mechanical mode, while still allowing an exchange between the two optical modes.

One application that would benefit from the optomechanical dark mode is an optical frequency conversion system[71–75]. The light storage process described in Chapter V can be used to instead convert an optical signal from one optical frequency to another optical frequency by using two different optical modes to interact with the same mechanical mode. This is the system that we use to examine the optomechanical dark mode.

6.2. Dark Mode Theory

To form a dark mode in this system, we use two optical "control" pulses, $s_{c,1}$ and $s_{c,2}$, with each being one mechanical frequency, ω_m, below its respective optical mode, as shown in Fig. 6.2. The frequencies of these two control pulses are $\omega_{L,1}$ and $\omega_{L,2}$, while the frequencies of the optical modes are $\omega_{c,1}$ and $\omega_{c,2}$. Subsequently, we introduce both $\Delta_1 = \omega_{L,1} - \omega_{c,1}$ and $\Delta_2 = \omega_{L,2} - \omega_{c,2}$. We also define $\hat{a}_1$ and $\hat{a}_2$ as relevant linearized intracavity fields for each mode (i.e. $\hat{a}_1$ and $\hat{a}_2$ each correspond

88

to $\delta\hat{a}$). Each mode has its own optomechanical coupling strength, g_1 and g_2. The optomechanical dark mode, $\hat{a}_D$, and bright mode, $\hat{a}_B$, can be defined as follows:

$$\hat{a}_D \equiv (g_2\hat{a}_1 - g_1\hat{a}_2)/\tilde{g}$$
$$\hat{a}_B \equiv (g_1\hat{a}_1 + g_2\hat{a}_2)/\tilde{g},$$

(6.1)

where we have also introduced $\tilde{g} = \sqrt{g_1^2 + g_2^2}$. We can also instead write the intracavity fields in terms of the bright and dark modes:

$$\hat{a}_1 = (g_1\hat{a}_B + g_2\hat{a}_D)/\tilde{g}$$
$$\hat{a}_2 = (g_2\hat{a}_B - g_1\hat{a}_D)/\tilde{g},$$

(6.2)

At this point we revisit our optomechanical Hamiltonian from Eq. 2.25, but now modifying this Hamiltonian to include the second optical mode[68, 70]:

$$\hat{H} = -\hbar\Delta_1\hat{a}_1^\dagger\hat{a}_1 - \hbar\Delta_2\hat{a}_2^\dagger\hat{a}_2 + \hbar\omega_m\hat{b}^\dagger\hat{b} - \hbar g(\hat{a}_1\hat{b}^\dagger + \hat{a}_1^\dagger\hat{b}) - \hbar g(\hat{a}_2\hat{b}^\dagger + \hat{a}_2^\dagger\hat{b})$$

(6.3)

Making the assumption that $\Delta_1 = \Delta_2 = -\omega_m$ and substituting $\hat{a}_1$ and $\hat{a}_2$ from 6.2 into the Hamiltonian in Eq. 6.3 produces a Hamiltonian written in terms of the bright and dark modes:

$$H = \hbar\omega_m(\hat{a}_B^\dagger\hat{a}_B + \hat{a}_D^\dagger\hat{a}_D + \hat{b}^\dagger\hat{b}) - \hbar\tilde{g}(\hat{a}_B^\dagger b + \hat{a}_B b^\dagger)$$

(6.4)

It can be seen from this Hamiltonian that the dark mode is decoupled from the mechanical oscillator, and indeed only the bright mode interacts with the mechanical oscillator. The dark mode is not present in the interaction component of the

Hamiltonian. The bright mode, however, is coupled to the mechanical oscillator with an effective optomechanical coupling rate of $\tilde{g}$.

Looking back at the Hamiltonian in Eq. 6.3, we can follow a similar procedure to that used in Section 2.3 to find the equations of motion for this system. First the Heisenberg Equation is used, followed by the introduction of damping and driving terms. Doing so results in the following equations of motion:

$$\frac{d\hat{a}_1}{dt} = \left(i\Delta_1 - \frac{\kappa_1}{2}\right)\hat{a}_1 + ig_1\hat{b} + \sqrt{\kappa_{ex,1}}\delta\hat{s}_p$$
$$\frac{d\hat{a}_2}{dt} = \left(i\Delta_2 - \frac{\kappa_2}{2}\right)\hat{a}_2 + ig_2\hat{b} \qquad (6.5)$$
$$\frac{d\hat{b}}{dt} = \left(-i\omega_m - \frac{\Gamma_m}{2}\right)\hat{b} + ig_1\hat{a}_1 + ig_2\hat{a}_2$$

Here we have also introduced total cavity decay rates κ_1 and κ_2 for each mode, as well as the cavity decay rates associated with each mode's input coupling, $\kappa_{ex,1}$ and $\kappa_{ex,2}$.

What we really want are equations of motion in terms of the bright and dark modes. We can find these by taking the time derivative of our definitions of a_D and a_B:

$$\frac{d\hat{a}_D}{dt} = (g_2\dot{\hat{a}}_1 - g_1\dot{\hat{a}}_2)/\tilde{g}$$
$$\frac{d\hat{a}_B}{dt} = (g_1\dot{\hat{a}}_1 + g_2\dot{\hat{a}}_2)/\tilde{g} \qquad (6.6)$$

Our system can be simplified at this point by saying that $\Delta_1 = \Delta_2 = -\omega_m$ and that $\kappa_1 = \kappa_2 \equiv \kappa$. We can now substitute the expressions for $\hat{a}_1$ and $\hat{a}_2$ from Eq. 6.2 into Eq. 6.5 to write $d\hat{a}_1/dt$ and $d\hat{a}_2/dt$ in terms of $\hat{a}_D$ and $\hat{a}_B$, then substitute these new expressions for $d\hat{a}_1/dt$ and $d\hat{a}_2/dt$ into Eq. 6.6, and finally perform a little algebra to

obtain the following equations of motion:

$$\frac{d\hat{a}_D}{dt} = \left(-i\omega_m - \frac{\kappa}{2}\right)\hat{a}_D + \frac{g_2}{\tilde{g}}\sqrt{\kappa_{ex,1}}\delta\hat{s}_p$$

$$\frac{d\hat{a}_B}{dt} = \left(-i\omega_m - \frac{\kappa}{2}\right)\hat{a}_B + i\tilde{g}\hat{b} + \frac{g_1}{\tilde{g}}\sqrt{\kappa_{ex,1}}\delta\hat{s}_p \qquad (6.7)$$

$$\frac{d\hat{b}}{dt} = \left(-i\omega_m - \frac{\Gamma_m}{2}\right)\hat{b} + i\tilde{g}\hat{a}_B$$

In the new equations of motion in Eq. 6.7, it is apparent once again that the dark mode does not interact with the mechanical oscillator. This makes it much easier to find a solution. We can follow a line of reasoning similar to the process used to get from Eq. 2.28 to Eq. 2.34, which was done back in Section 2.4. Doing so results in the following solution:

$$A_D^- = \frac{2}{\kappa}\frac{g_2}{\tilde{g}}\sqrt{\kappa_{ex,1}}\bar{s}_p$$

$$A_B^- = \frac{\left(\frac{\Gamma_m}{2} - i\Delta_p\right)}{\frac{\kappa}{2}\left(\frac{\Gamma_m}{2} - i\Delta_p\right) + \tilde{g}^2}\left(\frac{g_1}{\tilde{g}}\right)\sqrt{\kappa_{ex,1}}\bar{s}_p \qquad (6.8)$$

$$B^- = \frac{-ig_1}{\frac{\kappa}{2}\left(\frac{\Gamma_m}{2} - i\Delta_p\right) + \tilde{g}^2}\sqrt{\kappa_{ex,1}}\bar{s}_p$$

Recall that Δ_p is the detuning of the near-resonance probe laser (referred to in this chapter instead as the signal laser), with $\Delta_p = \Omega - \omega_m = \omega_p - \omega_L - \omega_m$.

If the signal laser is at resonance with the optical cavity, then $\Delta_p = 0$. In that case, we have

$$A_D^-(\Delta_p = 0) = \frac{2}{\kappa} \frac{g_2}{\tilde{g}} \sqrt{\kappa_{ex,1}} \bar{s}_p$$

$$A_B^-(\Delta_p = 0) = \frac{2\Gamma_m}{\kappa\Gamma_m + 4\tilde{g}^2} \left(\frac{g_1}{\tilde{g}}\right) \sqrt{\kappa_{ex,1}} \bar{s}_p \tag{6.9}$$

$$B^-(\Delta_p = 0) = \frac{-4ig_1}{\kappa\Gamma_m + 4\tilde{g}^2} \sqrt{\kappa_{ex,1}} \bar{s}_p,$$

which can be simplified by introducing the overall optomechanical cooperativity, $\tilde{C} \equiv 4\tilde{g}^2/\Gamma_m\kappa$:

$$A_D^-(\Delta_p = 0) = \frac{2}{\kappa} \frac{g_2}{\tilde{g}} \sqrt{\kappa_{ex,1}} \bar{s}_p$$

$$A_B^-(\Delta_p = 0) = \frac{1}{1 + \tilde{C}} \left(\frac{2g_1}{\kappa\tilde{g}}\right) \sqrt{\kappa_{ex,1}} \bar{s}_p \tag{6.10}$$

$$B^-(\Delta_p = 0) = \frac{-1}{1 + \tilde{C}} \left(\frac{4ig_1}{\kappa\Gamma_m}\right) \sqrt{\kappa_{ex,1}} \bar{s}_p$$

Evidently, the coupling between the bright mode and the mechanical oscillator displays what could be described as OMIT. The presence of the strong anti-Stokes control lasers suppresses the formation of the bright mode. As shown in Eq. 6.10, the bright mode is suppressed by a factor of $(1 + \tilde{C})$.

In the limit of ultrastrong coupling, where g_1 and g_2 are much greater than κ_1, κ_2, and ω_m, the dark mode becomes spectrally separated from the bright mode. Our system, however, falls into the regime of weak optomechanical coupling. In this regime, the dark mode can no longer be spectrally resolved from the bright mode. Fortunately, this does not preclude the formation of the dark mode, as we have just seen from Eq. 6.10. OMIT gives us a way to suppress the formation of the bright mode.

Another way to express the suppression of the bright mode is to examine the ratio of the dark mode amplitude to bright mode amplitude (at $\Delta_p = 0$):

$$\frac{A_D^-}{A_B^-} = \left(\frac{g_2}{g_1}\right)^2 (1 + \tilde{C})^2 \tag{6.11}$$

As shown here, the suppression of the bright mode occurs when the optomechanical cooperativity is sufficiently high. When compared to the notion of using ultrastrong coupling to spectrally resolve the dark mode from the bright mode, we can see that using OMIT is more practical, given that most optomechanical systems feature optical linewidths that far exceed their mechanical linewidths, whereas most optomechanical systems do not fall into the category of ultrastrong coupling.

If we had not made the assumption that $\kappa_1 = \kappa_2$, this dark-to-bright ratio would instead take the following form:

$$\frac{A_D^-}{A_B^-} = \left(\frac{g_2}{g_1}\right)^2 \left[1 + C_2 + C_1 \left(\frac{\kappa_1}{\kappa_2}\right)\right]^2, \tag{6.12}$$

with C_1 and C_2 being the cooperativities for each individual optical mode, viz. $C_i = 4g_i^2/\Gamma_m \kappa_i$. This shows that a sufficiently large cooperativity is still able to suppress bright mode formation, even if the optical modes differ in optical damping[69, 70].

Now that a method for the formation of the dark mode has been established, we can focus on how the dark mode can be detected. Substituting the result from Eq. 6.10 into the equivalent of the definitions from Eq. 6.2 produces

$$A_1^- = \left(\frac{C_1}{1 + \tilde{C}} + C_2\right) \frac{2}{\kappa} \frac{1}{\tilde{C}} \sqrt{\kappa_{ex,1}} \bar{s}_p$$

$$A_2^- = \left(\frac{1}{1 + \tilde{C}} - 1\right) \frac{2}{\kappa} \frac{\sqrt{C_1 C_2}}{\tilde{C}} \sqrt{\kappa_{ex,1}} \bar{s}_p. \tag{6.13}$$

In these equations, the first term in the parenthesis is due to the bright mode while the second term is due to the dark mode. In A_2^- there is destructive interference between the bright mode contributions. This means that excitation of the second optical mode is a direct consequence of the suppression of the bright mode, and is thus an indication that this suppression has occurred. Additionally, with the excitation of the dark mode and for values of C_2 that are comparable to C_1, increasing C_2 should lead to an increase in both mode 1 and mode 2. This means that examining the behavior of these populations as C_2 is increased will also give an indication of dark mode formation.

6.3. Experimental Details

A description of the individual components of the experimental apparatus is presented in Chapter III. For the dark mode experiments, it is necessary to interact with two different optical modes. The dark mode is formed by two simultaneous anti-Stokes shifted optical pulses, one for each optical mode, which we will refer to as "control" pulses. Another simultaneous optical pulse is at resonance with the first of the two optical modes and serves as our signal pulse. The spectral positioning of these pulses is shown in Fig. 6.1b. The dark mode formed by the two control pulses allows the signal to transfer to the other optical mode.

To generate these pulses, two different lasers were used, each with its own locking circuitry and modulators. The modulators allowed all of these beams to be pulsed, with the experiment beams all arriving simultaneously and having an 8 μs duration. After passing through the modulators for the individual lasers, the light from the two lasers is combined and coupled to the microsphere using the tapered fiber method. Transmitted light is then sent to a diffraction grating, which is used to separate the
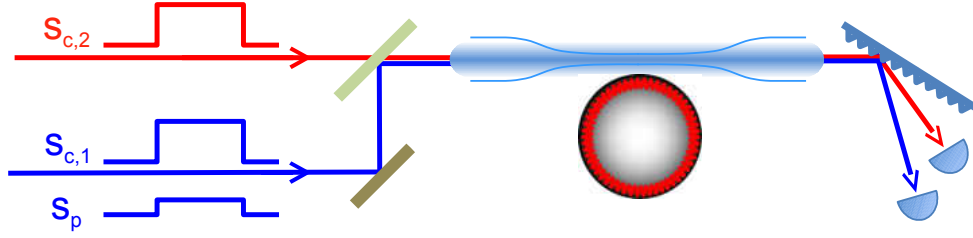
FIGURE 6.3. Simplified diagram of the experimental apparatus for the dark mode experiments. Two separate lasers are used to generate the necessary optical pulses, with each laser locked to one of the relevant optical modes. After exiting the microsphere, the two frequencies of light are separated by a diffraction grating.

light associated with each individual laser. Each separated beam then has its own set of detectors for locking and detection of relevant experimental signals. The spectrum analyzer gate is set to a gate delay of 6 μs from the arrival of the experiment pulses, with a gate duration of 1 μs. When all is said and done, this is essentially the same experimental setup as the OMIT experiment in Chapter IV, but with a duplicate laser and duplicate equipment related to that laser. This is shown diagrammatically in Fig. 6.3.

Two different microsphere samples were used for the data shown in this chapter. For sample A, $(\kappa_1, \kappa_2, \omega_m, \Gamma_m)/2\pi \approx 19, 16, 150, 0.055$ MHz. For sample B, $(\kappa_1, \kappa_2, \omega_m, \Gamma_m)/2\pi \approx 15, 15, 154, 0.06$ MHz. Sample A was used for Figs. 6.4, 6.5, and 6.7. Sample B was used for Fig. 6.6.

6.4. Results

The optomechanical cooperativities for each of the two optical modes can be controlled by adjusting the power of each respective control pulse. Figure 6.4a shows the emission spectrum from optical mode 1 in the absence of a control pulse for optical mode 2, i.e. $C_1 = 1.4$ and $C_2 = 0$. This spectrum is obtained by scanning the signal

field across the optical resonance, thereby adjusting the detuning, $\Delta = \omega_{in} - \omega_{c1}$. The result is a typical OMIT spectrum for optical mode 1, as the second optical mode does not have any effect under these conditions. The value for C_1 is determined by fitting a function to this OMIT spectrum, with the width of the OMIT dip being given by $\omega_m(1 + C_1)$. The same process was performed, but instead exciting optical mode 2 in the absence of control pulse 1, in order to establish subsequent values for C_2. This measurement was performed to obtain all listed values for C_1 and C_2.

By introducing the second control pulse, both optical modes become capable of interacting with the mechanical mode. This allows the formation of the dark mode. The plot in Fig. 6.4b was taken in the same manner as Fig. 6.4a, but now with the introduction of the second control pulse, and hence non-zero values for C_2. The presence of the dark mode leads to a diminishing OMIT dip (and spectral broadening of the dip) as C_2 is increased, due to the increasing excitation of optical mode 1. The dip in the emission spectrum persists, however, even at high values of C_2, due to the conversion from optical mode 1 to optical mode 2 via the dark mode. In other words, at low C_2 this dip is due to OMIT, while at high C_2 the dip is a consequence of dark mode facilitated optical mode conversion.

These spectra are juxtaposed with similar spectra taken at optical mode 2, shown in Fig. 6.4c. The peaks in Fig. 6.4c depict an increasing emission from optical mode 2 as C_2 is increased. As described previously, this emission heralds the formation of the dark mode and the suppression of the light mode. The dip in Fig. 6.4b and the peak in Fig. 6.4 also undergo a noticeable spectral shift as C_2 is increased. This shift arises as a result of the optical spring effect, where the increasing radiation pressure of control pulse 2 causes a shift in ω_m.
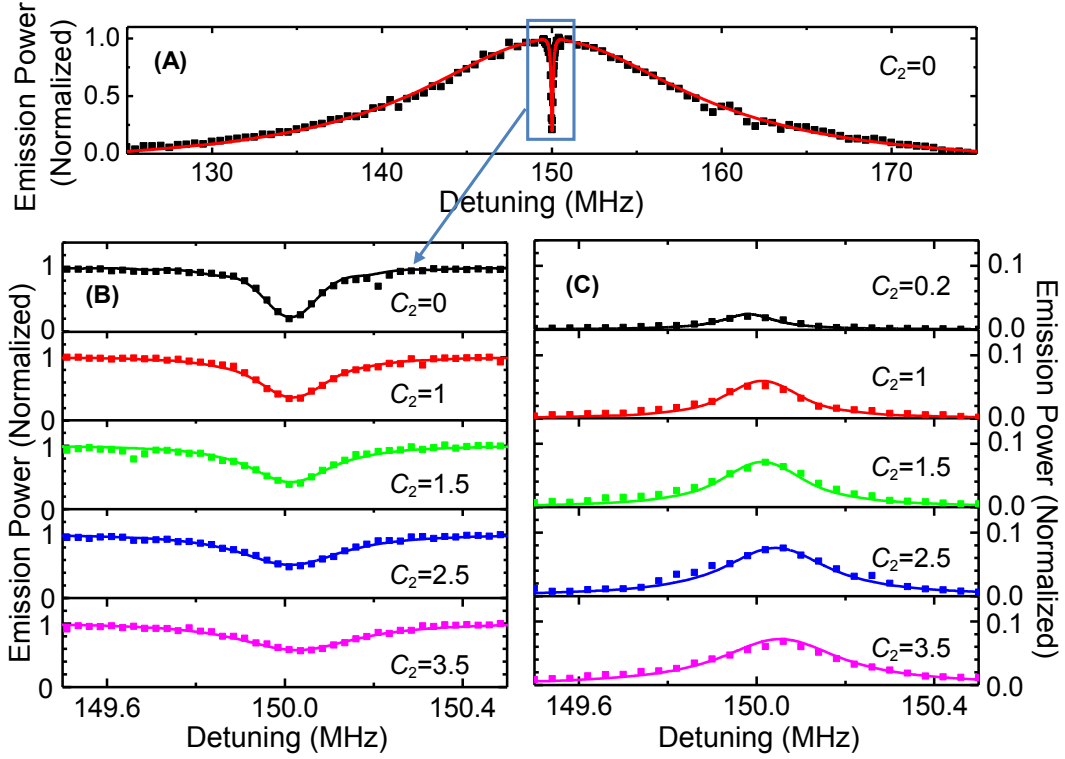
FIGURE 6.4. (a) Optical emission power spectrum for optical mode 1 in the absence of control pulse 2, shown as a function of the detuning, $\Delta = \omega_{in} - \omega_{c1}$. (b and c) Optical emission power spectra for optical mode 1, (b), and optical mode 2, (c), shown as a function of Δ. P_{in}, P_1, and P_2 are the optical powers for E_{in}, E_1, and E_2, respectively. For these three figures, $P_1 = 2.5$ mW, which corresponds to $C_1 = 1.4$. For (a) and (b), $P_{in} = 10 \ \mu W$. For (c), $P_{in} = 20 \ \mu W$. Solid lines depict theoretical predictions. For these and all subsequent plots, the emission power is normalized with respect to the emission power at resonance when $C_1 = C_2 = 0$.
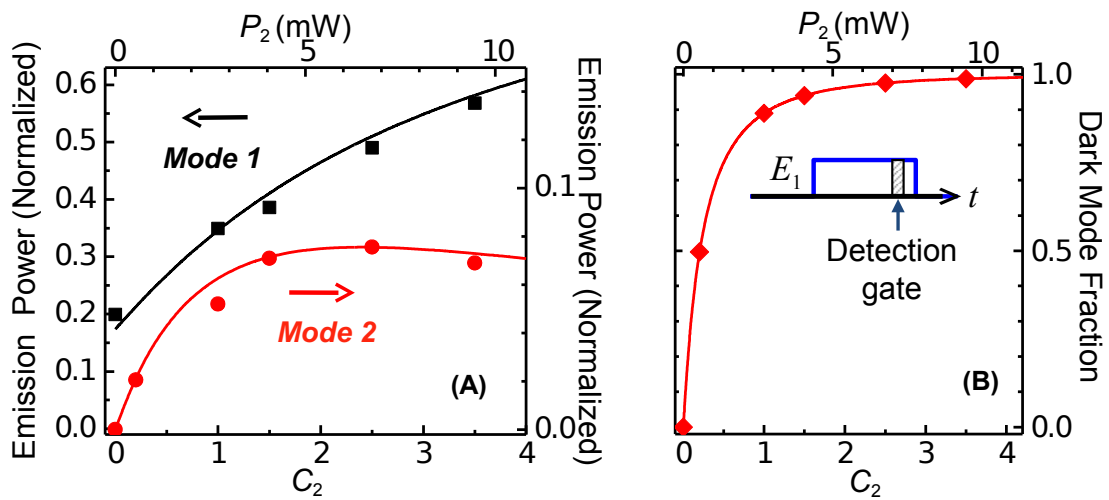
FIGURE 6.5. (a) Emission powers from optical mode 1 (squares) and optical mode 2 (circles), as a function of C_2 and with $\Delta = -\omega_m$. Solid lines indicate theoretical predictions. (b) Calculated dark-mode-to-light-mode fraction as a function of C_2. Diamonds correspond to the individual experimental results shown in (a). (Inset) Timing of the detection gate used for this figure and for Fig. 6.4. The optical pulses arrive simultaneously, with a duration of 8 μs. The detection gate begins 6 μs after the arrival of the optical pulses, and has a gate duration of 1 μs.

The spectra in Figs. 6.4b and c permit the calculation of the optical emission powers for both modes at $\Delta = -\omega_m$, which are shown in Fig. 6.5a. Note that for relatively small C_2, emission from both optical modes increases with increasing C_2. As C_2 becomes sufficiently large and the ratio of dark mode population to light mode population becomes sufficiently high, the emission from optical mode 2 saturates and begins to decrease with further increase in C_2.

The preceding results are also compared to theoretical predictions given by the coupled oscillator model. The parameters necessary for these predictions, κ_1, κ_2, ω_m, Γ_m, C_1, C_2, and $\eta_1 \eta_2 = 0.16$, were all determined experimentally. η_1 and η_2 are the output coupling ratios for each respective optical mode, with $\eta = \kappa_{ex}/\kappa$. Additionally, these experimentally determined values are used to compute the dark mode fraction, i.e. the ratio of dark mode population to bright mode population, which is shown in Fig. 6.5b. The dark mode fraction reaches 99% at the highest value for C_2, with $C_1 = 1.4$ and $C_2 = 3.5$.

It is important to note that while these proof-of-concept experiments exhibit a rather modest photon conversion efficiency, this is not a limitation of optomechanical dark modes in general. The photon conversion efficiency, which is the ratio of output flux from mode 2 over input flux to mode 1, can be written as

$$\chi = 4\eta_1 \eta_2 \frac{C_1 C_2}{(1 + C_1 + C_2)^2}. \tag{6.14}$$

Thus, in our system, the relatively low output couplings and cooperativities lead to our low conversion efficiency. In the limit that $\eta_1 = \eta_2 = 1$ and $C_1 = C_2 \gg 1$, however, the system approaches a unity conversion efficiency.

The detected signal in these experiments is the heterodyne signal from the mixing between the driving field E_2 and the emitted light from optical mode 2. The rise time
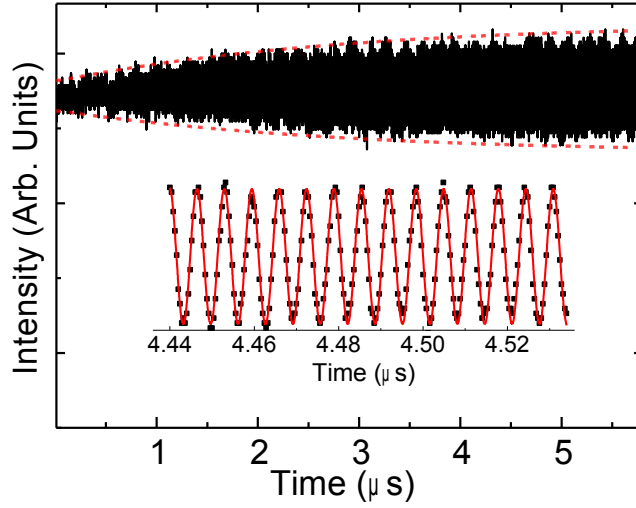
FIGURE 6.6. Heterodyne detected signal resulting from the mixing between the driving field E_2 and the emitted light from optical mode 2, obtained with $P_{in} = 0.1$ mW, $C_1 = 0.25$, and $C_2 = 0.4$. Dashed red lines indicate the theoretically predicted envelope with an adjustable offset. (Inset) Expanded plot of the same signal, showing the frequency of oscillation of the heterodyne signal (squares). For reference, the solid line shows a periodic oscillation with a frequency of $\omega_m/2\pi = 154$ MHz.

for this heterodyne signal is given by $1/[(1 + C_1 + C_2)\Gamma_m]$. This rise time was a critical factor when selecting the detection gate delay of 6 μs. Figure 6.6 shows the heterodyne signal as a function of time, prior to being sent to the spectrum analyzer, with $C_1 = 0.25$ and $C_2 = 0.4$. The rise time of this signal matches the theoretical prediction. Additionally, the frequency of oscillation of this signal was found to match ω_m as expected, which suggests the coherent nature of the optical mode conversion.

It is also desirable to probe the population of the mechanical oscillator, so as to investigate the bright mode population. This was done by the addition of a weak "reading" pulse at the same frequency as E_1, with the reading pulse beginning 1 μs after the termination of the other pulses and lasting 3 μs. The spectrum analyzer gate was then moved to be centered on the reading pulse. These timings are shown in the inset of Fig. 6.7. Additionally, ω_{c1} and ω_{c2} were fixed at their respective red

100
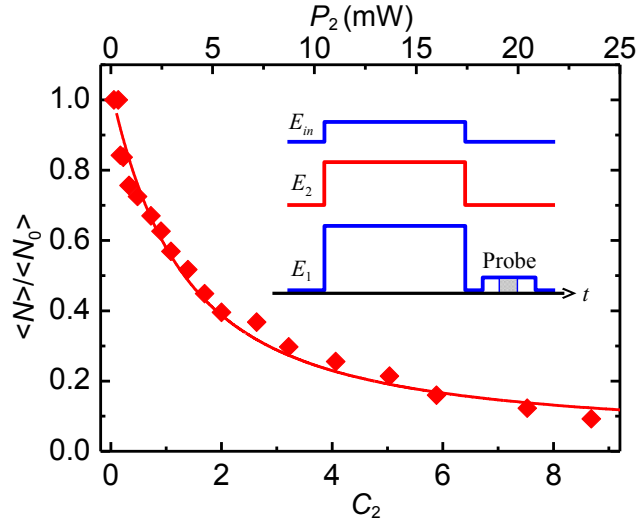
FIGURE 6.7. Population of the mechanical oscillator, shown as a function of C_2. Here, $P_1 = 1.25$ mW, which corresponds to $C_1 = 0.7$, and $P_{in} = 10$ μW. The solid line denotes the theoretical prediction using the coupled oscillator model. (Inset) Timing of pulses used for this figure. The shaded area indicates the spectrum analyzer detection gate.

sidebands. This detection process is essentially the same as the light storage readout process described in Chapter V.

The average phonon number of the mechanical oscillator, $\langle N \rangle$, is then determined by spectrally integrating the power density spectrum obtained from the spectrum analyzer. These measurements were performed with a relatively strong input signal of 10 μW, and with $C_1 = 0.7$. This strong input signal power was chosen in order to keep the detected phonon numbers well above the background thermal phonon number. Under these conditions, the phonon number at $C_2 = 0$, $\langle N_0 \rangle$, is two orders of magnitude greater than the thermal background.

These measurements are shown in Fig. 6.7, plotted as a function of C_2. The results are in good agreement with the theoretical prediction, which is also shown in Fig. 6.7. This agreement supports the concept that the system is driven to a

dark mode at high values for C_2, with the mechanical oscillation being increasingly dampened by anti-Stokes scattering of E_2.

6.5. Conclusion

This chapter presents a successful demonstration of the formation of an optomechanical dark mode. The dark mode is used to pass an optical signal from one optical whispering gallery mode to another, facilitated by coupling to a mechanical mode. By utilizing the dark mode, this optical transfer can occur without the signal being contaminated by the thermal background of the mechanical oscillator.

The experiments presented here use silica microspheres, which feature relatively modest optomechanical cooperativities. Other optomechanical systems, such as optomechanical membranes or nanobeams, feature cooperativites of 10^3 or higher, which is significantly larger than ours. It should be possible to extend the dark mode process to the quantum regime by applying it to one of these ultrahigh quality factor systems.

CHAPTER VII

SUMMARY

7.1. Dissertation Summary

This dissertation examines the transient behavior of an optomechanical system. This includes experimental demonstrations of time-dependent optomechanically induced transparency (OMIT), the use of an optomechanical system as a means for storing an optical signal as a mechanical excitation, and formation of an optomechanical dark mode to facilitate optical mode conversion.

The optomechanical system used for these experiments was a silica microsphere. For most of the experiments, light was coupled to the sphere using a tapered optical fiber. Some of the earlier work involved free-space coupling. Tapered fiber coupling is preferred over free-space coupling, as the free-space method requires the microspheres to be deformed. All of the experiments presented were performed at room temperature.

OMIT is a process where the presence of an anti-Stokes shifted "pump" laser renders an optomechanical system transparent to an on-resonance "probe" laser. In the absence of the pump laser, the on-resonance probe would enter the optical cavity and hence show a dip in its transmitted power, with the width of this transmission dip being determined by the optical quality factor. With the introduction of the pump laser, the pump laser creates a destructive interference which prevents the probe from interacting with the optical cavity. This causes a transparency feature to appear in the probe's transmission, with the width of this OMIT feature being determined by

the mechanical quality factor. Thus the transparency window of OMIT is a narrow feature that appears within the broader absorption feature due to the optical mode.

Previous work involving OMIT focuses on its steady state behavior. The experiments presented in this dissertation examine the time-domain behavior of OMIT. Experimental observation supports a characteristic time scale for OMIT given by $[(1+C)\Gamma_m]^{-1}$, and a damping rate of $C\Gamma_m$. These affect both the width and depth of the OMIT feature.

By gating the pump laser, the OMIT configuration can be used instead as a mechanism for storing an optical signal as a mechanical excitation, as was covered in Chapter V. The presence of the pump laser causes Rabi-like oscillations between the on-resonance optical field and the mechanical oscillator. By applying a $\pi/2$ pulse with the pump laser, an on-resonance optical signal can be converted into a mechanical excitation, and *vice versa*. The storage lifetime was found to be determined by the mechanical damping rate, which was on the order of 8.5 μs for our experimental conditions. At room temperature, the thermal background noise of the mechanical mode prevents this technique from being used for quantum signals.

Finally, introducing a second optical mode allows for the formation of an optomechanical dark mode. By forming a dark mode, it is possible to pass an optical signal from one optical whispering gallery mode to another, using the mechanical mode as a mediator. This dark mode is formed by the presence of two anti-Stokes shifted control lasers, one for each optical mode. The dark mode is a special superposition of the two optical modes that allows for optical mode conversion without interacting with the mechanical oscillator, despite the fact that the mechanical oscillator is the facilitator for this conversion. An experimental demonstration of the formation of an optomechanical dark mode was presented in Chapter VI.

7.2. Future Work

Our demonstration of optomechanical light storage was performed at room temperature. As such, the mechanical mode is already populated by thermal background noise. While this thermal background does not inhibit the use of this system for classical applications, it precludes its use as a system for storing quantum information. This limitation can be overcome, however, by first cooling the mechanical oscillator to its quantum ground state. Several optomechanical systems have been successfully cooled to their mechanical ground state[28, 29]. By combining these techniques, it should be possible to store quantum information optomechanically. This could lead to applications in quantum memory, as well as other methods for quantum optical wavelength conversion that do not necessarily require the formation of a dark mode.

Also, in the classical domain, our implementation of optomechanical light storage is unable to preserve the shape of an optical signal. By constructing a system where a series of optomechanical systems are connected one after another, it should be possible to store an optical signal and still preserve its shape. Such an arrangement would effectively allow for the group delay to be dynamically tuned[22, 54, 76, 77].

Additionally, the microspheres used for our experimental realization of the optomechanical dark mode possess cooperativities slightly greater than 1, and less than 10. This was sufficient to demonstrate the dark mode formation, but would be insufficient for working with quantum signals. There are several other optomechanical systems, such as membranes or nanobeams, that exhibit much higher cooperativities, with some 10^3 or greater[44, 78]. By combining our method for dark mode formation with one of these high cooperativity systems, it should be possible to perform work in the quantum regime while at room temperature.

APPENDIX A

TABLE OF SYMBOLS

Symbol	Meaning
$\hat{H}_L$	Hamiltonian for the optical cavity
$\hat{H}_m$	Hamiltonian for the mechanical oscillator
$\hat{H}_0$	Non-perturbed Hamiltonian
$\hat{H}_{int}$	Interaction Hamiltonian
$\hat{a}$	Photon annihilation operator
$\hat{b}$	Phonon annihilation operator
$\bar{\alpha}$	Optical cavity average coherent amplitude
$\bar{n}_c$	Average classical photon number for the strong control field
$\delta\hat{a}$	Optical cavity fluctuating term
$\hat{s}_{in}$	Total input optical field; $\hat{s}_{in} = \hat{s}_c + \hat{s}_p$
$\hat{s}_c$	Pump/control input optical field
$\hat{s}_p$	Probe/signal input optical field
$\delta\hat{s}_p$	Probe/signal input optical field in frame rotating at ω_L
$\hat{a}_{out}$	Outgoing optical field (Trans. for spheres, refl. for Fabry-Pérot)
$\hat{f}_{in}$	Thermal noise for the optical cavity
$\hat{b}_{in}$	Thermal noise for the mechanical oscillator
$\hat{x}$	Displacement of the mechanical oscillator
x_{zpf}	Zero point fluctuation of the mechanical mode
R	Radius of the microsphere

Symbol	Meaning
ω_c	Optical cavity resonance frequency
ω_m	Mechanical oscillator resonance frequency
ω_L	Frequency of pump/control laser
ω_p	Frequency of probe/signal laser
Δ	Detuning of the pump/control laser; $\Delta = \omega_L - \omega_c$
Ω	Spectral separation between pump and probe; $\Omega = \omega_p - \omega_L$
Δ_p	Detuning of probe/signal laser; $\Delta_p = \Omega - \omega_m = \omega_p - \omega_L - \omega_m$
g_0	Photon-phonon coupling strength; $g_0 = x_{zpf}\omega_c/R$
g	Effective optomechanical coupling strength; $g = g_0\sqrt{\bar{n}_c}$
κ_{ex}	Optical cavity decay rate associated with input coupling
κ_0	Optical cavity decay rate associated with all other effects
κ	Total optical cavity decay rate; $\kappa = \kappa_{ex} + \kappa_0$
η	Optical coupling parameter; $\eta = \kappa_{ex}/\kappa$
Γ_m	Mechanical oscillator decay rate
C	Optomechanical cooperativity; $C = (2g)^2/\Gamma_m\kappa$

DIAGRAMS OF MACHINED PARTS

Following are several schematics for aluminum sample holders used for the experiments presented in this thesis.
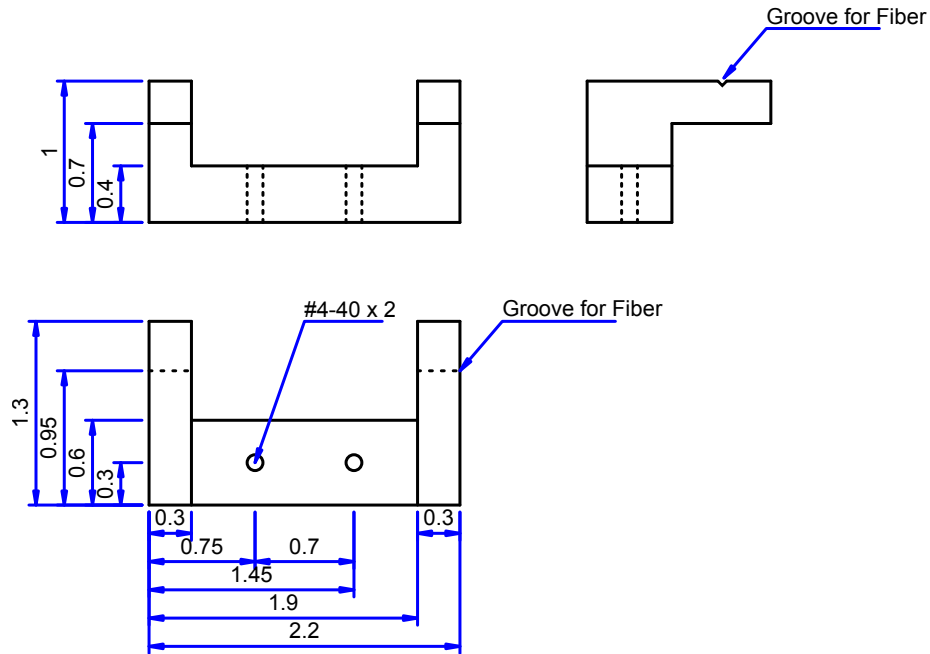
FIGURE B.1. Holder for tapered fiber. The fiber is glued into the groves on each fork. The shape of this holder allows a microscope objective for imaging to be brought in close to the microsphere and tapered section of the fiber. All measurements are in inches.

FIGURE B.2. Microsphere sample holder. The microsphere is suspended vertically and is held in a fiber chuck. The fiber chuck sets into the hole in this sample mount and is secured with a set screw. All measurements are in inches.

REFERENCES CITED

[1] Y.-S. Park and H. Wang. Resolved-sideband and cryogenic cooling of an optomechanical resonator. *Nat. Phys.*, 5:489, 2009.

[2] V. Fiore, Y. Yang, M. C. Kuzyk, R. Barbour, L. Tian, and H. Wang. Storing optical information as a mechanical excitation in a silica optomechanical resonator. *Phys. Rev. Lett.*, 107:133601, 2011.
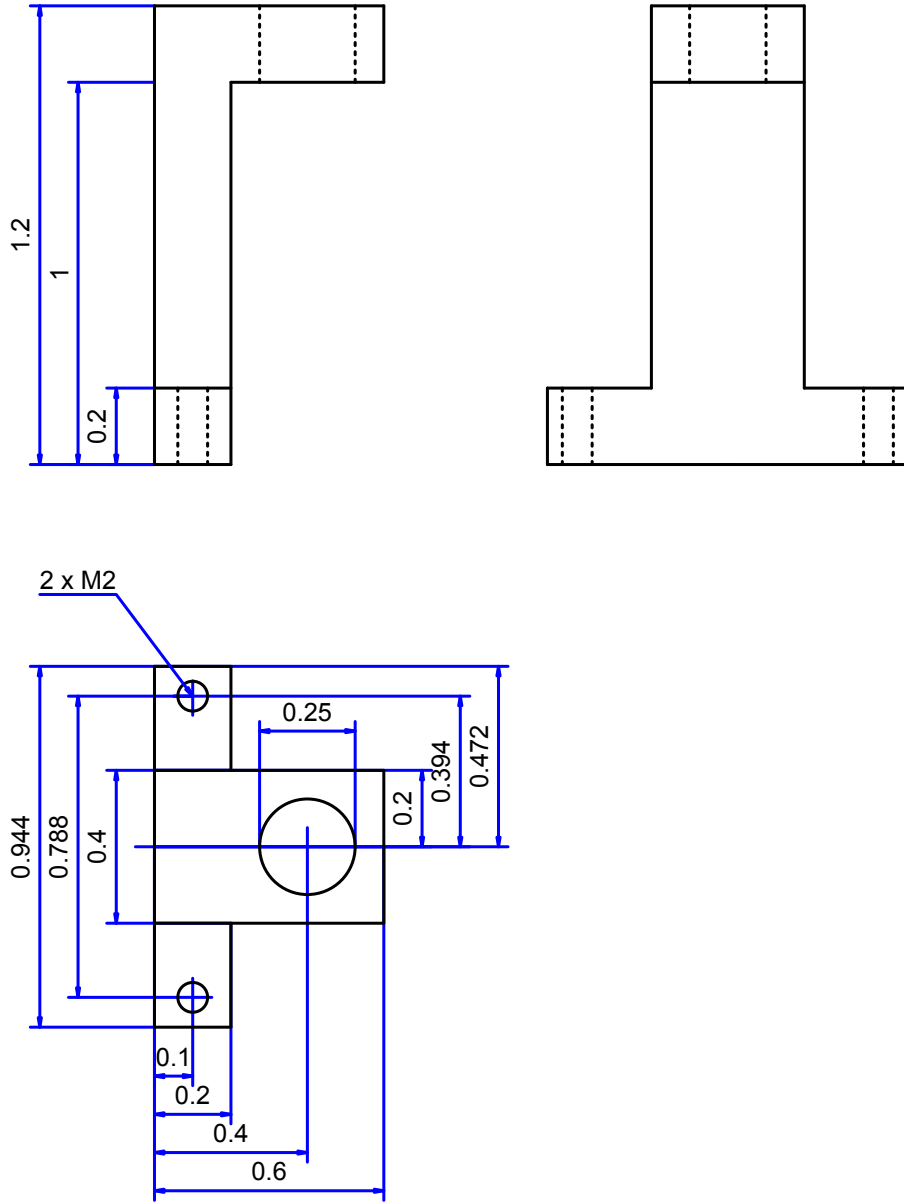
[3] V. Fiore, C. Dong, M. C. Kuzyk, and H. Wang. Optomechanical light storage in a silica microresonator. *Phys. Rev. A*, 87:023812, 2013.

[4] H.J. Kimble. The quantum internet. *Nature*, 453:1023, 2008.

[5] T. D. Ladd, F. Jelezko, R. Laflamme, Y. Nakamura, C. Monroe, and J. L. OBrien. Quantum computers. *Nature*, 464:45, 2010.

[6] R. Hanson and D. D. Awschalom. Coherent manipulation of single spins in semiconductors. *Nature*, 453:1043, 2008.

[7] J. Koch, T. M. Yu, J. Gambetta, A. A. Houck, D. I. Schuster, J. Majer, A. Blais, M. H. Devoret, S. M. Girvin, and R. J. Schoelkopf. Charge-insensitive qubit design derived from the cooper pair box. *Phys. Rev. A*, 76:042319, 2007.

[8] C. Dong, V. Fiore, M.C. Kuzyk, and H Wang. Optomechanical dark mode. *Science*, 338:1609, 2012.

[9] J. Kepler. *De Cometis Libelli Tres*. 1619.

[10] J. C. Maxwell. *On Physical Lines of Force*. 1862.

[11] P. Lebedev. Untersuchungen über die druckkräfte des lichtes. *Annalen der Physik*, 1901.

[12] E. F. Nichols and G. F. Hull. The pressure due to radiation. *The Astrophysical Journal*, 17:315, 1903.

[13] A. Ashkin. Acceleration and trapping of particles by radiation pressure. *Phys. Rev. Lett.*, 24:156, 1970.

[14] T. W. Hänsch and A. L. Shawlow. Cooling of gases by laser radiation. *Optics Communications*, 13:68, 1975.

[15] D.J. Wineland and H. Dehmelt. Proposed 10^{14} $\delta\nu < \nu$ laser fluorescence spectroscopy on Tl^+ monoion oscillator III (sideband cooling). *Bull. Am. Phys. Soc.*, 20:637, 1975.

[16] D. J. Wineland, R. E. Drullinger, and F. L. Walls. Radiation-pressure cooling of bound resonant absorbers. *Phys. Rev. Lett.*, 40:1639, 1978.

[17] M. H. Anderson, J. R. Ensher, M. R. Matthews, C. E. Wieman, and E. A. Cornell. Observation of Bose-Einstein condensation in a dilute atomic vapor. *Science*, 269:198, 1995.

[18] C. A. Regal, M. Greiner, and D. S. Jin. Observation of resonance condensation of fermionic atom pairs. *Phys. Rev. Lett.*, 92:040403, 2004.

[19] T. Reichhardt. Space technology: Setting sail for history. *Nature*, 433:678, 2005.

[20] L. D. Friedman. Interplanetary travel: A puff of wind for the solar sail? *Nature*, 302:104, 1983.

[21] S. Clark. Catching a ride on sunshine. *Nature*, 452:696, 2008.

[22] M. Aspelmeyer, T. J. Kippenberg, and F. Marquardt. Cavity optomechanics. *arXiv*, 1303.0733, 2013.

[23] T. Corbitt, Y. Chen, E. Innerhofer, H. Müller-Ebhardt, D. Ottaway, H. Rehbein, D. Sigg, S. Whitcomb, C. Wipf, and N. Mavalvala. An all-optical trap for a gram-scale mirror. *Phys. Rev. Lett.*, 98:150802, 2007.

[24] M. Vogel, C. Mooser, K. Karrai, and R. J. Warburton. Optically tunable mechanics of microlevers. *Appl. Phys. Lett.*, 83:1337, 2003.

[25] Y.-S. Park. *Radiation pressure cooling of a silica optomechanical resonator*. PhD thesis, University of Oregon, 2009.

[26] C. Höhberger Metzger and K. Karrai. Cavity cooling of a microlever. *Nature*, 432:1002, 2004.

[27] J.-Q. Zhang, S. Zhang, J.-H. Zou, L. Chen, W. Yang, Y. Li, and M. Feng. Fast optical cooling of nanomechanical cantilever with the dynamical zeeman effect. *Opt. Expr.*, 21:29695, 2013.

[28] A. D. OConnell, M. Hofheinz, M. Ansmann, Radoslaw C. Bialczak, M. Lenander, Erik Lucero, M. Neeley, D. Sank, H. Wang, M. Weides, J. Wenner, John M. Martinis, and A. N. Cleland. Quantum ground state and single-phonon control of a mechanical resonator. *Nature*, 464:697, 2010.

[29] J. D. Teufel, T. Donner, Dale Li, J. W. Harlow, M. S. Allman, K. Cicak, A. J. Sirois, J. D. Whittaker, K. W. Lehnert, and R. W. Simmonds. Sideband cooling of micromechanical motion to the quantum ground state. *Nature*, 475:359, 2011.

[30] J. Chan, T. P. Mayer Alegre, A. H. Safavi-Naeini, J. T. Hill, A. K., S. Gröblacher, M. Aspelmeyer, and O. Painter. Laser cooling of a nanomechanical oscillator into its quantum ground state. *Nature*, 478:89, 2011.

[31] E. Verhagen, S. Delglise, S. Weis, A. Schliesser, and T. J. Kippenberg. Quantum-coherent coupling of a mechanical oscillator to an optical cavity mode. *Nature*, 482:63, 2012.

[32] J. Zhang, K. Peng, and S. L. Braunstein. Quantum-state transfer from light to macroscopic oscillators. *Phys. Rev. A*, 68:013808, 2003.

[33] C. Genes, A. Mari, P. Tombesi, and D. Vitali. Robust entanglement of a micromechanical resonator with output optical fields. *Phys. Rev. A*, 78:032316, 2008.

[34] D. E. Chang, C. A. Regal, S. B. Papp, D. J. Wilson, J. Ye, O. Painter, H. J. Kimble, and P. Zoller. Cavity opto-mechanics using an optically levitated nanosphere. *PNAS*, 107:1005, 2010.

[35] F. Vollmer, S. Arnold, and D. Kengb. Single virus detection from the reactive shift of a whispering-gallery mode. *PNAS*, 105:20701, 2009.

[36] LIGO Scientific Collaboration. Observation of a kilogram-scale oscillator near its quantum ground state. *New J. of Phys.*, 11:073032, 2009.

[37] S. Weis, R.i Rivière, S. Deléglise, E. Gavartin, O. Arcizet, A. Schliesser, and T. J. Kippenberg. Optomechanically induced transparency. *Science*, 330:1520, 2010.

[38] C. K. Law. Interaction between a moving mirror and radiation pressure: A hamiltonian formulation. *Phys. Rev. A*, 51:2537, 1995.

[39] I. Wilson-Rae, N. Nooshi, W. Zwerger, and T. J. Kippenberg. Theory of ground state cooling of a mechanical oscillator using dynamical backaction. *Phys. Rev. Lett.*, 99:093901, 2007.

[40] F. Marquardt, J. P. Chen, A. A. Clerk, and S. M. Girvin. Quantum theory of cavity-assisted sideband cooling of mechanical motion. *Phys. Rev. Lett.*, 99:093902, 2007.

[41] G. S. Agarwal and S. Huang. Electromagnetically induced transparency in mechanical effects of light. *Phys. Rev. A*, 81:041803, 2010.

[42] J. J. Sakurai. *Modern Quantum Mechanics*. 1994.

[43] T. J. Kippenberg and K. J. Vahala. Cavity optomechanics: Back-action at the mesoscale. *Science*, 321:1172, 2008.

[44] J. D. Thompson, B. M. Zwickl, A. M. Jayich, F. Marquardt, S. M. Girvin, and J. G. E. Harris. Strong dispersive coupling of a high-finesse cavity to a micromechanical membrane. *Nature*, 452:72, 2008.

[45] T. J. Kippenberg, H. Rokhsari, T. Carmon, A. Scherer, and K. J. Vahala. Analysis of radiation-pressure induced mechanical oscillation of an optical microcavity. *Phys. Rev. Lett.*, 95:033901, 2005.

[46] D. Kleckner and D. Bouwmeester. Sub-kelvin optical cooling of a micromechanical resonator. *Nature*, 444:75, 2006.

[47] V. B. Braginsky, M. L. Gorodetsky, and V. S. Ilchenko. Quality-factor and nonlinear properties of optical whispering-gallery modes. *Phys. Lett. A*, 137:393, 1989.

[48] Y.-S. Park and H. Wang. Radiation pressure driven mechanical oscillation in deformed silica microspheres via free-space evanescent excitation. *Optics Express*, 15:16471, 2007.

[49] M. Cai, O. Painter, and K. J. Vahala. Observation of critical coupling in a fiber taper to silica-microsphere whispering-gallery mode system. *Phys. Rev. Lett.*, 85:85, 2000.

[50] S. M. Spillane, T. J. Kippenberg, O. J. Painter, and K. J. Vahala. Ideality in a fiber-taper-coupled microresonator system for application to cavity quantum electrodynamics. *Phys. Rev. Lett.*, 91:043902, 2003.

[51] S. M. Spillane, T. J. Kippenberg, and K. J. Vahala. Ultralow-threshold raman laser using a spherical dielectric microcavity. *Nature*, 415:621, 2002.

[52] E. D. Black. An introduction to Pound-Drever-Hall laser frequency stabilization. *Am. J. of Phys.*, 69:79, 2001.

[53] G. C. Bjorklund and M. D. Levenson. Frequency modulation (FM) spectroscopy. *Appl. Phys. B*, 32:145, 1983.

[54] A. Schliesser. *Cavity optomechanics and optical frequency comb generation with silica whispering-gallery-mode microresonators.* PhD thesis, Ludwig-Maximilians-Universität München, 2009.

[55] A. H. Safavi-Naeini, T. P. Mayer Alegre, M. Eichenfield J. Chan, Q. Lin M. Winger, J. T. Hill, D. E. Chang, and O. Painter. Electromagnetically induced transparency and slow light with optomechanics. *Nature*, 472:69, 2011.

[56] J. D. Teufel, Dale Li, M. S. Allman, K. Cicak, A. J. Sirois, J. D. Whittaker, and R. W. Simmonds. Circuit cavity electromechanics in the strong-coupling regime. *Nature*, 471:204, 2011.

[57] M. Karuza, C. Biancofiore, M. Bawaj, C. Molinelli, M. Galassi, P. Tombesi R. Natali, G. Di Giuseppe, and D. Vitali. Optomechanically induced transparency in membrane-in-the-middle setup at room temperature. *Phys. Rev. A*, 88:013804, 2013.

[58] M. Fleischhauer, S.F. Yelin, and M. D. Lukin. How to trap photons? storing single-photon quantum states in collective atomic excitations. *Opt. Comm.*, 179:395, 2000.

[59] C. Liu, Z. Dutton, C. H. Behroozi, and L. Vestergaard Hau. Observation of coherent optical information storage in an atomic medium using halted light pulses. *Nature*, 409:490, 2001.

[60] S. E. Harris. Electromagnetically induced transparency. *Phys. Today*, 50:36, 1997.

[61] C. Dong, V. Fiore, M. C. Kuzyk, and H. Wang. Transient optomechanically induced transparency in a silica microsphere. *Phys. Rev. A*, 87:055802, 2013.

[62] R. S. Tucker, P.-C. Ku, and C. J. Chang-Hasnain. Delay-bandwidth product and storage density in slow-light optical buffers. *Electronics Lett.*, 41:41, 2005.

[63] H.-J. Briegel, W. Dür, J. I. Cirac, and P. Zoller. Quantum repeaters: The role of imperfect local operations in quantum communication. *Phys. Rev. Lett.*, 81:5932, 1998.

[64] Q. Xu, P. Dong, and M. Lipson. Breaking the delay-bandwidth limit in a photonic structure. *Nat. Phys.*, 3:406, 2007.

[65] H. Lin, T. Wang, and T. W. Mossberg. Demonstration of 8-Gbit/in.^{2} areal storage density based on swept-carrier frequency-selective optical memory. *Opt. Lett.*, 20:1658, 1995.

[66] D. F. Phillips, A. Fleischhauer, A. Mair, R. L. Walsworth, and M. D. Lukin. Storage of light in atomic vapor. *Phys. Rev. Lett.*, 86:783, 2001.

[67] Z. Zhu, D. J. Gauthier, and R. W. Boyd. Stored light in an optical fiber via stimulated brillouin scattering. *Science*, 318:1748, 2007.

[68] Y.-D. Wang and A. A. Clerk. Using interference for high fidelity quantum state transfer in optomechanics. *Phys. Rev. Lett.*, 108:153603, 2012.

[69] Y.-D. Wang and A. A. Clerk. Using dark modes for high-fidelity optomechanical quantum state transfer. *New J. Phys.*, 14:105010, 2012.

[70] L. Tian. Adiabatic state conversion and pulse transmission in optomechanical systems. *Phys. Rev. Lett.*, 108:153604, 2012.

[71] J. T. Hill, A. H. Safavi-Naeini, J. Chan, and O. Painter. Coherent optical wavelength conversion via cavity optomechanics. *Nat. Comm.*, 3:1196, 2012.

[72] L. Tian and H. Wang. Optical wavelength conversion of quantum states with optomechanics. *Phys. Rev. A*, 82:053806, 2010.

[73] A. H. Safavi-Naeini and O. Painter. Proposal for an optomechanical traveling wave phonon-photon translator. *New J. Phys.*, 13:013017, 2011.

[74] C. A. Regal and K. W. Lehnert. From cavity electromechanics to cavity optomechanics. *J. Phys.: Conf Ser.*, 264:012025, 2011.

[75] Sh. Barzanjeh, M. Abdi, G. J. Milburn, P. Tombesi, and D. Vitali. Reversible optical-to-microwave quantum interface. *Phys. Rev. Lett.*, 109:130503, 2012.

[76] A. Schliesser and T. J. Kippenberg. Cavity optomechanics with whispering-gallery-mode optical micro-resonators. *arXiv*, 1003.5922, 2010.

[77] D. Chang, A. H. Safavi-Naeini, M. Hafezi, and O. Painter. Slowing and stopping light using an optomechanical crystal array. *New J. Phys.*, 13:023003, 2011.

[78] G. Anetsberger, O. Arcizet, Q. P. Unterreithmeier, R. Rivière, A. Schliesser, E. M. Weig, J. P. Kotthaus, and T. J. Kippenberg. Near-field cavity optomechanics with nanomechanical oscillators. *Nat. Phys.*, 5:909, 2009.